

Leibniz Institut für Katalyse e.V. an der Universität Rostock

Theoretical Study of Formic Acid Dehydrogenation and Full Hydrogenation of Acrolein



Dissertation

zur Erlangung des akademischen Grades

Doctor rerum naturalium (Dr. rer. nat.)

der Mathematisch Naturwissenschaftlichen Fakultät

der Universität Rostock

vorgelegt von

Qiquan Luo

geb. Am 14. März, 1984 in Shou City, Anhui Province, China

Rostock, April 2013

urn:nbn:de:gbv:28-diss2013-0115-0

Die vorliegende Arbeit entstand in der Zeit von Oktober 2009 bis April 2013 unter der Leitung von Herrn PD Dr. Haijun Jiao am Leibniz Institut für Katalyse e.V. an der Universität Rostock. Vollständiger Abdruck der von der mathematisch-Naturwissenschaftlichen Fakultät der Universität Rostock zur Erlangung des akademischen Grads eines Doktors der Naturwissenschaft genehmigten Dissertation.

Gutachter der Disseration:

1) PD Dr. Haijun Jiao

Leibniz-Institut für Katalyse e. V. an der Universität Rostock
Albert-Einstein Str. 29a, 18059 Rostock, Deutschland

2) Prof. Dr. Ralf Ludwig

Institut für Chemie, Universität Rostock
Dr.-Lorenz-Weg 1, 18059 Rostock, Deutschland

Tag der Einreichung: 23. April 2013

Tag der Promotion: 23. Juli 2013

Acknowledgement

Foremost, I own my sincere thanks to my supervisor PD. Dr. Habil. Haijun Jiao. He gave me an opportunity to study with him and, I am very lucky to be his first PhD student in Rostock. He has created a very nice academic atmosphere, and offered me much advice. Without his patient supervising and encouragement, I could not have finished this dissertation.

I would like to thank Prof. Matthias Beller. I have experienced a fantastic period in his group and it is an honor to be a member of group Beller. I would like also to thank Prof. Dr. Ralf Ludwig from the Institute of Chemistry and Prof. Dr. Ronald Redmer from the Institute of Physics of University of Rostock for allocating computer facilities.

I would also like to thank the past and present colleagues in this institute for their kind help and the precious friendship. They are Dr. Shaolin Zhou, Dr. Xiao-Feng Wu, Ailing Qiao, Dr. Yuehui Li, Dr. Min Zhang, Dr. Shu-Ping Luo, Dr. Yang Li, Dr. Liang-Qiu Lu, Dr. Si-Ping Wei, Dr. Yingyong Wang, Dr. Steffen Fleischer, Dr. Shoubhik Das, Dr. Andreas Dumrath, Lipeng Wu, Xianjie Fang, Dr. Qiang Liu and Dr. Lin He.

I have always benefited from the discussions with Prof. Dr. Qi-liang Lu, Dr. Gang Feng, Dr. Caihong Guo, Tao Wang, Dr. Shengguang Wang, Dr. Run Long, Xiaohu Yu and Dr. Guido Walther.

I would also like to express my thanks to Dr. Andreas Appelhagen and Matthias Linke for their technical support during this work.

I have a lot of close friends in Rostock, they are Chen Jin, Tao Xie, Renhao Xie, Dr. Chaonan Zheng, Qingyuan Wei, and so on.

I would also like to thank my elder sister and her husband, for so many years taking care of our parents.

Finally, I would like to thank my parents and my wife, I love you!

Summary

This dissertation focused mainly on theoretical study of formic acid (HCOOH) decomposition on the Ni(111), Pd(111), Ni(211), Pd(211), Pt(211) and β -Mo₂C(101) surfaces, since formic acid has been considered as one of potential materials in hydrogen storage and generation. The formate route ($\text{HCOOH} \rightarrow \text{HCOO} + \text{H}$) plays the dominating role in formic acid decomposition; and the rate-determining step is the dissociation of formate into surface CO₂ and H ($\text{HCOO} \rightarrow \text{CO}_2 + \text{H}$). In addition, the Ni(111) surface was also employed to investigate the mechanism of full acrolein hydrogenation. It is found the C=C bonds can be more easily hydrogenated both kinetically and thermodynamically than C=O double bonds. Acrolein hydrogenation follows the Langmuir-Hinshelwood mechanism, while the hydrogenation of allyl alcohol and propanal obeys the Eley-Rideal mechanism.

Zusammenfassung

Diese Dissertation befasst sich hauptsächlich mit theoretischen Studien über die Zersetzung von Ameisensäure (HCOOH) auf Ni(111)-, Pd(111)-, Ni(211)-, Pt(211)- und β -Mo₂C(101)-Oberflächen, da Ameisensäure als potentiell Material für die Lagerung und Erzeugung von Wasserstoff in Frage kommt. Die Zersetzung über das Formiat ($\text{HCOOH} \rightarrow \text{HCOO} + \text{H}$) hat den entscheidenden Anteil am Ameisensäureabbau, und der geschwindigkeitsbestimmende Schritt ist die Dissoziation des Formiats an der Oberfläche zu CO₂ und H ($\text{HCOO} \rightarrow \text{CO}_2 + \text{H}$). Weiterhin wurden die Ni(111)-Oberflächen zur Untersuchung des Mechanismus der vollständigen Acrolein-Hydrierung genutzt. Es hat sich gezeigt, dass C=C-Doppelbindungen im Vergleich zu C=O-Doppelbindungen sowohl kinetisch als auch thermodynamisch leichter hydriert werden können. Die Acrolein-Hydrierung verläuft nach dem Langmuir-Hinshelwood-Mechanismus, wobei die Hydrierung von Allylalkohol und Propanal dem Eley-Rideal-Mechanismus folgt.

Table of Contents

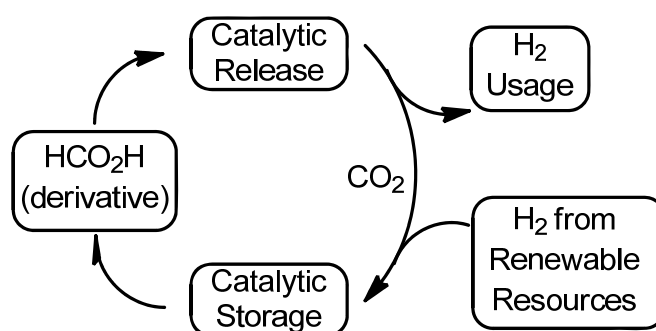
1 Computational Hydrogen Generation from Formic Acid.....	1
1.1 Introduction.....	1
1.2 Metals.....	4
1.2.1 Platinum.....	4
1.2.2 Palladium.....	10
1.2.3 Nickel.....	13
1.2.4 Copper.....	14
1.2.5 Gold.....	15
1.3 Metal oxides.....	16
1.3.1 Titanium oxide.....	16
1.3.2 Magnesium oxide.....	18
1.3.3 Zinc oxide.....	18
1.3.4 Nickel oxide.....	19
1.4 Conclusion and outline.....	20
1.5 References.....	21
2 Formic Acid Dehydrogenation on Ni(111) and Pd(111) and Comparison with Pt(111).....	26
2.1 Introduction.....	26
2.2 Computational details.....	27
2.3 Results and Discussion.....	29
2.3.1 Formic acid (HCO ₂ H/DCO ₂ H) adsorption.....	29
2.3.2 Formate (HCO ₂ /DCO ₂) adsorption.....	30
2.3.3 HCO ₂ and H co-adsorption.....	31
2.3.4 CO ₂ and H co-adsorption.....	32
2.3.5 HCO ₂ H dehydrogenation.....	33
2.3.6 Comparison with other surfaces.....	35
2.4 Conclusions.....	37
2.5 References.....	38
3 Formic Acid Dehydrogenation on Ni(211), Pd(211) and Pt(211).....	42
3.1 Introduction.....	42
3.2 Computational models and details.....	43
3.3 Results and discussion.....	45
3.3.1 HCO ₂ H adsorption.....	45
3.3.2 HCO ₂ H dissociation.....	45
3.3.3 HCO ₂ adsorption and dissociation.....	46
3.3.4 H adsorption on M(211).....	48
3.3.5 CO ₂ adsorption and desorption on M(211).....	49
3.3.6 Potential energy surface.....	51

3.4 Conclusions	53
3.5 References	53
4 Formic Acid Dehydrogenation on Molybdenum Carbide	57
4.1 Introduction	57
4.2 Computational details	58
4.2.1 Model	58
4.2.2 Method	59
4.3 Results and Discussion	59
4.3.1 Adsorption of the surface intermediates	59
4.3.2 Dissociation path	63
4.3.3 Potential Energy Surface	66
4.3.4 Comparison with Pd(111), Pt(111) and Ir(100).....	68
4.4 Conclusions	69
4.5 References	70
5 Full Acrolein Hydrogenation on Ni(111).....	74
5.1 Introduction	74
5.2 Computational details	75
5.3 Results and Discussion	76
5.3.1 Hydrogenation intermediates	76
5.3.2 Hydrogenation transition states	80
5.3.3 Potential energy surface of selective hydrogenation	82
5.3.4 Comparison with other surfaces	84
5.4 Conclusions	85
5.5 References	86
Appendix	
Eidesstattliche Erklärung	
Curriculum Vitae	
Publications	

1 Computational Hydrogen Generation from Formic Acid

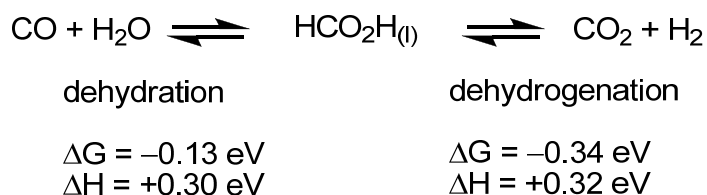
1.1 Introduction

Formic acid (HCO₂H, FA) dehydrogenation into hydrogen (H₂) and carbon dioxide (CO₂) is considered as one of the potential reactions to satisfy the increasing energy demand, especially in fuel cells as well as green and clean technologies. FA, which has 4.4% wt of hydrogen, is non-toxic, easy to be stored and transported as well as handled; all those make it as a desirable hydrogen storage material. [Scheme 1.1](#) shows the catalytic cycle of the formation and decomposition of FA in hydrogen storage and generation.¹



Scheme 1.1 Catalytic cycle for FA hydrogen storage and release

FA also can dehydrate into water (H₂O) and carbon monoxide (CO), and CO is a poison for fuel cell catalysts. Under standard reaction conditions, both dehydrogenation and dehydration starting from liquid FA, are endothermic and exergonic. Since the differences in both Gibbs free energy and enthalpy are rather small ([Scheme 1.2](#)), it is possible to dehydrogenate FA selectively to H₂ by changing reaction conditions or/and using suitable catalysts for practical applications.¹



Scheme 1.2 FA decomposition pathways

FA decomposition was first investigated in 1912 by Mailhe and Sabatier by using metals and metal oxides as catalysts.² Since then this topic has attracted great interests and several reviews about this chemistry have been published.³⁻⁶ Recent progress has been made in both heterogeneous and homogeneous catalysis. Tedsree *et al.*,⁷ reported that Ag nanoparticles coated with a thin layer of Pd atoms can significantly enhance H₂ production from FA

at ambient temperature; and atom probe tomography confirmed that these nanoparticles have a core-shell configuration with the shell containing 1-10 layers of Pd atoms; and the Pd shell contains terrace sites and is electronically promoted by the Ag core, leading to significantly enhanced catalytic properties. Tian *et al.*,⁸ reported the synthesis of core-shell-cluster trimetallic nanostructures (Au@Pd@Pt, gold core covered by a palladium shell, onto platinum clusters are deposited) and the high activity for FA electrooxidation. Bi *et al.*,⁹ reported mild and selective decomposition of FA/amine mixtures by using ultradispersed subnanometric Au as catalysts on acid-tolerant ZrO₂ without CO formation under ambient conditions in high efficiency. Flaherty *et al.*,¹⁰ reported that FA decomposition on carbon modified Mo(110) is up to 15 times more selective than on Mo(110). Solymosi *et al.*, reported CO free H₂ production from FA decomposition using Mo₂C/carbon(Norit) catalysts¹¹ and supported Au catalysts.¹² Kang *et al.*,¹³ reported the synthesis of Pt₃Pb nanocrystals and core-shell Pt₃Pb-Pt nanocrystals in solution phase and found that such nanocatalysts are more efficient for FA oxidation electro-catalysis than only Pt catalysts. Cuesta *et al.*,¹⁴ reported a detailed spectrokinetic study of FA electrocatalytic oxidation on Au and Pt electrodes and found that the adsorbed formate (HCOO) is the intermediate for both dehydrogenation and dehydration on metals. The reaction mechanisms of methanol synthesis from CO₂ and CO hydrogenation over industrial Cu/ZnO/Al₂O₃ catalysts have been investigated by Behrens *et al.*,¹⁵ both experimentally and computationally; and they found that the active site consists of Cu steps decorated with Zn atoms, all stabilized by a series of well-defined bulk defects and surface species that need to be present jointly for the system to work. Zhang *et al.*,¹⁶ synthesized a set of nanoparticles of silver and palladium alloy (Ag₂₅Pd₇₅, Ag₄₂Pd₅₈, Ag₆₀Pd₄₀, Ag₈₀Pd₂₀) at the size of about 2.2 nm and found that Ag₄₂Pd₅₈ has the highest activity with an initial turnover frequency of 382/h and an apparent activation energy of 0.23 eV, and it is the best catalytic performance ever reported among all heterogeneous catalysts tested for FA dehydrogenation in aqueous solution. Wang *et al.*,¹⁷ reported a stable and low-cost non-noble Co_{0.30}Au_{0.35}Pd_{0.35} nano-catalyst (~ 20nm) supported on carbon to generate CO-free H₂ from FA aqueous solution at 298 K.

Homogeneous catalysts have also been used to generate hydrogen from FA.¹⁸ In particular, Beller *et al.*,¹⁹ reported H₂ generation from FA/amine mixtures at high rates at room temperature with the commercially available complex [RuCl₂(PPh₃)₃] as the catalyst for direct usage in fuel cell. Similar results were also reported by Laurenczy *et al.*,²⁰ and Fukuzumi.²¹ Beller *et al.*,²² reported H₂ generation from FA by using iron complexes under basic conditions and light irradiation, and they further improved their protocol by using Fe(BF₄)₂·6H₂O/PP₃ complexes under milder conditions in a green solvent without using amine and light.²³

Due to the practical importance for H₂ generation from FA in fuel cell and green technology, many computational studies have been carried out to understand FA decomposition mechanisms on one hand, and to rationalize and design more effective catalysts in heteroge-

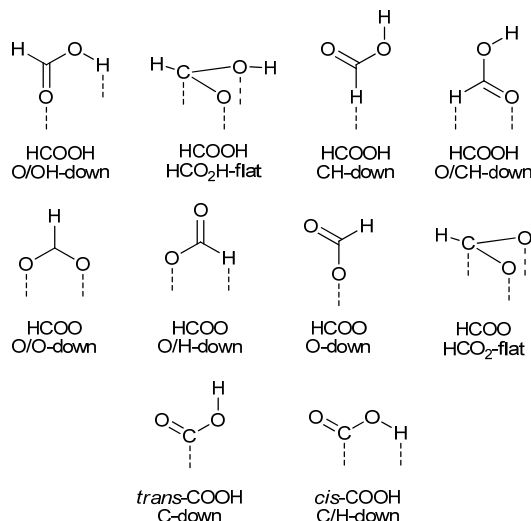
neous and homogeneous systems on the other hand. Nowadays computational chemistry and catalysis have gained more and more attentions due to the rapid development in theoretical methods and information technology. Computational chemistry and catalysis become a powerful tool to provide fundamental insights into mechanisms as well as kinetic and thermodynamic properties of elementary steps of catalytic reactions, especially of the steps, which are hardly or even not accessible with experimental methods. Some examples can be found in reviews^{24–28} or books.^{29,30} Herein, we focus only on the recent computational studies on FA decomposition (or CO₂ hydrogenation to FA) on metals and metal oxides, and the results about the stationary adsorptions of related individual surface intermediates are not discussed. Computational studies on homogeneous FA decomposition (or CO₂ hydrogenation to FA) using defined molecular catalysts are also not discussed in this paper, but the reviews^{26,31,32} and recent papers^{33–36} are given for interests.

Scheme 1.3 shows the most discussed surface adsorption configurations of FA, formate (HCOO) and carboxyl (COOH). For *trans*-FA, there are four possible adsorption configurations, the first one (**O/OH-down**) has its oxygen atom of the C=O group at the top of surface atom and the hydrogen atom of the O-H group directing to the surface (either one or two surface atoms); and the second one (**HCO₂H-flat**) has a flat adsorption configuration with the carbon atom and the two oxygen atoms interacting with the surface atoms, and the third one (**CH-down**) has only the C-H bond directing to the surface, and the last one has the oxygen atom of the C=O group interacting with the surface atoms and the hydrogen atom of the C-H group also pointing to the surface (**O/CH-down**) as well.

For formate (HCOO), there are four possible adsorption configurations, and the first one (**O/O-down**) is the well-known bidentate adsorption configuration with its two oxygen atoms interacting with two surface atoms (bridging) or one surface atom (chelating), and the second one (**O/H-down**) has a bidentate adsorption configuration with one of the O atoms and the H atom of the O-H group interacting with the surface atoms; and the third one (**O-down**) has a monodentate adsorption configuration with one O atom interacting with the surface atoms (and the hydrogen atom of the C-H group might or might not interact with surface atoms), and it is also possible for formate to have a flat adsorption configuration with its carbon and oxygen atoms interacting with the surface atoms (**HCO₂-flat**). For carboxyl (COOH), there are two possible adsorption configurations; the first one (**C-down**) has a monodentate carbon atom and the hydrogen atom of the O-H group pointing away from the surface, and the second one also has a monodentate carbon atom adsorption, but the hydrogen atom of the C-H group pointing to the surface (**C/H-down**). In our discussion we referee all these possible adsorption configurations, and those not shown in **Scheme 1.3** are described accordingly.

There are three proposed potential routes for FA oxidation (**Scheme 1.4**).³⁷ This first one is the formate route; where FA dissociates into surface formate (HCO₂H → H + HCOO), which forms CO₂ (HCOO → H + CO₂); and the second one is the direct route with FA decomposition

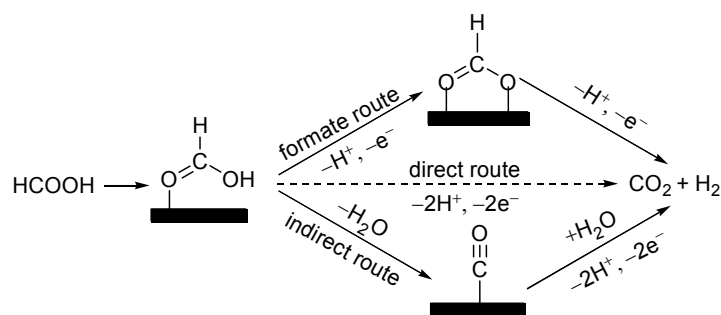
into $\text{CO}_2 + 2\text{H}$ (either $\text{HCO}_2\text{H} \rightarrow 2\text{H} + \text{CO}_2$ or $\text{HCO}_2\text{H} \rightarrow \text{H} + \text{COOH}$; $\text{COOH} \rightarrow \text{CO}_2 + \text{H}$); and the third one is the indirect route with FA dehydration into CO ($\text{HCO}_2\text{H} \rightarrow \text{CO} + \text{H}_2\text{O}$), which is further oxidized to CO_2 from the water-gas shift reaction ($\text{CO} + \text{H}_2\text{O} \rightarrow \text{H}_2 + \text{CO}_2$).



Scheme 1.3 Possible adsorption configurations of FA, HCOO and COOH on surfaces

1.2 Metals

FA is one of the representative molecules used to study the catalytic properties of metals, and many studies have been done both theoretically and experimentally. In addition to the experimental results, theoretical results might give an understanding of FA adsorption and decomposition on metal surfaces at the atomic level. The agreement between theory and experiment can validate the used models and methods.



Scheme 1.4 Proposed FA oxidation routes [37]

1.2.1 Platinum

Platinum is one of the most used metals in FA decomposition to produce H_2 . Not only the gas phase adsorption and dissociation but also electro-catalytic oxidations under the consideration of water molecules or solvation have been investigated.

Bakó and Pálincás³⁸ investigated FA adsorption on Pt(111) in gas phase using periodic

density functional theory (DFT) method (GGA-PBE) in a $3 \times 2 \times 3$ supercell and a 3-layer slab (one relaxed top layer and two fixed bottom layers) with 15 Å vacuum gap. For *trans*-FA they found the **O/OH-down** adsorption configuration be to most stable (Scheme 1.3), and the calculated adsorption energy is -0.42 eV. Due to their interaction with the surface Pt atoms, both the O-H and C=O bonds are elongated compared to the gas phase values and their stretching frequencies are red shifted. The O-H bond becomes therefore weak. In addition, the individual adsorptions of FA, HCOO and COOH on Pt(111) have been reported by Saliccioli *et al.*,³⁹ and the most stable FA adsorption conformation is the same as found by Bakó and Pálinkás,³⁸ but the computed adsorption is larger (-0.56 eV). The HCOO intermediate has a bridging bidentate adsorption configuration (**O/O-down**) and the computed adsorption energy is -2.45 eV; while the COOH intermediate has a **C/H-down** adsorption configuration and the computed adsorption energy is -2.69 eV.

Hartnig *et al.*,⁴⁰ reported FA adsorption on the Pt(111) surface from gas phase and also in the presence of one and two H₂O molecules by using periodic DFT method (GGA-PBE) and a 4-layer (two relaxed top layers and two fixed bottom layers) slab in a 4×4 unit cell with 16.1 Å vacuum gap. On the neutral surface in gas phase, they found the same most stable adsorption configuration (**O/OH-down**) as reported by Bakó and Pálinkás,³⁸ and the calculated adsorption energy is -0.37 eV. On the neutral surface with one H₂O molecule, the most stable adsorption configuration has FA with its two oxygen atoms bonding to the surface and the H atom of the O-H bond interacting with the oxygen atom of the neighbouring H₂O molecule; and the calculated adsorption energy is -0.70 eV. Adding one more H₂O molecule to the adsorbed FA/H₂O complex on the neutral surface leads to hydrogen bonding interaction between two H₂O molecules; and no FA dissociation is observed.

On the charged surface with $q=4e$ in gas phase by removing 4 electrons from the slab with 16 surface atoms, the most stable adsorption configuration has both oxygen atoms bonding to the surface and the hydrogen atom of the O-H group pointing away from the surface; and the calculated adsorption energy is -2.28 eV. By adding one H₂O molecule to the adsorbed FA, the intermediate structure has a bidentate adsorption configuration with two oxygen atoms bonding to the surface and the O-H bond forming a strong hydrogen bonding with the H₂O molecule; and the calculated adsorption energy is -3.83 eV. However, the most stable adsorption configuration has dissociated surface H atom, CO₂ and hydronium ion (OH₃⁺), and the calculated adsorption energy is -4.54 eV, indicating the driving force for FA decomposition. Adding one more H₂O molecule to the dissociated surface leads to the formation of a complex with one H⁺ bridging two H₂O molecules (H₂O-H⁺-OH₂), and the surface CO₂ and H atom.

Neurock *et al.*,⁴¹ studied FA electrocatalytic oxidation in the presence of solution and applied electrochemical potential using periodic DFT method (GGA-RPBE) and a 3-layer (two relaxed top layers and one fixed bottom layer) slab in a 3×3 unit cell with 10 Å vacuum gap. In

their calculation, the aqueous phase was modeled by using 24 explicit solvent molecules chosen to fill up the vacuum region, and one H₂O molecule on the surface was therefore replaced with reactant, intermediate and product species.

All three FA oxidization routes were examined using DFT together with the double-reference method in order to determine their potential dependence reaction energies and activation barriers. It shows that FA has two adsorbed structures in solution, i.e.; (a) FA bonds to surface in the **O/OH-down** adsorption configuration; and (b) FA lays parallel to surface in the **H₂COH-flat** adsorption configuration. While the **O/OH-down** adsorption configuration is more favourable in gas phase, both adsorption configurations in solution are energetically nearly equivalent. FA readily reacts from the upright mode to form a surface HCOO intermediate and proton. The HCOO intermediate has the bidentate **O/O-down** adsorption configuration, which is quite rigid with the C–H bond oriented along the surface normal, thus making it very difficult to activate the C–H bond. The C–H bond dissociation from this state requires bending the C–H group out of the OCO plane (dynamic bending mode), which costs over 1 eV in energy. Alternatively, the molecule can reorient itself to be bound through one of the oxygen atoms and the hydrogen atom, and this also costs over 1 eV in energy at positive potentials as it requires breaking the very highly polarized Pt–O bond.

Table 1.1 Computed activation energies (eV) and the reaction energies (eV, in the bracket) [41]

	0.0 V-NHE	0.5 V-NHE	1.0 V-NHE
formate route			
HCO ₂ H → HCOO + H	~0.05 (–0.78)	(–1.00)	~0.00 (–1.21)
HCOO → CO ₂ + H	1.20 (–0.09)	1.10 (–0.86)	1.00 (–1.59)
direct route			
HCO ₂ H → COOH + H	0.50 (–1.37)	0.47 (–1.60)	0.42 (–1.81)
COOH → CO ₂ + H	0.52 (–0.50)	(–0.26)	~0.50 (–0.99)
indirect route			
HCO ₂ H → CO + H ₂ O	~1.00 (–2.06)	~1.00 (–2.06)	0.50 (–2.16)
CO + H ₂ O → CO ₂ + 2H	1.42 (1.19)	0.99 (0.20)	0.57 (–0.64)

In order to establish the potential dependence of all the three routes, and compare with the experiment and clarify path ultimately controlling the chemistry as well as the energetic changes caused by different potentials, three different potentials (0.0, 0.5 and 1.0 V NHE) were considered in their calculation. The activation energies and the reaction energies are shown in Table 1.1. Compared to the formate route which needs very high barrier for HCOO dissociation, and the indirect route which also needs higher barrier for CO formation and subsequent oxidation, the direct route proceeds via the initial activation of the C–H bond, and the

corresponding barrier is 0.5 eV at 0 V and drops down to 0.4 eV at higher potentials. The barrier to activate the O–H bond is very low over a range of potentials, and is thus readily activated to form CO₂ directly. Based on the calculated activation barriers, this direct route appears to be dominant to form CO₂ and requires the presence of step or defect sites

On the basis of the solvation model of Neurock *et al.*,⁴¹ Zhong *et al.*, studied FA oxidation on Pt(111)⁴² and bimetallic PtAu(111)⁴³ (one Pt atom of Pt(111) outmost layer was replaced by one Au atom) using periodic DFT method (GGA-PBE) and a 3-layer (one relaxed top layer and two fixed bottom layers) slab model in a 3×3 unit cell with 10 Å vacuum gap. They found that on Pt(111) the direct route (HCOOH → CO₂ + 2H) has energy barrier of 0.25 eV, the indirect route (HCOOH → H + COOH → CO + H₂O) has effective energy barrier of 1.43 eV. They also proposed a dimer route which involves the simultaneous formation of CO₂ and CO in an elementary step (2HCOOH → CO₂ + 2H + CO + H₂O) and the computed energy barrier is 0.66 eV, which is comparable with that of the direct route but much lower than that of the indirect route. This proposed mechanism rationalizes the easy CO poisoning of Pt-based catalysts and improves the understanding of FA catalytic oxidation. On PtAu(111), they found that the direct route is much more favorable than the indirect route (0.67 vs. 4.31 eV).

Wang and Liu⁴⁴ investigated FA oxidation at Pt/H₂O interface using periodic DFT method (GGA-PBE). They used a continuum solvation model to simulate the reactions at the metal/H₂O interface and a 4-layer (two relaxed top layers and two fixed bottom layers) slab in a 4×2√3 unit cell with 15 Å vacuum gap. They found that the **O/CH-down** adsorption configuration is most stable in the presence of H₂O environment, but it is very difficult for dissociate C-H and the calculated barrier is around 1 eV. For the formate intermediate, it prefers the bidentate adsorption configuration (**O/O-down**), and further C-H dissociation also is not favorable in activation energy barrier (1.1 eV) in the presence of H₂O environment. In the presence of pre-adsorbed formate, however, FA can adsorb with the **CH-down** adsorption configuration near the formate, and in this configuration the C-H dissociation of FA becomes easily with low barrier (0.45 eV), and the dissociation of COOH into CO₂ is rapidly by the transfer of proton to water. This finding reveals that the pre-adsorbed formate is a co-catalyst for FA direct oxidation, instead of being an active intermediate for CO₂ production or a site-blocking species.

Peng *et al.*,⁴⁵ reported the mechanism of FA electro-oxidation on Sb-modified Pt (Sb/Pt) electrode on the basis of in-situ electrochemical surface-enhanced infrared absorption spectroscopy and periodic DFT calculations (GGA-PBE). They used their previous model systems,⁴⁴ and for Sb modification they put all Sb atoms initially at the face-centered cubic hollow sites of Pt(111), and indeed, the hollow site is also the most stable adsorption site. Their calculations show that the presence of Sb on Pt(111) favours FA adsorption via the **CH-down** adsorption configuration, while inhibits the previously mentioned **O/CH-down** adsorption configuration. This **CH-down** adsorption configuration facilitates kinetically the

complete FA oxidation into CO₂. They also show that such Sb modification can weaken CO adsorption energy on the Pt site, and consequently help to relieve CO poisoning on the Pt electrode.

Gao *et al.*,⁴⁶ studied FA oxidation on the Pt(111) surface in gas phase with and without co-adsorbed water molecule by using periodic DFT method (GGA-PBE) and a 5-layer slab (three relaxed top layers and two fixed bottom layers) in (3×3) and (2×2) unit cells (for 1/9 and 1/4 monolayer coverage (ML), respectively), with 13 Å vacuum gap. Under the co-adsorption of one water molecule, they found two stable adsorption configurations in close energy, **O/OH-down** and **cis-HCO₂H-flat** as also reported by Neurock.⁴¹ They found that formate is a reactive intermediate for CO₂ in FA oxidation in gas phase, and the co-adsorbed water can catalyze FA oxidation by reducing the O-H dissociation barrier, modify the surface structures of FA and formate on Pt(111) and promote the C-H dissociation. They also found that increasing the surface coverage from 1/9 to 1/4 ML reduces the key activation barriers (the effective barrier from the bidentate formate to the C-H dissociation transition state) so that FA oxidation becomes even more favourable. In addition, they also reported that FA dissociation from the flat adsorption configuration via the formate route is not competitive to the perpendicular one with one co-adsorbed water molecule at 1/4 ML. The indirect route via COOH intermediate is also found not competitive to the formate route.

Using the same methodology Gao *et al.*,⁴⁷ also reported DFT study of FA electrochemical oxidation on Pt(111) under the consideration of two solvation models, **model A** with two explicit water molecules per surface unit cell to describe the interfacial waters; and **model B** having a water bilayer consisting of a fully periodic ice-like network of water molecules was used to describe the solid/liquid interface. In **model A**, they found that the most stable FA adsorption configuration is the same as found in gas phase (**O/OH-down**); and the two co-adsorbed water molecules do not affect the adsorption structure and energy. In **model B**, FA is incorporated into this surface and can substitute two water molecules in the bilayer in two different co-adsorption configurations in close energy, and both configurations can have strong hydrogen bonding between FA and the surrounding water molecules. Such co-adsorption configurations are different from those proposed by Wang and Liu.⁴⁴ Their computed minimum energy pathway suggests that the formate route is always preferred over the direct route on clean surface, but at potential higher than 0.3V, both the formate and direct routes are nearly identical in energy, therefore it is hardly to draw the decisive conclusions on the predominant route under electrochemical conditions. Very recently, Gao *et al.*,⁴⁸ reported the role of the adsorbed CO and OH in FA electro-oxidation on Pt(111) under the consideration of the direct and formate routes. Their results show that the adsorbed CO adversely affects FA oxidation, while the adsorbed OH does not. As to the co-adsorbed CO and OH, a synergistic co-effect was found in promoting FA oxidation.

FA decomposition on Pt(111) in gas phase has also been computed by Kang *et al.*,¹³ and in

their calculations they used periodic DFT method (GGA-PBE) and a 4-layer slab (two relaxed top layers and two fixed bottom layers) in a (4×2) unit cell (1/8 ML) with 15 Å vacuum gap. Despite of their quite similar computational methodologies, Gao *et al.*,⁴⁶ and Kang *et al.*,¹³ reported different results for FA decomposition on Pt(111) in gas phase (Table 1.2).

Table 1.2 Computed adsorption (E_{ads} , eV) and reaction energy (E_r , eV) as well as activation barrier (E_a , eV) of different steps for FA dissociation

formate route Pt(111)			
	1/9 ML ⁴⁶	1/4 ML ⁴⁶	1/8 ML ¹³
E_{ads} (HCOOH _(g))	-0.40	-0.34	-0.26
E_a (HCO ₂ H → HCOO + H)	0.94	0.88	0.72
E_a (HCOO → CO ₂ + H)	1.56	1.16	1.23
E_r (HCOOH _(g) → CO _{2(g)} + 2H)	-0.32	-0.38	-0.83
formate route Pt ₃ Pb(111)			
E_{ads} (HCOOH)			-0.23
E_a (HCO ₂ H → HCOO + H)			0.36
E_a (HCOO → CO ₂)			0.90
formate route core-shell Pt ₃ Pb-Pt(111)			
E_{ads} (HCOOH)			-0.41
E_a (HCO ₂ H → HCOO + H)			0.55
E_a (HCOO → CO ₂ + H)			1.16
COOH route Pt(111)			
E_a (HCOOH → COOH + H)	1.83	1.58	0.72
E_a (COOH → CO ₂ + H)	1.15	0.90	0.71
E_a (COOH + H → CO + H ₂ O)	1.53	1.39	
COOH route Pt ₃ Pb(111)			
E_a (HCOOH → COOH + H)			0.57
E_a (COOH → CO ₂ + H)			0.61
COOH route Pt ₃ Pb-Pt(111)			
E_a (HCOOH → COOH + H)			0.58
E_a (COOH → CO ₂ + H)			0.56

For example, the adsorption energy of FA at 1/8 ML (-0.26 eV) is lower than those at 1/9 and 1/4 ML (-0.40 and -0.34 eV, respectively), the O-H dissociation barrier at 1/8 ML (0.72 eV) is lower than those at 1/9 and 1/4 ML (0.94 and 0.88 eV, respectively). Large differences are found for effective barrier of formate dissociation, 1.23 eV at 1/8 ML, while 1.56 eV at 1/9 ML and 1.16 eV at 1/4ML. Even larger difference has been found for the C-H dissociation of FA to form COOH intermediate, e.g.; the activation barrier is 0.73 eV at 1/8 ML, while 1.83 eV

at 1/9 ML and 1.58 eV at 1/4 ML.

Since no structural parameters of the transition state were given in their respective articles, it is really not easy to speculate the origins of these differences despite of their very similar models and methods. It is noted that Gao *et al.*, used CASTEP⁴⁹ software, while Kang *et al.*,¹³ used VASP⁵⁰ package. However it is hardly be believe that such huge differences come from different software packages. Indeed, Cao *et al.*,⁵¹ used four different functional methods, i.e.; PAW-PBE and USPP-PW91 with VASP, and USPP-PBE and USPP-PW91 with CASTEP to calculate the hydrogenation and the respective C-C coupling reactions of carbon species on the Fe₅C₂(001) surface and found that all four methods give very close structural as well as kinetic and thermodynamic parameters.

Kang *et al.*,¹³ reported FA oxidation on the pure metallic Pt, the bimetallic Pt₃Pb nanocrystals and the Pt₃Pb-Pt core-shell nanocrystals (Table 1.2). On Pt(111), they found that the direct route of FA decomposition is more favourable over the formate route, especially in the second step of CO₂ formation from COOH ($E_a = 0.71$ eV) and HCOO ($E_a = 1.23$ eV) dissociations, although they have the same activation barriers for the first step to form COOH and HCOO ($E_a = 0.72$ eV). On the Pt₃Pb nanocrystals, the barrier of the first step of formate route ($E_a = 0.36$ eV) is lower than that of the first step of direct route ($E_a = 0.57$ eV), the barrier of the second step of formate route ($E_a = 0.90$ eV) is higher than that of the second step of the direct route ($E_a = 0.61$ eV), indicating that formate “poisoning” could be worse on the Pt₃Pb(111) surface, and therefore, the direct route can be favourable. On the Pt₃Pb-Pt core-shell nanocrystals, nearly the same results as on Pt(111) have been found, and the direct route is favourable, especially in the second step of CO₂ formation from COOH ($E_a = 0.56$ eV) dissociation and HCOO ($E_a = 1.16$ eV) dissociation. Their combined experimental and theoretical studies suggested that the high activity of the Pt₃Pb nanocrystals and the Pt₃Pb-Pt core-shell nanocrystals results from the elimination of CO poisoning and the decreased barriers for the dehydrogenation steps. However, they did not investigate the indirect route for comparison. Although the results by Gao *et al.*,⁴⁶ favour the formate route, the results of Kang *et al.*,¹³ favour the direct route for FA decomposition on the pure Pt(111) surface.

Compared to Pt(111), they found that both types of nanocrystals can reduce the activation for the O-H bond dissociation in FA and the C-H bond dissociation in formate. They also found that both types of nanocrystals can reduce the C-H dissociation barrier in FA to form COOH and the O-H dissociation in COOH to form CO₂. On all the three surfaces the direct route for FA decomposition is favourable, and the most active catalyst is the Pt₃Pb-Pt core-shell nanocrystals.

1.2.2 Palladium

As platinum is well established to be most active for FA decomposition in gas phase,⁵² palladium has been reported to be most active for FA electrocatalytic oxidation in aqueous phase.⁵³ Compared to Pt, much less theoretical studies about FA decomposition on Pd are known.

FA decomposition on Pd(111) was reported by Zhou *et al.*,⁵⁴ by using periodic DFT method (GGA-PBE) and slab model. They used a 3-layer slab (top layer relaxed and two bottom layers fixed) in a (3×3) unit cell (1/9 ML) with 10 Å vacuum gap. In contrast to Pt(111), FA on Pd(111) has a flat adsorption configuration (**HCO₂H-flat**) with adsorption energy of −0.40 eV, while the expected **O/OH-down** configuration is 0.14 eV less stable. The computed activation barrier of the O-H bond dissociation into surface formate and H is 0.21 eV. However, these results by Zhou *et al.*, could not be reproduced by Luo *et al.*⁵⁵ In their calculations, they used the same model and method and found that the most stable adsorption configuration of FA is the expected **O/OH-down** configuration with adsorption energy of −0.39 eV, and the computed O-H bond dissociation barrier is 0.58 eV; and all these are roughly the same as on the Pt(111) surface. In contrast, the reported flat adsorption configuration (**HCO₂H-flat**) by Zhou *et al.*,⁵⁴ could not be located and reproduced despite of intensive searches by Luo *et al.*.

For formate adsorption, Zhou *et al.*,⁵⁴ calculated four adsorption configurations, and the most stable one has one oxygen atom in η^3 -capping over the Pt face centred cubic surface (η^3 -**O-down**) (−0.67 eV), followed by the bidentate structure (**O/O-down**) (−0.60 eV) of two oxygen atoms as well as the monodentate oxygen atom bridging (η^2 -**O-down**) (−0.54 eV) and atop (−0.39 eV) structures (η^1 -**O-down**). However, these results by Zhou *et al.*, disagree with the results from the combined experimental and theoretical studies by Zheng *et al.*⁵⁶ They reported that the bidentate structure (**O/O-down**) is the only stable adsorption configuration, and the experimentally determined geometrical parameters of the adsorbed formate on Pd(111) from low-energy electron diffraction (LEED) are in very close agreement with the results from the periodic DFT calculations using a 4-layer slab (two top layers relaxed and two bottom layers fixed) in (3×3) a unit cell (1/9 ML) with 14 Å vacuum gap. The same results for the bidentate structure (**O/O-down**) formate as the most stable adsorption configuration has also been reported by Luo *et al.*,⁵⁵ and the calculated adsorption energy is −2.37 eV, which is more stable than the η^3 -capping face centred cubic structure (η^3 -**O-down**) (−1.67 eV), and this is just the opposite to the results of Zhou *et al.*.

For the C-H bond dissociation of the adsorbed formate into CO₂, Zhou *et al.*, calculated the barriers for all four adsorption configurations and the highest barrier is found for the face centred cubic adsorption configuration (η^3 -**O-down**) (0.52 eV), and the lowest barrier is found for the monodentate oxygen atom bridging configuration (η^2 -**O-down**) (0.17 eV), and the transformation barrier between these two adsorption configurations is 0.06 eV. Therefore, a two-step C-H bond dissociation of formate is more favourable than the one step alternative. In contrast to Zhou *et al.*, Luo *et al.*,⁵⁵ found a transition state for C-H dissociation with one oxygen atom interacting with surface Pd and the C-H bond also pointing to the surface (**O/H-down**) with adsorption energy of −1.66 eV; and the calculated effective barrier is 0.76 eV, starting from the most stable bridging bidentate adsorption configuration (**O/O-down**) of formate.

Recently, Hu *et al.*,⁵⁷ systematically studied FA adsorption and dissociation on M(111), M = Pt, Pd, Rh, Au, by using periodic DFT method (GGA-PBE-USPP) and a 4-layer slab model (two top layers relaxed and two bottom layers fixed) in a (3×3) unit cell (1/9 ML) with 15 Å vacuum gap. They found the same favourable route as reported by Gao *et al.*⁴⁶ on Pt(111), i.e.; FA has the **O/OH-down** configuration and dissociates into surface formate in the **O/O-down** configuration, and the adsorbed HCOO dissociates via a meta stable configuration (**O-down**) into CO₂ and surface H. For FA adsorption, the computed adsorption energy is -0.39, -0.40, -0.46 and -0.15 eV for Pt, Pd, Rh and Au, respectively, and the corresponding dissociation barrier into surface formate and hydrogen (HCOOH → HCOO + H) is 0.69, 0.68, 0.08, 1.36 eV for Pt, Pd, Rh and Au, respectively. For the rate-determining step of formate dissociation (HCOO → CO₂ + H), they found that Pt(111) and Rh(111) have close effective barriers (1.88 and 1.92 eV, respectively), and they are higher than the effective barriers (1.59 and 1.56 eV, respectively) for Pd(111) and Au(111).

For describing the reaction in aqueous solution, they considered HCOO⁻/HCOO as reactant, which can have spontaneously C-H dissociation on Pt, Pd and Rh. On Au, however, they did not find C-H dissociation, and the reaction was expected to take place as in gas phase. Therefore they concluded that the focus of FA dissociation in solution catalysed by Pt, Pd and Rh is the formation of H₂ from surface H atoms.

Table 1.3 FA adsorption energy (E_{ads} , eV) and dissociation barrier (E_{a} , eV) on Pd(111)

	Pd(111) ⁵⁵	Pd(111) ⁵⁷	Pd (111) ⁵⁸	Pd(111) ⁵⁹
E_{ads} (HCOOH)	-0.39	-0.40	-0.62	-0.40
E_{a} (HCOOH → HCOO + H)	0.58	0.68	1.00	0.49
E_{a} (HCOO → CO _{2(g)} + H)	0.76	1.59	0.88	0.77

In addition, FA dissociation on Pd(111) was also systematically studied by Zhang *et al.*,⁵⁸ and Yuan *et al.*⁵⁹ Zhang *et al.*, used periodic DFT method (GGA-PW91) calculations and a 3-layer slab model (one top relaxed layer and two fixed bottom layers) in a (3×3) unit cell (1/9 ML) with 10 Å vacuum gap. For the same reaction route, they reported that the rate-determining step is FA dissociation into surface formate and hydrogen (HCOOH → HCOO + H) instead of formate dissociation into CO₂ and hydrogen (HCOO → CO₂ + H), and the computed barrier is 1.00 and 0.88 eV, respectively, and they differ strongly from the reported values (0.68 and 1.59 eV, respectively) by Hu *et al.*⁵⁷ In their calculations (GGA-PBE) on FA dissociation on Pd(111) with a 4-layer (two relaxed top layers and two fixed bottom layers) slab model in a 3×3 unit cell with 15 Å vacuum gap, Yuan *et al.*⁵⁹ reported the corresponding barrier for FA dissociation into surface formate and hydrogen as well as formate dissociation into CO₂ and hydrogen is 0.49 and 0.77 eV, respectively, and these data are close to those (0.58 and 0.76 eV, respectively) reported by Luo *et al.*⁵⁵ In addition, Yuan *et al.*⁵⁹ also

reported the competitive behaviour of FA dissociation on Pd(111) into COOH+H (0.56 eV) and COOH dissociation into CO+OH (0.60 eV) or CO₂+H (0.80 eV). Such controversial results about FA dissociation on Pd(111) are summarized in Table 1.3, and it shows clearly that it is not possible to have a general picture for FA dissociation on Pd(111).

Along with the Pd(111) surface, Yuan *et al.*,⁵⁹ also investigated FA adsorption and dissociation on Pd atom modified Au(111) surfaces, (i) all nine first layer Au atoms of Au(111) are fully replaced by nine Pd atoms (Pd ML), (ii) six of the nine Au atoms on Au(111) are replaced by six Pd atoms (Pd₆Au₃); (iii) three of the nine Au atoms on Au(111) are replaced by three Pd atoms (Pd₃Au₆). Compared to the clean Pd(111), FA dissociation on Pd ML and Pd₆Au₃ into either HCOO and COOH becomes more competitive, while COOH formation on Pd₃Au₆ is more favored kinetically than HCOO formation. For the selective dissociation of COOH into either CO+OH or CO₂+H, Pd(111) and Pd ML favor CO+OH formation kinetically by 0.20 and 0.25 eV, respectively; while Pd₆Au₃ and Pd₃Au₆ favor CO₂+H formation by 0.15 and 0.11 eV, respectively. These results indicate that a proper arrangement of Au and Pd sites can significantly improve electrocatalytic activity of PdAu catalyst for FA oxidation attributed to the reduction of CO poisoning.

Apart from bulky Pd as catalyst, Li *et al.*,⁶⁰ computed FA dissociation on a Pd₇ cluster at the B3LYP level of density functional theory under the consideration of solution effect of water by means of the polarizable continuum model in the self-consistent reaction field method. FA adsorption on Pd₇ in gas phase and solution has the **O/OH-down** configuration and the calculated adsorption energy is -0.49 and -0.83 eV, respectively. In gas phase, FA prefers to dissociate into formate (**O/O-down**) and H with activation energy of 0.41. The surface formate (**O/O-down**) first goes through a meta-stable configuration (**O/H-down**) and dissociates into CO₂ and H, the effective barrier is 0.91 eV. In solution, FA first also dissociates into formate (**O/O-down**) and H with activation energy of 0.06 eV, and the direct dissociation of formate in the **O/O-down** configuration into CO₂ and H is the dominating route with activation energy of 0.61 eV. In addition, they also computed the alternative COOH route for CO₂ formation and the direct route for the formation of CO+H₂O in both gas phase and solution, and the formate route is found to be most favourable.

1.2.3 Nickel

Not only Pt and Pd but also Ni has been used for FA decomposition. Recently Luo *et al.*,⁵⁵ computed FA decomposition on Ni(111) by using spin-polarized periodic DFT method (GGA-PBE). They used a 3-layer slab (two top relaxed layers and one fixed bottom layer) in a (3×3) unit cell (1/9 ML) with 15 Å vacuum gap. They reported the (**O/OH-down**) adsorption configuration of FA to be most stable, and the calculated adsorption energy is -0.36 eV. For the O-H bond dissociation the calculated activation barrier is 0.41 eV. For formate decomposition, they suggested a multi-step process, i.e. the most stable bidentate bridging adsorption configuration (**O/O-down**) transforms into the threefold capping structure (**O-down**) with

barrier of 0.67 eV; and then subsequent transformation into the bridging bidentate structure (**O/H-down**) with barrier of 0.36 eV. The last step is the decomposition of formate (**O/H-down**) with energy barrier of 0.10 eV. Based on their calculations, the dissociation of the hydrogen atom from formate to surface CO₂ and H is the rate determining step with effective energy barrier of 1.03 eV. In addition, they found very well agreement between the calculated vibrational frequencies for the adsorbed FA, formate as well as deuterated FA and formate and the experimentally observed IR data, and these agreements validate their model and method. They also made general comparison for FA decomposition among Ni(111), Pd(111) and Pt(111), and found very high similarity in adsorption configurations and energetic parameters.

As the back reaction of FA decomposition, the potential energy surface of CO₂ hydrogenation into FA has been computed by Peng *et al.* on the Ni(111)⁶¹ and Ni(110) surfaces.⁶² In their calculations, Peng *et al.* used spin-polarized periodic DFT method (GGA-PW91) and a 5-layer (three relaxed top layers and two fixed bottom layers) slab with a 3×3 surface unit cell and the vacuum gap was set up to equivalent of 6 atomic layers for Ni(111), and a 7-layer (four relaxed top layers and three fixed bottom layers) slab in a 2×3 surface unit cell and the vacuum gap was set to 12 Å for Ni(110). For CO₂ hydrogenation to FA on Ni(111), the energetic parameters for the elementary steps are nearly the same as found for FA decomposition by Luo *et al.*⁵⁵

Peng *et al.*, found that CO₂ is only weakly physisorbed on Ni(111), whereas much more strongly (−0.47 eV) on Ni(110), which is close the value (−0.42 eV) reported by Wang *et al.*⁶³ For formate formation, the computed activation barrier on Ni(111) is higher than on Ni(110) (0.62 vs. 0.41 eV), as well as the activation barrier for formate hydrogenation to FA on Ni(111) is lower than on Ni(110) (0.83 vs. 1.03 eV). For CO₂ hydrogen on Ni(110), Vesselli *et al.*, reported a combined experiment and computation study, and their calculations show that the barrier for formate formation is 0.43 eV,⁶⁴ close to the reported value by Peng *et al.*, and the barrier for formate hydrogenation to FA is 0.80 eV,⁶⁵ lower than the reported value by Peng *et al.*

Peng *et al.*, also investigated CO₂ hydrogenation from subsurface H, and found that subsurface H has essentially no effect on the energetics of CO₂ hydrogenation. For both Ni(111) and Ni(110), subsurface H is significantly less stable than surface H, and as a result, the thermochemistry of the reaction between subsurface and adsorbed CO₂ to adsorbed FA becomes exothermic, whereas the reaction between surface H and adsorbed CO₂ to adsorbed FA is endothermic. Therefore, on both surfaces the reaction with transient energetic bulk H emerging to the surface might be more driven than the respective reaction with surface H.

1.2.4 Copper

FA decomposition on the clean and oxygen pre-covered Cu(111) surfaces was studied by Wang *et al.*,⁶⁶ using a periodic DFT method (GGA-PBE). In their calculations they used a 3-layer slab separated by 10 Å of vacuum gap with a 3×2 unit cell (1/6ML). On clean Cu(111),

FA has the **O/OH-down** adsorption configuration, and formate has the **O/O-down** adsorption configuration as well as the H atom locates at the nearest face centred cubic site. The calculated O-H dissociation barrier from FA to formate is 0.62 eV. On oxygen pre-covered Cu(111) surface, the O-H dissociation barrier (0.11 eV) decreases drastically compared to the clean surface. On the Cu(111) and Cu(110) surfaces, Wang *et al.*,⁶⁷ computed CO₂ hydrogenation to formate and found that formate synthesis on these two surfaces are structure-insensitive with close activation energies (0.69 and 0.64 eV, respectively), and this is because that the gas phase CO₂ interacts directly with the surface atomic hydrogen to form the less stable monodentate formate instead of the pre-required adsorption on the surface and the structural similarity between the transition state and the adsorbed monodentate formate. In contrast, formate decomposition barriers on Cu(111) and Cu(110), starting from the more stable bidentate adsorption configuration, differ significantly (0.97 and 1.44 eV, respectively), indicating their structure-sensitivity. In addition, the conversion of the bidentate formate to the monodentate format is structure-sensitive because of their significantly different adsorption energies on Cu(111) and Cu(110) of -0.69 and -1.20 eV, respectively. Using periodic DFT method (GGA-PBE) and a 3-layer slab separated by 10 Å of vacuum gap with a 3×3 unit cell Mei *et al.*,⁶⁸ computed the decomposition of formate on Cu(111) into CO₂(g) + H, CO(g)+OH, CO+OH and HCO+O, and found that the formation of CO₂ has the lowest activation energy among these four reactions (1.30, 2.80, 3.01 and 1.70 eV, respectively).

1.2.5 Gold

Beltramo *et al.*,⁶⁹ investigated FA oxidation on gold electrodes with a combination of electrochemistry, in situ surface-enhanced Raman spectroscopy and differential electrochemical mass spectrometry as well as first-principles DFT calculations. In their calculations, they used a 4-layer slab in a (2×2) unit cell and the vacuum gap was equivalent to 6 atomic layers to model the Au(110) and Au(100) surfaces; and all slab atoms were fixed in the calculations and only the adsorbates (FA and formate) were fully optimized. They found that formate is the relevant surface-bonded intermediate during FA oxidation; and at low potential formate can interact with a nearby water to produce CO₂ and hydronium ion, and at high potential formate can interact with a surface-bonded hydroxyl to give CO₂ and water. There is no evidence for CO formation on gold during FA oxidation.

The above discussion and comparison show the increasing theoretical importance in catalytic FA dissociation from monometallic clean surfaces to bimetallic or even trimetallic surfaces as well as to small-sized metal clusters in both gas phase and solution. Despite of the interesting and plentiful results, it is still controversial about the favourable reaction mechanisms for FA catalytic dissociation, in particular for the Pt and Pd systems. For example, what is the most favourable reaction route with its intermediates and elementary steps, and which step has the highest (effective) barrier?⁷⁰

1.3 Metal oxides

FA adsorption and decomposition on metal oxides have been intensively studied as a prototypical system of catalytic reactions at metal oxide surfaces. It has been well established that FA decomposes to a formate anion and an acidic proton that forms a surface hydroxyl group (OH). The selective dehydrogenation and dehydration depend strongly on the nature of substrates and reaction conditions.

1.3.1 Titanium oxide

Surface chemistry of TiO_2 plays a key role in the development and optimization of solar power, catalysis, gas sensing and medical implantation as well as corrosion protection. The chemical reactivity of water, oxygen and carboxylic acids as well as alcohols on TiO_2 , mainly on rutile $\text{TiO}_2(110)$, was reviewed by Pang *et al.*⁷¹

Using an ab initio Hartree-Fock (HF) crystalline orbital method as well as both polymer and slab models Ahdjoudj and Minot⁷² reported FA adsorption and dissociation on the rutile $\text{TiO}_2(110)$ surface. TiO_2 is an amphoteric oxide which contains metallic cations as acidic sites and oxygen anions as basic sites at the surface. They found dissociative FA adsorption, and the formate anion is bound to the surface titanium atoms forming the bridging bidentate adsorption configuration (**O/O-down**) and the proton is bound to the bridging oxygen atom forming the surface OH group. FA dissociative adsorption on $\text{TiO}_2(110)$ was also found by Bates *et al.*,⁷³ and by Käckell and Terakura.^{74,75} using a slab model at the DFT level (GGA-USPP). FA dissociative adsorption on both stoichiometric and defective $\text{TiO}_2(110)$ surfaces with the formation of the bridging bidentate adsorption configuration (**O/O-down**) was also found by Wang *et al.*⁷⁶ from their combined experimental (X-ray photoelectron spectroscopy and ultraviolet photoemission spectroscopy) and theoretical (HF/3-21G* on a cluster model) studies.

Vittadini *et al.*,⁷⁷ carried out periodic DFT (GGA-USPP) calculation on FA adsorption on the anatase $\text{TiO}_2(101)$ and $\text{TiO}_2(001)$ surfaces. On the dry $\text{TiO}_2(101)$ surface,⁷⁸ FA has a molecular monodentate adsorption configuration with the hydrogen of the O-H group bonded to a surface bridging oxygen atom, while on the hydrate $\text{TiO}_2(101)$ surface, FA has dissociative adsorption and the formed formate anion has a monodentate adsorption configuration due to the interaction with a nearby water molecule. These results were also confirmed by Miller *et al.*,^{79,80} from their study on the effect of water on the adsorbed FA structures on the anatase $\text{TiO}_2(101)$ surface. FA dissociative bidentate adsorption was also found on the step D-(112) and step B-(100) edges by Gong *et al.*,⁸¹ and on the clean and partially hydrated $\text{TiO}_2(001)$ surfaces by Gong *et al.*,⁸² as well as on the brookite $\text{TiO}_2(210)$ surface by Li *et al.*⁸³

Nunzi and De Angelis⁸⁴ reported their DFT calculations on FA adsorption on the single-wall TiO_2 nanotubes using cluster models, and studied the surface curvature effect under the comparison with the results on the planar $\text{TiO}_2(101)$ anatase slab. On the slab model, they found FA in both molecular monodentate adsorption configuration and bidentate bridging

configuration for dissociative adsorption close in adsorption energy (-1.16 vs. -1.13 eV), suggesting a possible co-existence of molecular FA and dissociated formate on the surface. While on the curvature of the nanotubes, the molecular monodentate adsorption is energetically more favored than the dissociated bidentate adsorption configuration, e.g.; -1.19 vs. -0.45 eV on the (12, 0) tube; and -1.35 vs. -1.08 eV on the (0, 4) tube.

FA selective decomposition on the rutile $\text{TiO}_2(110)$ surface depends on the reaction temperature and gas phase pressure. For FA dehydration ($\text{HCOOH} \rightarrow \text{CO} + \text{H}_2\text{O}$) on rutile $\text{TiO}_2(110)$, Iwasawa *et al.*,⁸⁵ used periodic DFT method (GGA-PBE). On the stoichiometric surface FA dissociates to surface formate and hydroxyl spontaneously, but simple unimolecular decomposition of formate into CO is energetically unfavorable and is quite improbable. However, O vacancy can promote this decomposition process, and during the catalytic process the first step includes FA dissociative adsorption, condensation of HO_B at the bridge oxygen to form H_2O and to create an O vacancy, and the second step involves formate decomposition at the O vacancy and healing of the vacancy by OH to complete the catalytic cycle. Therefore two bridging OH groups from two dissociatively adsorbed FA are necessary to form one H_2O and one vacancy and one formate should always accompany one HO_B . This proposed reaction mechanism was supported by the subsequent *in situ* scanning tunnelling microscopic study by Aizawa *et al.*⁸⁶

For FA dehydrogenation ($\text{HCOOH} \rightarrow \text{CO}_2 + \text{H}_2$) on the rutile $\text{TiO}_2(110)$ Uemura *et al.*,⁸⁷ used periodic DFT method (GGA-PBE in combination doubled numerical basis set plus polarization function and effective potentials). They found that that the activation energy for the dehydrogenation process depends the charges of the reacting H atom of adsorbates (FA and HCOO^-) and the amount of the adsorption energy available at the transition state. The most plausible reaction pathway is the one between a bridging formate adsorbed on two 5-fold coordinated Ti^{4+} ions and a FA molecule weakly adsorbed at the adjacent Ti^{4+} ion. The dehydrogenation occurs by acid-base interaction between the two adsorbates, indicating that this process does not require a special site such as an oxygen defect, which is the active site for unimolecular FA dehydration. Thus, the different decomposition process, dehydrogenation or the dehydration, is due to the two different active sites on the surface; i.e.; three adjacent surface Ti^{4+} ions on the stoichiometric surface for the bimolecular dehydrogenation and on the oxygen defect sites for the unimolecular dehydration.

The molecular mechanism of the selective dehydrogenation and dehydration of FA on $\text{V}_2\text{O}_5/\text{TiO}_2$ has been computed by Avdeev *et al.*,⁸⁸ using periodic DFT method (GGA-PBE-USPP). For the dehydrogenation step, they found FA dissociative adsorption through the oxygen atom of the O=C group to produce monodentate formate on the V^{5+} center and surface V-OH acid sites as the initial step of reaction pathway leading to $\text{CO}_2 + \text{H}_2$, and the rate-determining step corresponds to migration of the basic H atom of the C-H group to the acidic H atom of V-OH acid site. For the dehydration pathway, FA is also adsorbed on the

V⁵⁺ centre, but via the oxygen atom of the O-H group, followed by the synchronous formation of surface OH as rate-determining step and the evolution of CO molecules into the gas phase, and this path is completed by recombination of two V-OH surface hydroxyl groups to form adsorbed H₂O. Initialization of both dehydrogenation and dehydration pathways of FA decomposition on the VOx/TiO₂ surface occur on the same Lewis acids sites V⁵⁺ but proceed through different intermediates; and the dehydration process is more preferable than the dehydrogenation process on the basis of the computed activation energies (1.26 vs. 1.38 eV) of the corresponding rate-determination steps.

1.3.2 Magnesium oxide

Nakatsuji *et al.*,⁸⁹ reported FA molecular adsorption on the MgO(001) surface by using ab-initio molecular orbital method (HF and MP2) and a Mg₈O₈ cluster model. The most stable adsorption configuration has dissociated formate anion in bidentate form bridging the Mg atoms and the proton sat on one oxygen atom (**O/O-down**), and the calculated dissociation barrier is 1.24 eV for *cis*-FA and 0.56 eV for *trans*-FA at the MP2 level. Similar results have been found by Szymański and Gillan⁹⁰ using periodic DFT method (GGA-PW) on the flat non-defective MgO(100) surface for FA adsorption and dissociation.

Lintuluoto *et al.*,⁹¹ calculated FA decomposition on the perfect and defect Mg(100) surfaces by using ab-initio molecular orbital method (HF and MP2) and a Mg₈O₈ cluster model, and they found that FA decomposition does not occur on the perfect surface, but it is feasible on surface O²⁻ vacancy to form CO and H₂O. At the UMP2 level, the energy barrier is 1.23 eV, and the overall reaction is endothermic by 2.12 eV.

1.3.3 Zinc oxide

FA adsorption and decomposition on the ZnO(10 $\bar{1}$ 0) surface were computed at different levels and using different models. Nakatusji *et al.*,⁹² computed the chemisorption and surface reaction of FA on ZnO(10 $\bar{1}$ 0) using a Zn₄O₄ cluster embedded in an electrostatic field represented by 464 point charges at the crystal ZnO lattice position at the HF and MP2 levels of theory. They found a more stable bridging bidentate adsorption configuration for *cis*-FA, which needs a small barrier (0.51 eV at HF) to dissociate into surface formate in the bridging bidentate adsorption configuration (**O/O-down**) and OH, and this process is highly exothermic (-3.70 eV at HF). In contrast, *trans*-FA dissociates spontaneously first into surface formate in the unidentate configuration (**O-down**), which one oxygen atom of formate interacts with one surface Zn atom and the other oxygen atom interacts with the hydrogen atom of the surface OH group, and the energy barrier for the dissociative adsorption of *trans*-FA to form the bridging bidentate formate and surface OH group is 0.64 eV at HF.

On the basis of the results of Nakatusji *et al.*,⁹² Yoshimoto *et al.*,⁹³ further computed FA decomposition on (10 $\bar{1}$ 0) using a Zn₄O₄ cluster embedded in an electrostatic field to simulate the Madelung potential at the HF and MP2 levels of theory. Starting from the most stable adsorbed formate on the surface (**O/O-down**), the first step of the minimum energy path is the

C-H bond dissociation to form CO₂ and surface Zn-H and the computed barrier is 2.30 eV at HF, and the second step is the molecular adsorption of a second *cis*-FA molecule, where the oxygen atom of the O=C group interacts with one surface Zn atom and the oxygen atom of the O-H group interacts with the Zn atom of the formed Zn-H group, directly followed by H₂ formation and surface formate regeneration, and the calculated barrier is rather low (0.29 eV at HF). From FA adsorption to CO₂ and H₂, the rate-determining step is the C-H bond dissociation from the adsorbed formate.

Apart from the above mentioned cluster model for FA adsorption and decomposition, Persson and Ojamäe⁹⁴ computed FA adsorption by using periodic HF method. In their calculations, they did not include the adsorption-induced surface relaxation effect. For *trans*-FA, they found dissociative adsorption in two unidentate configurations; one is the same as reported by Nakatusji *et al.*,⁹² where the surface formate interacts with one surface Zn atom and one oxygen atom interacts with the hydrogen atom of the surface OH group direct bonded to the Zn atom and they form a 6-membered ring (or short-bridge form), and the second configuration has the same surface interaction modes but the formate and surface Zn and O form a 8-membered ring (or long bridge form); and the latter one is more stable than the former one by about 0.3 eV. Later on, Persson *et al.*,⁹⁵ refined their surface model by relaxing the first surface layer and confirmed their previous results qualitatively and they also found that surface relaxation can have a significant influence on the equilibrium geometries and adsorption energies. The most stable bridging bidentate adsorption configuration (**O/O-down**) of formate on ZnO was also confirmed by a combined experimental (X-ray powder diffraction, transmission electron microscopy, Fourier transform infrared spectroscopy, X-ray photoelectron spectroscopy, UV-vis, and photoluminescence spectroscopy) and theoretical (a Zn₁₀O₁₀ cluster model at B3LYP/6-31+G(d,p)) studies by Lenz *et al.*⁹⁶

1.3.4 Nickel oxide

Miura *et al.*,⁹⁷ computed formate decomposition on NiO(111) using (NiO)₄ cluster model at the B3LYP level of DFT. Since FA can dissociate easily into surface formate and surface hydroxyl, they focused only on formate decomposition into CO₂ and H. On the NiO(111) surface, formate prefers the chelating bidentate adsorption configuration (**O/O-down**); and this chelating bidentate adsorption configuration can easily go to the corresponding monodentate adsorption configuration (**O-down**) with very low energy barrier (0.26 eV), and the former is more stable than the later latter by 0.22 eV. Rotation of the monodentate formate group results in the monodentate adsorption configuration (**O/H-down**) without essential barrier, where its C-H group pointing to the neighboring surface oxygen atom. The next step is the C-H bond dissociation with the formation of the chemisorbed CO₂ and surface OH; and the corresponding barrier is 0.76 eV, this step is also the rate-determining step. These findings are in agreement with the experimental results.

1.4 Conclusion and outline

We mainly outlined the recent computational investigations into FA adsorption and decomposition on some metal (Pt, Pd, Ni, Cu, Rh and Au) and metal oxide (TiO₂, MgO, ZnO and NiO) surfaces, despite of the fact that there are plentiful literatures data for the adsorption of many individual surface intermediates which are related to FA adsorption and decomposition; and homogeneous catalytic decomposition of FA using defined molecular complexes are also not discussed here. The goal is the understanding into the reaction mechanisms of selective dehydrogenation and dehydration.

On metal surfaces, molecular FA adsorption configuration has been found, and such configuration can go to the adsorbed surface formate and H easily via low barrier. The most important surface intermediate is formate, which has a bridging bidentate adsorption configuration with its two oxygen atoms interacting with two surface metal atoms. The subsequent C-H bond dissociation in formate results in CO₂ formation. Apart from the well discussed formate route, alternative routes like FA direct dissociation into CO+H₂O and carboxylic (COOH) route have been studied. Despite of these interesting and plentiful results, it is still controversial about the favourable reaction mechanisms for FA catalytic dissociation, and this is because that the computed results depend on many factors, e.g.; model size, coverage, solvation, mono- and bimolecular systems, interaction of adsorbed species, and finally computational methodologies.

FA electro-catalytic oxidation might have three different routes, the formate route, the direct route and the indirect route under the consideration of water solvent molecules and the applied potentials. Apart from the formate route, both the direct and indirect routes might be accessible depending on the model systems, and it is also found the pre-adsorbed formate might act as a catalyst for C-H bond activation and CO₂ formation. The co-adsorbed CO and OH might also affect this reaction.

On metal oxide surfaces, FA adsorbs mostly dissociatively into surface formate and surface OH group; and surface formate prefers the bridging bidentate adsorption configuration. In addition, surface defects or surface oxygen vacancies also play an important role in the subsequent dissociation steps. Since the first step of FA decomposition is more or less very easy, the surface formate represents the most important intermediate for the subsequent reactions, and the selective decomposition of formate either via the dynamic bending structure or the transfer from the bridging bidentate to the monodentate structures remains the intriguing and challenging task.

Despite of the rapid development in information technology and quantum chemical methodology as well as their wide applications, all these reported calculations used very limited and over idealized or simplified models, which are far away from the real systems; and many controversial results have been found by using different model and methods. Since many relevant structural parameters, especially those of the transition states, are not available in many

studies, it is not possible or easy to understand the origins of the quite different or controversial results and to identify the best catalysts for H₂ generation from FA decomposition.

One of the most important effects in heterogeneous catalysis, the quantum size effect of the nanocatalysts, has not been studied adequately. Moreover, all these reported calculations are carried out under idealized conditions; and the reaction parameters like temperature, pressure have not been considered. Recent computational studies show that it is necessary to include the contribution of temperature and pressure from *ab initio* atomistic thermodynamics.^{98,99} This is because that all the reported studies used the most stable surfaces, which have the lowest adsorption energies or the smallest desorption energies and at the working temperature and pressure, desorption instead of adsorption might take place.^{100,101}

In future work, we need not only the development in nanotechnology and analytic methods for providing more detailed information of surface properties and sophisticated computational methodologies but also more reasonable (stepped, kinked or defect) model systems for a better understanding into the catalytic mechanisms under the consideration of the reaction conditions (temperature and pressure as well as solvent)

1.5 References

- (1) Loges, B.; Boddien, A.; Gärtner, F.; Junge, H.; Beller, M. *Top. Catal.* **2010**, *53*, 902–914.
- (2) Mailhe, A.; Sabatier, P. *Compt. Rend.* **1912**, *152*, 1212–5.
- (3) Mars, P.; Scholten, J. J. F.; Zwietering, P. *Adv. Catal.* **1963**, *14*, 35–113.
- (4) Trillo, J. M.; Munuera, G.; Criado, J. M. *Catal. Rev.* **1972**, *7*, 51–86.
- (5) Madix, R. J. *Adv. Catal.* **1980**, *29*, 1–53.
- (6) Columbia, M. R.; Thiel, P. A. *J. Elect. Chem.* **1994**, *369*, 1–14.
- (7) Tedsree, K.; Li, T.; Jones, S.; Chan, C. W. A.; Yu, K. M. K.; Bagot, P. A. J.; Marquis, E. A.; Smith, G. D. W.; Tsang, S. C. E. *Nature Nanotech.* **2011**, *6*, 302–307.
- (8) Fang, P. P.; Duan, S.; Lin, X. D.; Anema, J. R.; Li, J. F.; Buriez, O.; Ding, Y.; Fan, F. R.; Wu, D. Y.; Ren, B.; Wang, Z. L.; Amatore, C.; Tian, Z. Q.; *Chem. Sci.* **2011**, *2*, 531–539.
- (9) Bi, Q. Y.; Du, X. L.; Liu, Y. M.; Cao, Y.; He, H. Y.; Fan, K. N.; *J. Am. Chem. Soc.* **2012**, *134*, 8926–8933.
- (10) Flaherty, D. W.; Berglund, S. P.; Mullins, C. B. *J. Catal.* **2010**, *269*, 33–43.
- (11) Koós, Á.; Solymosi, F.; *Catal. Lett.* **2010**, *138*, 23–27.
- (12) Gazsi, A.; Bánsági, T.; Solymosi, F. *J. Phys. Chem. C* **2011**, *115*, 15459–15466.
- (13) Kang, Y.; Qi, L.; Li, M.; Diaz, R. E.; Su, D.; Adzic, R. R.; Stach, E.; Li, J.; Murray, C. B. *ACS Nano* **2012**, *6*, 2818–2825.
- (14) Cuesta, A.; Cabello, G.; Osawa, M.; Gutiérrez, C. *ACS Catal.* **2012**, *2*, 728–738.
- (15) Behrens, M.; Studt, F.; Kasatkin, I.; Kuhl, S.; Havecker, M.; Abild-Pedersen, F.; Zander, S.; Girgsdies, F.; Kurr, P.; Knief, B. L.; Tovar, M.; Fischer, R. W.; Nørskov, J. K.; Schlogl, R. *science* **2012**, *336*, 893–897.

-
- (16) Zhang, S.; Metin, Ö.; Su, D.; Sun, S. *Angew. Chem. Int. Ed.* **2013**, *52*, 3681–3684.
- (17) Wang, Z. L.; Yan, J. M.; Ping, Y.; Wang, H. L.; Zheng, W. T.; Jiang, Q. *Angew. Chem. Int. Ed.* **2013**, *52*, 4406–4409.
- (18) Johnson, T. C.; Morris, D. J.; Wills, M. *Chem. Soc. Rev.* **2010**, *39*, 81–88.
- (19) Loges, B.; Boddien, A.; Junge, H.; Beller, M. *Angew. Chem. Int. Ed.* **2008**, *47*, 3962–3965.
- (20) Fellay, C.; Dyson, P. J.; Laurenczy, G. *Angew. Chem. Int. Ed.* **2008**, *47*, 3966–3968.
- (21) Fukuzumi, S. *Eur. J. Inorg. Chem.* **2008**, 1351–1362.
- (22) Boddien, A.; Loges, B.; Gärtner, F.; Torborg, C.; Fumino, K.; Junge, H.; Ludwig, R.; Beller, M. *J. Am. Chem. Soc.* **2010**, *132*, 8924–8934.
- (23) Boddien, A.; Mellmann, D.; Gärtner, F.; Jackstell, R.; Junge, H.; Dyson, P. J.; Laurenczy, G.; Ludwig, R.; Beller, M. *Science* **2011**, *333*, 1733–1736.
- (24) Hammer, B.; Nørskov, J. K. *Adv. Catal.* **2000**, *45*, 71–129.
- (25) Inderwildi, O. R.; Jenkins, S. J.; *Chem. Soc. Rev.* **2008**, *37*, 2274–2309.
- (26) Torrent, M.; Solà, M.; Frenking, G. *Chem. Rev.* **2000**, *100*, 439–493.
- (27) Niu, S.; Hall, M. B. *Chem. Rev.* **2000**, *100*, 353–406.
- (28) López, N.; Almora-Barrios, N.; Carchini, G.; Błoński, P.; Bellarosa, L.; Garcí-Muelas, R.; Novell-Leruth, G.; García-Motac, M. *Catal. Sci. Technol.* **2012**, *2*, 2405–2417.
- (29) Wiest, O.; Wu, Y. (Eds), *Computational Organometallic Chemistry*, Springer **2012**.
- (30) Santen, R. A. V.; Neurock, M. (Eds), *Molecular Heterogeneous Catalysis: A Conceptual, Computational Approach*, Wiley-Vch, **2006**.
- (31) Leitner, W.; Dinjus, E.; Gaßner, F. *J. Organomet. Chem.* **1994**, *475*, 257–266.
- (32) Maseras, F.; Lledós, A. (Eds), *Computational Modeling of Homogeneous Catalysis*, **2002** Kluwer Academic Publishers, p79–105.
- (33) Ohnishi, Y. Y.; Nakao, Y.; Sato, H.; Sakaki, S. *Organometallics* **2006**, *25*, 3352–3363.
- (34) Ohnishi, Y. Y.; Matsunaga, T.; Nakao, Y.; Sato, H.; Sakaki, S. *J. Am. Chem. Soc.* **2005**, *127*, 4021–4032.
- (35) Musashi, Y.; Sakaki, S. *J. Am. Chem. Soc.* **2000**, *122*, 3867–3877.
- (36) Musashi, Y.; Sakaki, S. *J. Am. Chem. Soc.* **2002**, *124*, 7588–7603.
- (37) Chen, Y. X.; Heinen, M.; Jusys, Z.; Behm, R. J. *Angew. Chem. Int. Ed.* **2006**, *45*, 981–985.
- (38) Bakó, I.; Pálinkás, G. *Surf. Sci.* **2006**, *600*, 3809–3814.
- (39) Saliccioli, M.; Edie, S. M.; Vlachos, D. G. *J. Phys. Chem. C* **2012**, *116*, 1873–1886.
- (40) Hartnig, C.; Grimminger, J.; Spohr, E. *J. Elect. Chem.* **2007**, *607*, 133–139.
- (41) Neurock, M.; Janik, M.; Wieckowski, A. *Faraday, Discuss* **2008**, *140*, 363–378.
- (42) Zhong, W.; Zhang, D. *Catal. Commun.* **2012**, *29*, 82–86.
- (43) Zhong, W.; Wang, R.; Zhang, D.; Liu, C. *J. Phys. Chem. C* **2012**, *116*, 24143–24150.
- (44) Wang, H. F.; Liu, Z. P. *J. Phys. Chem. C* **2009**, *113*, 17502–17508.

- (45) Peng, B.; Wang, H. F.; Liu, Z. P.; Cai, W. B.; *J. Phys. Chem. C* **2010**, *114*, 3102–3107.
- (46) Gao, W.; Keith, J. A.; Anton, J.; Jacob, T. *Dalton Trans.* **2010**, *39*, 8450–8456.
- (47) Gao, W.; Keith, J. A.; Anton, J.; Jacob, T. *J. Am. Chem. Soc.* **2010**, *132*, 18377–18385.
- (48) Gao, W.; Mueller, J. E.; Jiang, Q.; Jacob, T. *Angew. Chem. Int. Ed.* **2012**, *51*, 9448–9452.
- (49) Segall, M. D.; Lindan, P. L. D.; Probert, M. J.; Pickard, C. J.; Hasnip, P. J.; Clark, S. J.; Payne, M. C. *J. Phys.: Cond. Matt.* **2002**, *14*, 2717–2744.
- (50) Kresse, G.; Hafner, J. *Phys. Rev. B* **1993**, *47*, 558–561.
- (51) Cao, D.B.; Li, Y.W.; Wang, J.; Jiao, H. *J. Phys. Chem. C* **2008**, *112*, 14884–14890.
- (52) Barteau, M. A. *Catal. Lett.* **1991**, *8*, 175–183.
- (53) Larsen, R.; Ha, S.; Zakzeski, J.; Masel, R. I. *J. Power Sources* **2006**, *157*, 78–84.
- (54) Zhou, S.; Qian, C.; Chen, X. *Catal. Lett.* **2011**, *141*, 726–734.
- (55) Luo, Q.; Feng, G.; Beller, M.; Jiao, H. *J. Phys. Chem. C* **2012**, *116*, 4149–4156.
- (56) Zheng, T.; Stacchiola, D.; Saldin, D. K.; James, J.; Sholl, D. S.; Tysoe, W. T. *Surf. Sci.* **2005**, *574*, 166–174.
- (57) Hu, C.; Ting, S. W.; Chan, K. Y.; Huang, W. *Int. J. Hydrogen Energy* **2012**, *37*, 15956–15965.
- (58) Zhang, R.; Liu, H.; Wang, B.; Ling, L.; *J. Phys. Chem. C* **2012**, *116*, 22266–22280.
- (59) Yuan, D.W.; Liu, Z. R. *J. Power Sources*, **2013**, *224*, 241–249.
- (60) Li, S. J.; Zhou, X.; Tian, W. Q.; *J. Phys. Chem. A*, **2012**, *116*, 11745–11752.
- (61) Peng, G.; Sibener, S. J.; Schatz, G. C.; Ceyer, S. T.; Mavrikakis, M. *J. Phys. Chem. C* **2012**, *116*, 3001–3006.
- (62) Peng, G.; Sibener, S. J.; Schatz, G. C.; Mavrikakis, M. *Surf. Sci.* **2012**, *606*, 1050–1055.
- (63) Wang, S. G.; Cao, D. B.; Li, Y. W.; Wan, J.; Jiao, H. *J. Phys. Chem. B* **2005**, *109*, 18956–18963.
- (64) Vesselli, E.; De Rogatis, L.; Ding, X.; Baraldi, A.; Savio, L.; Vattuone, L.; Rocca, M.; Fornasiero, P.; Peressi, M.; Baldereschi, A.; Rosei, R.; Comelli, G. *J. Am. Chem. Soc.* **2008**, *130*, 11417–11422.
- (65) Vesselli, E.; Rizzi, M.; De Rogatis, L.; Ding, X.; Baraldi, A.; Comelli, G.; Savio, L.; Vattuone, L.; Rocca, M.; Fornasiero, P.; Baldereschi, A.; Peressi, M. *J. Phys. Chem. Lett.* **2010**, *1*, 402–406.
- (66) Tao, S. X.; Wang, G. C.; Bu, X. H. *J. Phys. Chem. B* **2006**, *110*, 26045–26054.
- (67) Wang, G. C.; Morikawa, Y.; Matsumoto, T.; Nakamura, J. *J. Phys. Chem. B* **2006**, *110*, 9–11.
- (68) Mei, D.; Xu, L.; Henkelman, G. *J. Catal.* **2008**, *258*, 44–51.
- (69) Beltramo, G. L.; Shubina, T. E.; Koper, M. T. M. *ChemPhysChem* **2005**, *6*, 2597–2606.
- (70) Xu, J.; Yuan, D.; Yang, F.; Mei, D.; Zhang, Z.; Chen, Y. X.; *Phys. Chem. Chem. Phys.* **2013**, *15*, 4367–4376.
- (71) Pang, C. L.; Lindsay, R.; Thornton, G.; *Chem. Soc. Rev.* **2008**, *37*, 2328–2353.

- (72) Ahdjoudj, J.; Minot, C. *Catal. Lett.* **1997**, *46*, 83–91.
- (73) Bates, S. P.; Kresse, G.; Gillan, M. J. *Surf. Sci.* **1998**, *409*, 336–349.
- (74) Käckell, P.; Terakura, K. *Appl. Surf. Sci.* **2000**, *166*, 370–375.
- (75) Käckell, P.; Terakura, K. *Surf. Sci.* **2000**, *461*, 191–198.
- (76) Wang, L. Q.; Ferris, K. F.; Shultz, A. N.; Baer, D. R.; Engelhard, M. H. *Surf. Sci.* **1997**, *380*, 352–364.
- (77) Vittadini, A.; Selloni, A.; Rotzinger, F. P.; Grätzel, M. *J. Phys. Chem. B* **2000**, *104*, 1300–1306.
- (78) Gong, X. Q.; Selloni, A.; Batzill, M.; Diebold, U. *Nat. Mater.*, **2006**, *5*, 665–670.
- (79) Miller, K. L.; Falconer, J. L.; Medlin, J. W. *J. Catal.* **2011**, *278*, 321–328.
- (80) Miller, K. L.; Musgrave, C. B.; Falconer, J. L.; Medlin, J. W. *J. Phys. Chem. C* **2011**, *115*, 2738–2749.
- (81) Gong, X. Q.; Selloni, A. *J. Catal.* **2007**, *249*, 134–139.
- (82) Gong, X. Q.; Selloni, A.; Vittadini, A. *J. Phys. Chem. B* **2006**, *110*, 2804–2811.
- (83) Li, W. K.; Gong, X. Q.; Lu, G.; Selloni, A. *J. Phys. Chem. C* **2008**, *112*, 6594–6596.
- (84) Nunzi, F.; De Angelis, F. *J. Phys. Chem. C* **2011**, *115*, 2179–2186.
- (85) Morikawa, Y.; Takahashi, I.; Aizawa, M.; Namai, Y.; Sasaki, T.; Iwasawa, Y. *J. Phys. Chem. B* **2004**, *108*, 14446–14451.
- (86) Aizawa, M.; Morikawa, Y.; Namai, Y.; Morikawa, H.; Iwasawa, Y. *J. Phys. Chem. B* **2005**, *109*, 18831–18838.
- (87) Uemura, Y.; Taniike, T.; Tada, M.; Morikawa, Y.; Iwasawa, Y. *J. Phys. Chem. C* **2007**, *111*, 16379–16386.
- (88) Avdeev, V. I.; Parmon, V. N. *J. Phys. Chem. C* **2011**, *115*, 21755–21762.
- (89) Nakatsuji, H.; Yoshimoto, M.; Hada, M.; Domen, K.; Hirose, C. *Surf. Sci.* **1995**, *336*, 232–244.
- (90) Szymański, M. A.; Gillan, M. J. *Surf. Sci.* **1996**, *367*, 135–148.
- (91) Lintuluoto, M.; Nakatsuji, H.; Hada, M.; Kanai, H. *Surf. Sci.* **1999**, *429*, 133–142.
- (92) Nakatsuji, H.; Yoshimoto, M.; Umemura, Y.; Takagi, S.; Hada, M. *J. Phys. Chem.* **1996**, *100*, 694–700.
- (93) Yoshimoto, M.; Takagi, S.; Umemura, Y.; Hada, M.; Nakatsuji, H. *J. Catal.* **1998**, *173*, 53–63.
- (94) Persson, P.; Ojamäe, L.; *Chem. Phys. Lett.* **2000**, *321*, 302–308.
- (95) Persson, P.; Lunell, S.; Ojamäe, L.; *Int. J. Quantum Chem.* **2002**, *89*, 172–180.
- (96) Lenz, A.; Selegård, L.; Söderlind, F.; Larsson, A.; Holtz, P. O.; Uvdal, K.; Ojamäe, L.; Käll, P. O. *J. Phys. Chem. C* **2009**, *113*, 17332–17341.
- (97) Miura, T.; Kobayashi, H.; Domen, K.; *J. Phys. Chem. B* **2001**, *105*, 10001–10006.
- (98) Reuter, K.; Scheffler, M. *Phys. Rev. B* **2001**, *65*, 035406–11.
- (99) Reuter, K.; Scheffler, M. *Phys. Rev. B* **2003**, *68*, 045407–11.

(100) Wang, T.; Liu, X.; Wang, S.; Huo, H. C.; Li, Y. W.; Wang, J.; Jiao, H. *J. Phys. Chem. C* **2011**, *115*, 22360–22368.

(101) Wang, T.; Wang, S.; Li, Y. W.; Wang, J.; Jiao, H. *J. Phys. Chem. C* **2012**, *116*, 6340–6348.

2 Formic Acid Dehydrogenation on Ni(111) and Pd(111) and Comparison with Pt(111)

2.1 Introduction

One of the biggest challenges of our human society in the 21st century is the rising global energy demand and the depleted fossil fuel reserves, and a hydrogen economy has been considered as one of the energy resources to solve this problem.¹ Nowadays, hydrogen is mainly produced from fossil resources by means of steam reforming and coal gasification, which require high-temperature and consume extra energy. Although molecular hydrogen has very high energy density on its mass basis, but very low energy density by volume at ambient condition. For being used as transport fuel, hydrogen must be pressurized or liquefied to provide sufficient driving range for compact, light, safe and affordable containment. Since hydrogen is an energy carrier instead of a primary energy, its generation or production from suitable materials under mild condition, storage and conversion into electrical energy are very challenging.

Compared with other hydrogen resources, formic acid is non-toxic, easy to be handled and stored, and provides a viable method for safety hydrogen carrier.² There are previous experimental studies on the adsorption and dehydrogenation of formic acid on transition metal surface.³ Recently, Beller and co-workers generated hydrogen successfully from formic acid amine adduct at high rate and room temperature for direct usage in fuel cell.⁴ Laurenczy⁵ and Fukuzumi⁶ also showed that formic acid can be used as an efficient hydrogen storage material. Jessop et al. showed that CO₂ can be hydrogenated to formic acid under supercritical CO₂.⁷ Solymosi *et al.*, reported the decomposition and reforming of formic acid on supported Au catalysts to produce CO free hydrogen,⁸ and they also reported that Mo₂C prepared by the reaction of Mo₃O with a multiwalled carbon nanotube and carbon Norit is an excellent and stable catalyst for hydrogen production from formic acid virtually free of CO.⁹ Promising results were also obtained from the decomposition of formic acid on various supported metal catalysts.¹⁰ Very recently a new process for hydrogenating CO₂ to formic acid using homogeneous ruthenium catalysts has been reported by Schaub and Paciello.¹¹

Theoretically Sakaki *et al.*, investigated CO₂ hydrogenation to formic acid using ruthenium¹² and rhodium¹³ catalysts under homogeneous conditions. Under heterogeneous conditions, the reaction mechanism of electrocatalytic oxidation of formic acid over Pt(111) in the presence of water has been elucidated.^{14,15} Jacob *et al.*,¹⁶ computed the mechanisms of formic acid oxidation on the Pt(111) surface under electrochemical condition with water-covered compared with the gas-phase reactions. On the basis of ¹³C NMR measurement and DFT calculation Tsang *et al.*,¹⁷ reported the size effect of various metal colloid catalysts on the decomposition and electro-oxidation of formic acid, and found different adsorption configurations (bridging, monodentate and multimodentate) of formate in

equilibrium upon the change of the catalyst sizes. Recently Zhou *et al.*, studied formic acid dehydrogenation on Pd(111) surface.¹⁸ Formic acid dehydrogenation on other metal surfaces (Pt(100) and Pd(100)¹⁹) and metal oxide surfaces (MgO(001),²⁰ CeO₂,²¹ TiO₂(110),²² ZnO(10 $\bar{1}$ 0),²³ CuO²⁴ and α -Fe₂O₃,²⁵ as well as pure and MgO doped γ -Al₂O₃²⁶) also were reported.

As an excellent reforming catalyst, Ni has been extensively used for hydrogen generation from steam reforming ($\text{CH}_4 + \text{H}_2\text{O} = \text{CO} + 3\text{H}_2$), partial oxidation ($\text{CH}_4 + 1/2\text{O}_2 = \text{CO} + 2\text{H}_2$) and dry reforming ($\text{CH}_4 + \text{CO}_2 = 2\text{CO} + 2\text{H}_2$).²⁷ Using Ni(111) as a model catalyst, the dry reforming mechanism was investigated by Zhu *et al.*,²⁸ and Wang *et al.*²⁹ In addition, CH₄ dehydrogenation³⁰ and CO₂ chemisorption³¹ on Ni(111) also have been computed. The kinetic mechanism of methanol decomposition into CO and H atom ($\text{CH}_3\text{OH} = \text{CO} + 4\text{H}$),³² and the conversion process of formaldehyde and methanol from CO and H₂³³ were reported. The CH_x stability and reactivity of on the Ni(111) surface was studied by Nørskov *et al.*³⁴ HCN hydrogenation to methylamine ($\text{HCN} + 2\text{H}_2 = \text{CH}_3\text{NH}_2$) was studied by Olive *et al.*³⁵ As a fundamental process for the refining industry benzene hydrogenation ($\text{C}_6\text{H}_6 + 3\text{H}_2 = \text{C}_6\text{H}_{12}$) was explored by Mittendorfer and Hafner.³⁶

To the best of our knowledge, formic acid dehydrogenation on Ni surface has not been reported. Since nickel is much cheaper than palladium and platinum, we investigated the mechanism of formic acid dehydrogenation on Ni(111) by using density functional theory methods and compared our data with the available experimental and theoretical results. Detailed comparisons for formic adsorption and dehydrogenation have been made among Ni(111), Pd(111) and Pt(111), and high similarities among these metals have been found.

2.2 Computational details

All calculations were performed using plane-wave periodic density functional method as implemented in the Vienna ab initio simulation package (VASP).³⁷ The exchange and correlation energies were calculated using the Perdew, Burke and Ernzerhof (PBE)³⁸ functional within the generalized gradient approximation (GGA). The electron-ion interaction was described by the projector augmented wave (PAW) method,³⁹ and the Kohn-Sham one-electron states were expanded in a plane wave basis set up to 400 eV. Electron smearing of $\sigma = 0.1$ eV⁴⁰ was used following the Methfessel-Paxton scheme. Spin polarization was included for the correct description of magnetic properties.

For optimizing the crystal lattices all atoms were fully relaxed with the forces converged to be less than 0.02 eV/Å and the total energy converged to be less than 10⁻⁴ eV. Brillouin zone sampling was employed using a Monkhorst-Pack grid.⁴¹ The calculated crystal lattice and magnetic moment is 3.517 Å and 6.1 μ_B , respectively, and they are in well agreement with the experimental value of 3.52 Å⁴² and 6.040 μ_B ,⁴³ respectively. For the Ni(111) surface, the first Brillouin zone was sampled with 3×3×1 k-point grid. For calculating gas phase molecules a 7.46×7.46×19.06 Å lattice was used.

Ni(111) was modelled using a three-layer slab with a 15 Å vacuum zone in the z direction to separate the slabs, a $p(3 \times 3)$ super cell with nine atoms at each layer was used; and this corresponds to a 1/9 monolayer (ML) coverage. This model was tested and benchmarked previously by Wang *et al.*^{29-30,31} In our calculation, we have fixed the bottom layer to their bulky position, while relaxed the top two layers along with the adsorbates, and the calculated adsorption energy of formic acid is -0.36 eV. We also tested a four-layer model with the top one layer, top two layers and top three layers relaxed, and the calculated adsorption energy of formic acid is -0.39, -0.39 and -0.41 eV, respectively. It shows that our three-layer model with top two layers relaxed is reasonable. Figure 2.1 shows the top view of Ni(111) and the adsorption modes, i.e.; the face-centered cubic (fcc) site; the hexagonal-close packed (hcp) site, the top site and the bridge site; in which the blue and white atoms represent the first and the second layers of Ni(111), respectively. Due to the structural and energetic similarities for the adsorption at the fcc and hcp sites, we discussed mainly the results for the adsorption at the fcc site, while those at the hcp site are given in Appendix Figures A1-A5 for comparison if not mentioned otherwise. In addition, we tested a 4-layer slab with $5 \times 5 \times 1$ k-point grid (top two layers with adsorbates were relaxed and bottom two layers were fixed to the bulk positions), and the calculated adsorption energy of formic acid is -0.33 eV; and the calculated dissociation barrier is 0.37 eV, these are close to the values (-0.36 vs. 0.41 eV) by using 3-layer model with $3 \times 3 \times 1$ k-point grid.

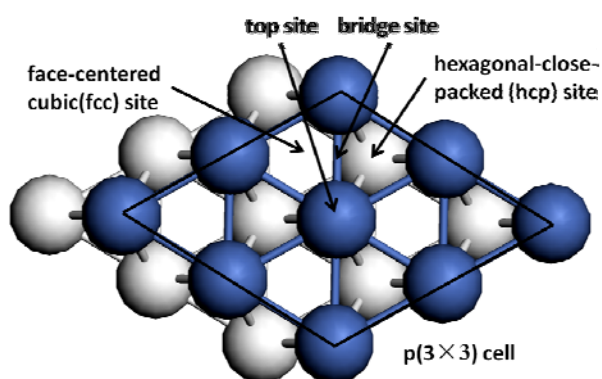


Figure 2.1 Top view of the Ni(111) surface and the adsorption sites (first layer Ni in blue and second layer Ni atom in white)

The nudged elastic band (NEB) method was used to find a minimum energy path (MEP) between an initial and a final state; both are local minima on the potential energy surface.⁴⁴ In this approach, the reaction path is discretized with the discrete configurations or images between minima connected by elastic springs to prevent the images from sliding to the minima in optimization. The vibrational frequencies of the adsorbed species and the transitional states were calculated by diagonalizing the mass-weighted force constant matrix, obtained by numerically differentiation of analytically calculated forces as implemented in

VASP. Since both hydrogen and deuterium atoms have the same electronic structure, and differ only in mass, we used the mass of 1 for hydrogen and 2 for deuterium in the corresponding frequency calculations.

The Hessian matrix was determined based on a finite difference approach with a step size of 0.024 Å for the displacements for individual atoms of the adsorbate along each Cartesian coordinate. The computed vibrational frequencies were used to characterize a minimum state without imaginary frequencies or an authentic transition state with only one imaginary frequency.

The adsorption energy is defined as $E_{\text{ads}} = E_{\text{A/slab}} - [E_{\text{slab}} + E_{\text{A}}]$, where $E_{\text{A/slab}}$ is the total energy of the slab with adsorbate A, E_{slab} is the total energy of the bare slab, and E_{A} is the total energy of free adsorbate A. Thus, the more negative the E_{ads} , the stronger the adsorption. The reaction energy (ΔE_{r}) and barrier (E_{a}) are calculated by $\Delta E_{\text{r}} = E_{\text{FS}} - E_{\text{IS}}$ and $E_{\text{a}} = E_{\text{TS}} - E_{\text{IS}}$, respectively, where E_{IS} , E_{FS} and E_{TS} are the total energies of the initial state (IS), final state (FS) and transition state (TS), respectively. For the dissociative reaction $XY = X + Y$, we defined the lateral interaction between X and Y as $E_{\text{int}} = E_{\text{X+Y/slab}} + E_{\text{slab}} - (E_{\text{X/slab}} + E_{\text{Y/slab}})$, where $E_{\text{X/slab}}$ and $E_{\text{Y/slab}}$ are the total energies of the adsorption of X and Y on the slab, respectively, and $E_{\text{X+Y/slab}}$ is the total energy of the co-adsorbed X+Y on the slab.

2.3 Results and Discussion

2.3.1 Formic acid (HCO₂H/DCO₂H) adsorption

In order to get the optimal formic acid adsorption structures on Ni(111), different starting configurations were considered at 1/9 ML coverage, and only the most stable adsorption configuration **1a** is located.

As shown in [Figure 2.2](#), the adsorbed HCOOH in **1a** stands over the fcc centre and the carbonyl oxygen (C=O) binds to atop site and the hydroxyl group (O-H) points towards asymmetrically to two neighbouring nickel atoms. The Ni-O distance is 2.046 Å; and the Ni-H distances are 2.422 and 2.353 Å. The computed adsorption energy for **1a** is -0.36 eV, indicating an energetically favourable process.

In addition to the optimized structural parameters of adsorbed formic acid, it is also interesting to compare the computed stretching frequencies with the available experimental data. Experimentally deuterated formic acid with deuterium at the carbon atom (DCO₂H) was used and the stretching frequencies were recorded at 90 K.⁴⁵ For direct comparison we have computed the stretching frequencies of adsorbed DCO₂H and HCO₂H on Ni(111). As shown in [Table 2.1](#), the computed C=O (1613 vs. 1600-1700 cm⁻¹), C-D (2240 vs. 2200 cm⁻¹), C-O (1275 vs. 1200-1325 cm⁻¹) and O-H (2850 vs. 2730 cm⁻¹) stretching frequencies for the adsorbed DCO₂H are in well agreement with the experimental values, and these agreements validate our model and method. In addition, the expected isotopic effect has been observed between HCO₂H and DCO₂H. For example, the C=O and C-O stretching frequencies of

DCO₂H have slightly lower wave numbers than those of HCO₂H, and the O-H stretching frequency of DCO₂H has somewhat higher wave numbers than that of HCO₂H. As expected the strongest shift of the stretching frequency is found for C-D compared to C-H. These experiments show that there is no corrosion of nickel surface by formic acid under this condition. In view of acidic corrosion of formic acid, it was reported that no evidence of nickel formate film formation was obtained in the temperature range (225-480°C) in which the nickel surface shows active catalysis using electron microscopy and diffraction techniques. However, experiments at lower temperatures (30-55°C) showed that an anhydrous nickel formate film is produced when nickel is exposed to an atmosphere nearly saturated with formic acid. Under these conditions, multilayer adsorption of formic acid becomes possible. Corrosion of the metal surface may then be similar to the reaction with liquid formic acid.⁴⁶

Table 2.1 Vibrational frequencies (ν , cm⁻¹) of adsorbed formic acid on Ni(111)

	1a ^a	DCO ₂ H ^b
$\nu_{C=O}$	1626 (1613)	(1600-1700)
ν_{C-H} (ν_{C-D})	3034 (2240)	(2200)
ν_{C-OH}	1296 (1275)	(1200-1325)
ν_{O-H}	2829 (2850)	(2730)

a) The vibrational frequencies for DCO₂H are given in parenthesis.

b) The experimental values from Ref. [45]

2.3.2 Formate (HCO₂/DCO₂) adsorption

Formate (HCO₂) is a very common surface intermediate in water-gas shift reaction and methanol oxidation. As shown in Figure 2.2, three stable structures of formate adsorption on Ni(111) are found, e.g.; the bidentate bridging structure **2a** with its two oxygen atoms at atop sites; the 3-fold capping structure **2b** and the bidentate structure **2c** with one oxygen and one hydrogen atom at atop sites. The most stable adsorption structure is **2a** with adsorption energy of -2.83 eV, and **2b** and **2c** are less stable (-2.23 and -1.90 eV, respectively). In **2a**, the Ni-O (1.966 Å) and O-C (1.271 Å) distances are in good agreement with calculated values (1.951 vs. 1.277 Å) by Pang *et al.*⁴⁷ In **2b**, the 3-fold capping oxygen to Ni (Ni-O) has distances of 2.011, 2.036 and 2.094 Å. In **2c**, the Ni-O and Ni-H distances are 1.908 and 1.835 Å, respectively.

For the adsorbed HCO₂ in **2a**, the computed C-H stretching frequency is 2989 cm⁻¹, and the symmetrical and asymmetrical stretching frequencies of the bidentate O-C-O bridge are 1304 and 1510 cm⁻¹, respectively. For the adsorbed DCO₂, the corresponding C-D stretching mode is 2202 cm⁻¹, which is in agreement with the experimental value of 2196 cm⁻¹,⁴⁸ and the symmetrical and asymmetrical modes of the bidentate O-C-O bridge are 1280 and 1509 cm⁻¹, respectively. For **2b**, the stretching modes of C-H, C=O and C-O are 2951, 1717 and 1039

cm^{-1} , respectively, and the C-H bending modes are 1314 and 963 cm^{-1} . For **2c**, the stretching modes of C-H, C=O and C-O are 2047, 1751 and 1115 cm^{-1} , respectively, and the C-H bending modes are 1324 and 859 cm^{-1} . It is to note that such bidentate adsorption configurations (**2a** and **2c**) in equilibrium have been observed experimentally on the nano-sized Pd particles.¹⁷

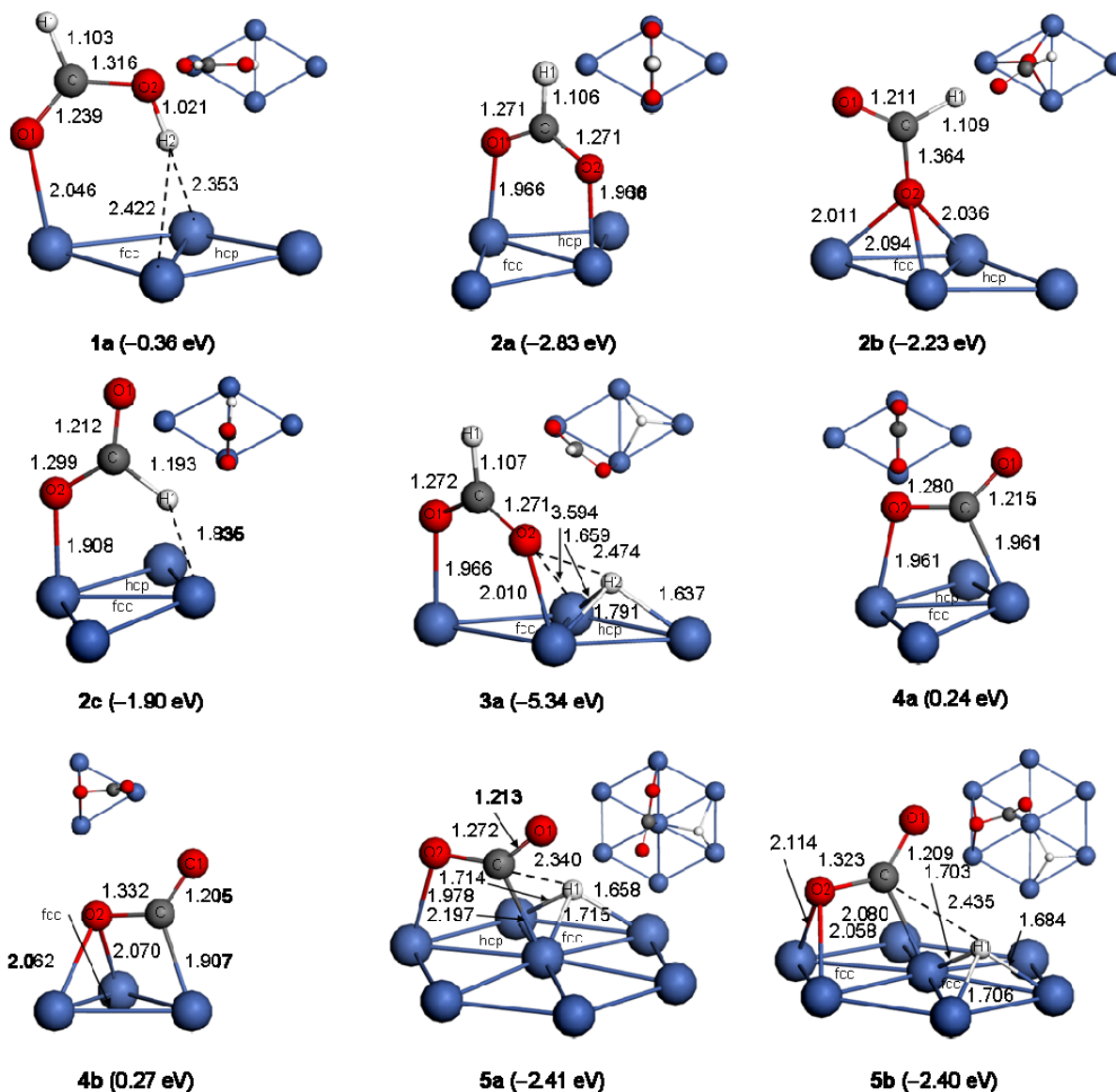


Figure 2.2 The stable structures and adsorption energies of HCO₂H (**1a**), HCO₂ (**2a-2c**), HCO₂ and H co-adsorption (**3a**) CO₂ adsorption (**4a** and **4b**), as well as CO₂ and H co-adsorption (**5a** and **5b**) configuration on Ni(111) (bond distances in Å energies in eV)

2.3.3 HCO₂ and H co-adsorption

For the first dehydrogenation step ($\text{HCO}_2\text{H} \rightarrow \text{HCO}_2 + \text{H}$), we have computed HCO₂ and H co-adsorption. For formate and H co-adsorption, the stable configuration (**3a**) has been found (Figure 2.2); and the computed co-adsorption energy is -5.34 eV. In **3a** the H atom adsorbs at

the 3-fold hcp site and the formate has bidentate coordination over the fcc and hcp centers, and the structural parameters for formate are very close to those in **2a**. The computed lateral interaction energy of **3a** is 0.23 eV. In addition, the computed co-adsorption energy of formate and the subsurface fcc H is -4.96 eV, 0.38 eV less stable than **3a**. The reaction energy of HCO₂H dehydrogenation to HCO₂ and H is exothermic by 0.35 eV.

It is to note that there are plentiful studies about hydrogen adsorption on Ni(111).^{27,42,49-59} It is reported that molecular hydrogen adsorbs dissociatively on Ni(111), and H atom prefers the 3-fold fcc and hcp sites in close energy and surface H adsorption has the largest adsorption energy than those in subsurface.⁵⁹ On Ni(111) Ceyer et al. found that subsurface H can hydrogenate adsorbed methyl to methane, while surface H can not;⁵¹ and subsurface H can hydrogenate adsorbed ethylene to ethane, while surface H does not have such activity under these experimental conditions.⁵² Hu *et al.* calculated the hydrogenation of methyl adsorbed on Ni(111) by surface and subsurface H, and showed that the initial positions of subsurface H relative to the adsorbed methyl play an important role to get a low activation energy.⁵⁵

In our calculation, we considered both surface and subsurface H adsorption in the fcc site at 1/9 ML, and no stable H adsorptions in the hcp subsurface at 1/9 ML have been found. The calculated adsorption of H on the fcc and hcp sites is -2.76 and -2.74 eV, respectively, in agreement with the experimental values -2.73.⁴² The computed adsorption energy of subsurface H in fcc site is -1.98 eV. The surface H-Ni distances are 1.710, 1.709 and 1.706 Å, and the subsurface H-Ni distances are 1.723 Å, which are consistent with the reported values of 1.71 and 1.74 Å by Greeley and Mavrikakis.⁵⁸ The computed H-Ni vibrational frequencies on Ni(111) at 1/9 ML are 1151, 880 and 868 cm⁻¹; and in the subsurface are 886, 882 and 731 cm⁻¹. These values agree well with those at 1/4 ML.⁴⁹

2.3.4 CO₂ and H co-adsorption

For the second dehydrogenation step (HCO₂ → CO₂ + H), we have computed CO₂ and H co-adsorption. Apart from H adsorption, CO₂ adsorption on Ni(111) also was systemically studied.³¹ Herein, only two most stable structures of CO₂ chemisorption (**4a** and **4b**) were taken into account (Figure 2.2). In **4a**, the adsorbed CO₂ bridges the atop sites, while in **4b** the carbon atoms is at the atop site and the oxygen atom bridges two nickel atoms over the fcc center. The computed adsorption energies of **4a** (0.24 eV) and **4b** (0.27 eV) are close to those (0.26 eV at 1/6 ML and 0.31 eV 1/4 ML) found by Wang.³¹ The computed stretching modes of C=O and C-O and the bending mode of O-C-O of **4a** (**4b**) are 1741 (1724), 1100 (963) and 661 (676) cm⁻¹, respectively. The frequencies of isolated CO₂ also were calculated; i.e. the C-O stretching mode and the two bending modes of O=C=O are 2364, 1317, 633 and 631 cm⁻¹, respectively.

On the basis of CO₂ adsorption, two stable configurations (**5a** and **5b**) for CO₂ and H co-adsorption have been found (Figure 2.2); and the computed co-adsorption energy of **5a** and **5b** is -2.41 and -2.40 eV, respectively. In **5a** and **5b**, the co-adsorbed CO₂ configurations

are close to those in **4a** and **4b**, respectively, and the H atom is at the 3-fold fcc and hcp site, respectively. The computed lateral interaction in **5a** and **5b** is 0.11 and 0.09 eV, respectively. In addition the computed co-adsorption energy with H in the subsurface of -1.88 and -1.84 eV, and is 0.53 and 0.56 eV, higher than **5a** and **5b**, respectively.

2.3.5 HCO₂H dehydrogenation

For analyzing the minimum energy path of formic acid dehydrogenation on Ni(111), the transition states for O-H bond breaking have been computed. Experimentally, monomer of formic acid was found to decompose to formate intermediate.⁶⁰ As shown in Figure 2.3, an authentic transition state for the O-H bond breaking **TS(1a/3a)** is located and verified by frequency calculation. In **TS(1a/3a)**, the O-H breaking distance is 1.558 Å, much longer than that of 1.021 Å in **1a**. The computed dehydrogenation barrier is 0.41 eV, and the dehydrogenation energy is -0.35 eV, indicating an exothermic process.

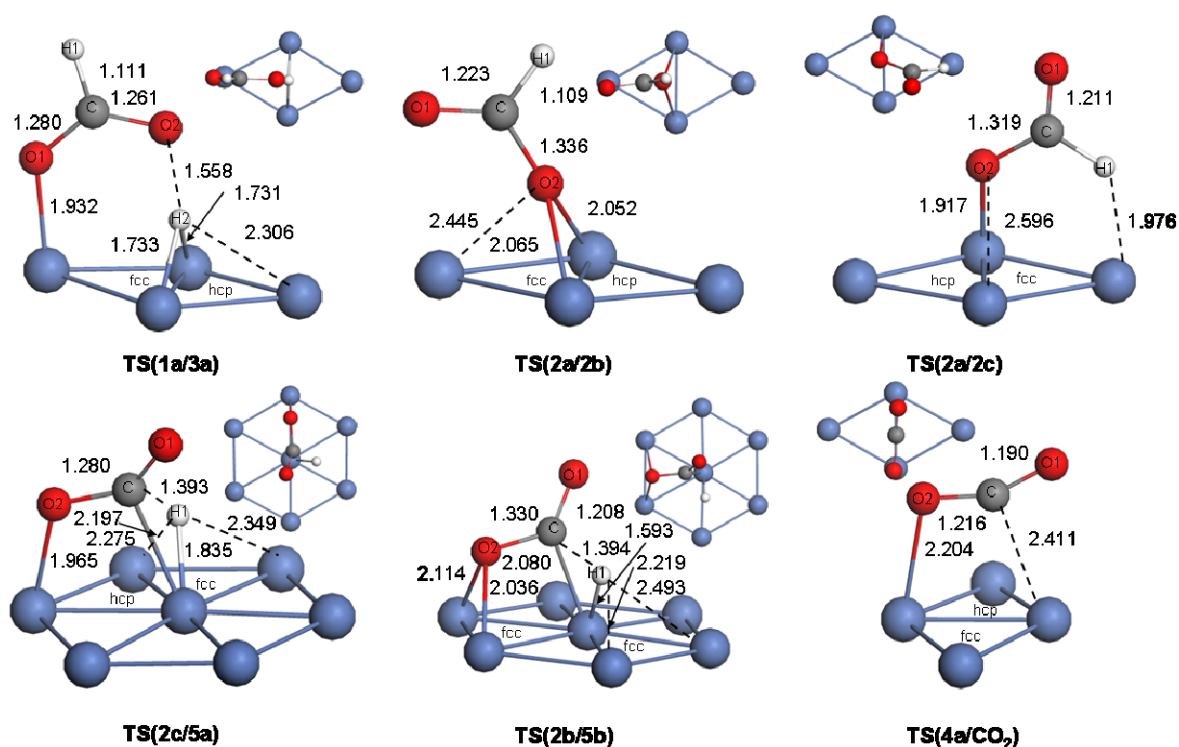


Figure 2.3 Transition state of HCO₂H → HCO₂ + H on Ni(111) the coordination change of HCO₂ adsorption HCO₂ dehydrogenation (bond distances in Å) . CO₂ desorption on Ni(111) (bond distances in Å)

Compared to formic acid dehydrogenation, formate dehydrogenation on Ni(111) is more complicated because of the arrangement of the C-H bond from **2a** via **2b** to **2c** depending on the formate coordination (Figure 2.3). From **2a** to **2b**, the coordination changes from the bidentate mode to the 3-fold capping mode via the corresponding transition state **TS(2a/2b)**

and the barrier is 0.67 eV. The second step is the coordination change from the 3-fold capping mode to the C-O and C-H bidentate mode via the corresponding transition state **TS(2b/2c)** and the barrier is 0.36 eV for **TS(2b/2c)**.

For formate dehydrogenation into CO₂ and H, two authentic transition states, **TS(2c/5a)** and **TS(2b/5b)**, are located and verified by frequency calculations. As shown in Figure 2.3, the breaking C-H distance is 1.393 Å in **TS(2c/5a)** and 1.394 Å in **TS(2b/5b)**; much longer than that (1.193 Å) in **2c**, but shorter than that in **5a** (2.340 Å) and **5b** (2.435 Å). The computed barrier is 0.10 eV for **TS(2c/5a)** and 0.41 eV for **TS(2b/5b)**. The calculated effective barrier is about 1.03 eV.

For CO₂ release we have also computed the transition state **TS(4a/CO₂)**. As shown in Figure 2.3, the Ni-C distances are 2.204 and 2.411 Å, and they are longer than those (1.961 and 1.961 Å) in **4a**. The C-O distances are 1.216 and 1.119 Å. The computed desorption barrier is 0.14 eV.

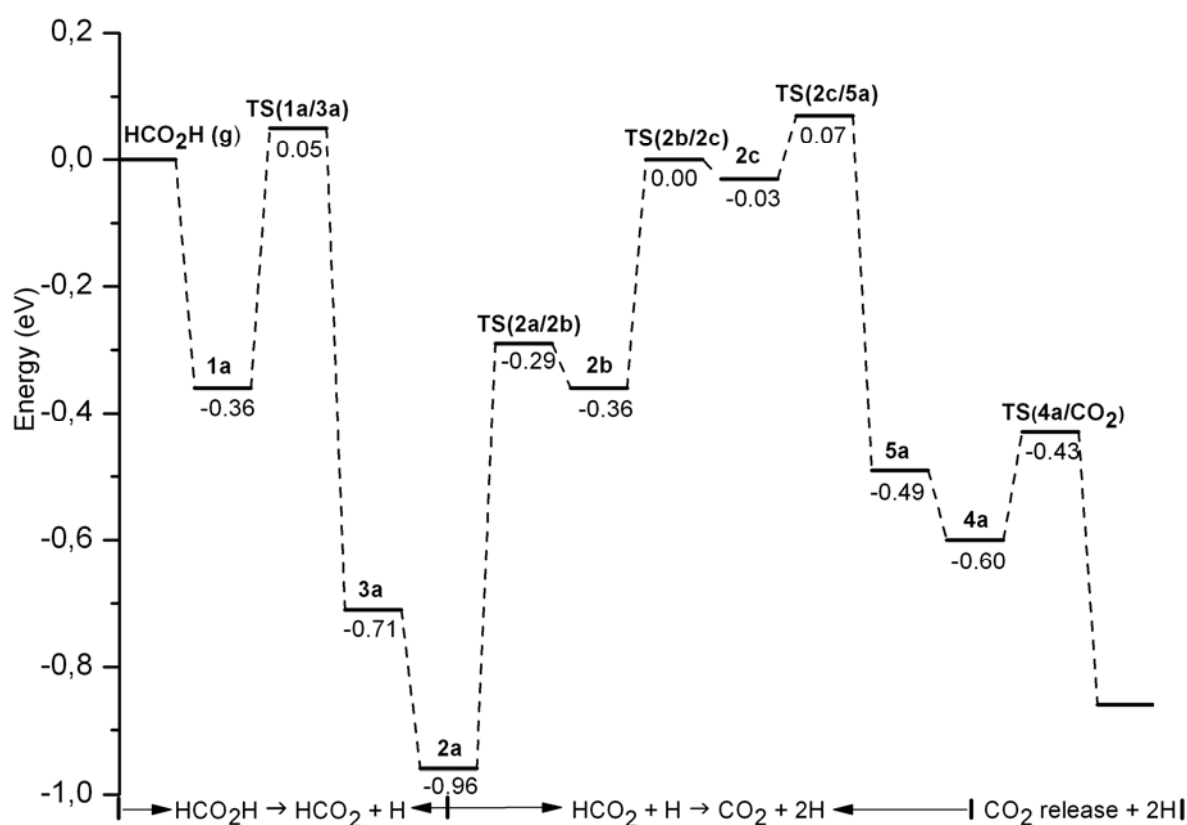


Figure 2.4 Potential energy of formic acid dehydrogenation on Ni (111) (energies in eV)

On the basis of the computed energetic data we have mapped the potential energy surface shown in Figure 2.4. The dehydrogenation of formic acid into formate and atomic hydrogen has barrier of 0.41 eV. The dehydrogenation energy is -0.60 eV for the separated adsorption (or -0.35 eV for co-adsorption) of formate and hydrogen, indicating an exothermic process.

On the potential energy surface, it shows also that the adsorbed formate (**2a**) is the resting state, and the transition state of formate dehydrogenation is the maximum point. Although formate dehydrogenation takes several steps, it is possible to get the effective barrier of about 1.03 eV, and CO₂ desorption needs very low barrier of 0.14 eV. It is to note that the calculated effective barrier for formic acid dehydrogenation of 1.03 eV is close to the reported apparent value of 0.87±0.04 eV in the temperature range between 225-480°C.⁴⁶

2.3.6 Comparison with other surfaces

Since Ni, Pd and Pt are the 10th group elements; it is interesting to compare their geometric and energetic properties of Ni, Pt¹⁶ by Jacob *et al.*, and Pd¹⁸ by Zhou *et al.* for formic acid adsorption and dehydrogenation. Table 2.2 lists the adsorption energy and the energy of the O-H breaking process in formic acid dehydrogenation on metals and metal oxides.

(a) Formic acid adsorption and dissociation: On Ni(111), the O (O=C) atom and the H (O-H) atom point towards two surface atoms, formic acid stands perpendicularly over the surface. The computed adsorption energy is -0.36 eV, and the O-H dissociation has barrier of 0.41 eV and is exothermic by 0.6 eV for the separated adsorption or 0.35 eV for co-adsorption.

Table 2.2 HCO₂H adsorption energy (E_{ads} , eV) and dehydrogenation barrier (E_a , eV) on different surfaces

Surface	E_{ads}	E_a	Reference
Ni(111)	-0.36	0.41	
Pt(111)/1/9 ML	-0.40	0.94	16
Pt(111)/1/4 ML	-0.34	0.88	16
Pd(111)	-0.39	0.58	
Pd(111)	-0.40	0.21	18
ZnO(10 $\bar{1}$ 0)	-3.42		23
MgO(001)	-0.89	0.73	20
TiO ₂ (110)	-1.059		22

On Pd(111), however, Zhou *et al.*, showed that that formic acid lays flat on the Pd (111) surface and bonds the surface with C and O atoms and the computed adsorption energy is -0.40 eV; such flat adsorption structure was also found in our work on Ni(111), but 0.40 eV less stable than the ground state (**1a**, see Appendix Figure A1). The O-H dissociation has barrier of 0.21 eV, and is endothermic by 0.12 eV, and the back reaction barrier is only 0.09 eV.

On Pt(111), the O (O=C) atom bonds the atop site and the H (O-H) atom points towards only one surface atom, and formic acid also stands perpendicularly on the surface, and this stable structure was also reported previously.^{61,62} The computed adsorption energy is -0.34 eV at

1/4 ML and -0.40 eV at 1/9 ML, and the O-H dissociation has barrier of 0.88 eV at 1/4 ML and 0.94 eV at 1/9 ML; and is endothermic by 0.22 eV at 1/4 ML and 0.02 eV at 1/9 ML.

(b) Formate adsorption and dissociation: On Ni(111), **2a** is the most stable adsorption configuration with adsorption energy of -2.83 eV. On Pt(111), the more stable adsorption configuration is close to **2a**, and the adsorption energy is -2.50 eV at 1/4 ML and -2.32 eV at 1/9 ML. For both Ni(111) and Pt(111), formate dehydrogenation needs several steps and the effective dehydrogenation barrier is about 1.03 eV on Ni(111), and 1.16 eV at 1/4 ML and 1.56 eV at 1/9 ML on Pt(111). These indicate the similarity of Ni(111) and Pt(111) in formic acid dehydrogenation.

On Pd(111), Zhou *et al.* also found our **2a**-like, **2b**-like and **2c**-like structures for formate adsorption, and they also found one bridge intermediate with an O atom to two surface Pd atoms (1bridge structure), and the computed adsorption energies are -0.60 , -0.67 , -0.39 and -0.54 eV, much lower than those on Ni(111) and Pt(111). Since the different adsorption states of formic acid on those metals, HCO_2 dehydrogenation was suggested to proceed via **2c**-like to 1bridge structure; and needs to overcome the barriers of 0.01 and 0.17 eV.

The much lower energy barrier of formate dehydrogenation on Pd(111) and the much smaller energy difference between the **2a**- and **2b**-like structures are remarkable compared with those on Ni(111) and Pt(111). To clarify these differences, we performed formic acid and formate adsorption and dehydrogenation on Pd(111) with spin polarization by using the same slab model as used by Zhou *et al.*. In our calculations, the most stable adsorption configuration of formic acid on Pd(111) as energy minimum (**1A**, Appendix Figure A6) is close to **1a** on Ni(111) and **1a**-like on Pt(111), and the computed adsorption energy of -0.39 eV, as expected, is also close to that (-0.36 eV) on Ni(111) and those (-0.34 eV at 1/4 ML and -0.40 eV at 1/9 ML) on Pt(111). In contrast, the flat adsorption configuration for formic acid on Pd(111) reported by Zhou *et al.* could not be located. In addition, our calculated O-H dissociation barrier and dehydrogenation energy of formic acid on Pd(111) are 0.58 and -0.17 eV for separated adsorption (0.09 eV for co-adsorption), respectively, and they are in contrast to the reported results (0.21 vs. 0.12 eV).

For formate adsorption on Pd(111), **2a**- , **2b**- and **2c**-like structures (**2A**, **2B** and **2C**; Appendix Figure A7) are located as energy minimums, and the corresponding adsorption energy is -2.37 , -1.67 and -1.66 eV, respectively, and the energy difference between **2A** and **2B** is 0.70 eV. Our calculated adsorption energies of formate on Pd(111) and their differences are much larger than those given by Zhou *et al.* In addition, our recalculated effective barrier of formate dehydrogenation on Pd(111) is 0.76 eV, which also is much higher than that given by Zhou *et al.*. On the basis of their similarities in the adsorption and dehydrogenation of formic acid and formate on Ni(111), Pd(111) and Pt(111), we believe that our calculated results for Pd(111) are more confidential and reliable than those reported by Zhou *et al.*.

Detailed information of HCO_2 and H co-adsorption and the transition state of formic acid

dissociation into HCO_2 and H as well as the transition state of HCO_2 dissociation into CO_2 and H on Pd(111) are shown in [Appendix Figures A8-A10](#); and [Appendix Table A1](#) shows the adsorption energies (E_{ads} , eV) for all stationary points involved in HCO_2H dissociation into CO_2 and H on Ni(111) and Pd(111).

At 1/9 ML coverage, the adsorption energy of formic acid on Ni, Pd and Pt surface is -0.36 , -0.39 and -0.40 eV, respectively. The barrier of formic acid dissociation into formate and hydrogen is 0.41 , 0.58 and 0.94 eV; respectively. These data show that formic acid has close adsorption energies on three metal surfaces, but has the lowest dissociation barrier on Ni surface and the highest barrier on Pt surface.

The adsorption energy of formate on Ni, Pd and Pt surface is -2.83 , -2.37 and -2.32 eV, respectively; and the effective barrier of formate dissociation into hydrogen and CO_2 is 1.03 , 0.76 and 1.56 eV, respectively. These data show that Ni surface has the strongest formate adsorption, while Pt has the highest barrier for formate dissociation. These computed data indicate clearly that Pd catalyzed formic acid dehydrogenation has the lowest effective barrier (0.76 eV), followed by Ni (1.03 eV) and Pt (1.56 eV).

(c) Formic acid adsorption and dissociation on metal oxides: Apart from metallic catalysts, metal oxides were also considered as catalysts for formic acid dehydrogenation. For example, formic acid adsorbs dissociatively on $\text{ZnO}(10\bar{1}0)$ ²³ to form surface formate and hydroxyl without energy barrier, and the dissociative adsorption energy is -3.45 eV. On TiO_2 ²² formic acid dissociatively adsorbs to form formate and surface hydroxyl, and the calculated dissociative adsorption energy is -1.39 eV (1/2 ML). On $\text{MgO}(111)$,²⁰ the most stable structure of molecular formic acid adsorption is our **1a**-like configuration with the O (O=C) and H (H-O) atoms interacting with the surface Mg and O atoms, respectively, and the adsorption energy is -0.89 eV; and the energy barrier of the O-H dehydrogenation is 0.75 eV and the dissociative adsorption energy is -0.59 eV.

2.4 Conclusions

Under the consideration of hydrogen production or carbon dioxide utilization, the adsorption and dehydrogenation of formic acid (HCO_2H) on the Ni(111) surface have been computed at the level of spin-polarized density functional theory. For the adsorption of formic on Ni(111), the most stable adsorption configuration (**1a**) has formic acid nearly perpendicular over the surface with the carbonyl oxygen atom (O=C) at atop and the hydroxyl hydrogen atom (O-H) bridging two neighbouring nickel atoms. This stable configuration is supported by the agreement between the computed and experimentally determined vibrational frequencies of deuterated formic acid (DCO_2H) on nickel surface. The expected isotope effect has been observed from the computed vibrational frequencies of formic acid and deuterated formic acid.

The most stable adsorption configuration of formate (HCO_2) has the bidentate bridging structure (**2a**) with its two oxygen atoms (C-O) at atop sites. This stable configuration (**2a**) is

evidenced by the well agreement between the computed and experimentally determined vibrational frequencies of deuterated formate (DCO_2) on nickel surface. In addition, the 3-fold capping structure with single oxygen atom (**2b**) and the bidentate structure with one oxygen atom (C-O) and one hydrogen atom (C-H) at atop sites (**2c**) are less stable local minimums. It is to note that such bidentate structures (**2a** and **2c**) in equilibrium have been observed in a very recent experiment on nano-sized Pd facet.¹⁷

On Ni(111) formic acid dehydrogenation into surface formate and hydrogen ($\text{HCO}_2\text{H} \rightarrow \text{HCO}_2 + \text{H}$) has barrier of 0.41 eV and is thermodynamic by 0.35 eV at co-adsorption. Formate dehydrogenation ($\text{HCO}_2 \rightarrow \text{CO}_2 + \text{H}$) goes via several steps from **2a** to **2c**, as well as has effective barrier of about 1.0 eV and is the rate-determining step.

Our computed adsorption configuration and energetic data for formic acid dehydrogenation on Ni(111) are very close and similar to the reported results for Pt(111), but in sharp contrast to the previously reported results for Pd(111).¹⁸ Our recalculated adsorption configurations and energetic data for formic acid dehydrogenation on Pd(111) show the high similarities on Ni(111), Pd(111) and Pt(111). However, it is found that on three metal surfaces, formic acid has close adsorption energies; and the calculated effective barrier for formic acid dehydrogenation is the lowest on Pd surface (0.76 eV), and the highest on Pt surface (1.56 eV); and that on Ni surface has the intermediate value (1.03 eV).

2.5 References

- (1) Züttel, A.; Borgschulte, A.; Schlapbach, L., Eds.; *Hydrogen as a Future Energy Carrier*, Wiley VCH, Weinheim, **2008**.
- (2) Johnson, T. C.; Morris, D. J.; Wills, M. *Chem. Soc. Rev.* **2010**, 39, 81–88.
- (3) Columbia, M. R.; Thiel, P. A. *J. Electroanal. Chem.* **1994**, 369, 1–14. (b) Madix, R. J. *Adv. Catal.* **1980**, 29, 1–53.
- (4) (a) Boddien, A.; Loges, B.; Gärtner, F.; Torborg, C.; Fumino, K.; Junge, H.; Ludwig, R.; Beller, M. *J. Am. Chem. Soc.* **2010**, 132, 8924–8934. (b) Loges, B.; Boddien, A.; Gärtner, F.; Junge, H.; Beller, M. *Top Catal.* **2010**, 53, 902–914. (c) Junge, H.; Boddien, A.; Capitta, F.; Loges, B.; Noyes, J. R.; Gladiali, S.; Beller, M. *Tetrahedron Lett.* **2009**, 50, 1603–1606. (d) Boddien, A.; Loges, B.; Junge, H.; Gärtner, F.; Noyes, J. R.; Beller, M. *Adv. Synth. Catal.* **2009**, 351, 2517–2520. (e) Loges, B.; Boddien, A.; Junge, H.; Beller, M. *Angew. Chem. Int. Ed.* **2008**, 47, 3962–3965. (f) Boddien, A.; Loges, B.; Junge, H.; Beller, M. *ChemSusChem.* **2008**, 1, 751–758.
- (5) Fellay, C.; Dyson, P. J.; Laurenczy, G. *Angew. Chem. Int. Ed.* **2008**, 47, 3966–3968.
- (6) Fukuzumi, S. *Eur. J. Inorg. Chem.* **2008**, 1351–1362.
- (7) Jessop, P. G.; Hsiao, Y.; Ikariya, T.; Noyori, R. *J. Am. Chem. Soc.* **1996**, 118, 344–355.
- (8) Gazsi, A.; Bánsági, T.; Solymosi, F. *J. Phys. Chem. C* **2011**, 115, 15459–15466.
- (9) Koós, Á.; Solymosi, F. *Catal. Lett.* **2010**, 138, 23–27

- (10) (a) Zhou, X.; Huang, Y.; Xing, W.; Liu, C.; Liao, J.; Lu, T. *Chem. Commun.* **2008**, 3540–3542. (b) Ojeda, M.; Iglesia, E. *Angew. Chem. Int. Ed.* **2009**, *48*, 4800–4803. (c) Bulushev, D. A.; Beloshapkin, S.; Ross, J. R. H. *Catal. Today* **2010**, *154*, 7–12.
- (11) Schaub, T.; Paciello, R. A. *Angew. Chem. Int. Ed.* **2011**, *50*, 7278–7282.
- (12) (a) Ohnishi, Y. Y.; Nakao, Y.; Sato, H.; Sakaki, S. *Organometallics* **2006**, *25*, 3352–3363. (b) Ohnishi, Y. Y.; Matsunaga, T.; Nakao, Y.; Sato, H.; Sakaki, S. *J. Am. Chem. Soc.* **2005**, *127*, 4021–4032. (c) Musashi, Y.; Sakaki, S. *J. Am. Chem. Soc.* **2000**, *122*, 3867–3877.
- (13) Musashi, Y.; Sakaki, S. *J. Am. Chem. Soc.* **2002**, *124*, 7588–7603.
- (14) Wang, H. F.; Liu, Z. P. *J. Phys. Chem. C* **2009**, *113*, 17502–17508.
- (15) Neurock, M.; Janik, M.; Wieckowski, A. *Faraday Discuss.* **2009**, *140*, 363–378.
- (16) (a) Gao, W.; Keith, J. A.; Anton, J.; Jacob, T. *J. Am. Chem. Soc.* **2010**, *132*, 18377–18385. (b) Gao, W.; Keith, J. A.; Anton, J.; Jacob, T. *Dalton Trans.* **2010**, *39*, 8450–8456.
- (17) Tedsree, K.; Chan, C. W. A.; Jones, S.; Cuan, Q.; Li, W. K.; Gong, X. Q.; Tsang, S. C. E. *Science* **2011**, *322*, 224–228.
- (18) Zhou, S.; Qian, C.; Chen, X. *Catal. Lett.* **2011**, *141*, 726–734.
- (19) Yue, C. M. Y.; Lim, K. H. *Catal. Lett.* **2009**, *128*, 221–226.
- (20) Nakatsuji, H.; Yoshimoto, M.; Hada, M.; Domen, K.; Hirose, C. *Surf. Sci.* **1995**, *336*, 232–244.
- (21) Senanayake, S. D.; Mullins, D. R. *J. Phys. Chem. C* **2008**, *112*, 9744–9752.
- (22) (a) Uemura, Y.; Taniike, T.; Tada, M.; Morikawa, Y.; Iwasawa, Y. *J. Phys. Chem. C* **2007**, *111*, 16379–16386. (b) Morikawa, Y.; Takahashi, I.; Aizawa, M.; Namai, Y.; Sasaki, T.; Iwasawa, Y. *J. Phys. Chem. B* **2004**, *108*, 14446–14451.
- (23) Nakatsuji, H.; Yoshimoto, M.; Umemura, Y.; Takagi, S.; Hada, M. *J. Phys. Chem.* **1996**, *100*, 694–700.
- (24) Poulston, S.; Rowbotham, E.; Stone, P.; Parlett, P.; Bowker, M. *Catal. Lett.* **1998**, *52*, 63–67.
- (25) Halawy, S.; Al-Shihry, S.; Mohamed, M. *Catal. Lett.* **1997**, *48*, 247–251.
- (26) Patermarakis, G. *Appl. Catal. A* **2003**, *252*, 231–241.
- (27) Hu, Y. H.; Ruckenstein, E. *Adv. Catal.* **2004**, *48*, 297–345.
- (28) Zhu, Y. A.; Chen, D.; Zhou, X. G.; Yuan, W. K. *Catal. Today* **2009**, *148*, 260–267.
- (29) (a) Wang, S. G.; Liao, X. Y.; Hu, J.; Cao, D. B.; Li, Y. W.; Wang, J.; Jiao, H. *Surf. Sci.* **2007**, *601*, 1271–1284. (b) Wang, S. G.; Cao, D. B.; Li, Y. W.; Wang, J.; Jiao, H. *J. Phys. Chem. B* **2006**, *110*, 9976–9983.
- (30) (a) Wang, S. G.; Cao, D. B.; Li, Y. W.; Wang, J.; Jiao, H. *Surf. Sci.* **2009**, *603*, 2600–2606. (b) Wang, S. G.; Cao, D. B.; Li, Y. W.; Wang, J.; Jiao, H. *Surf. Sci.* **2006**, *600*, 3226–3234.
- (31) Wang, S. G.; Cao, D. B.; Li, Y. W.; Wang, J.; Jiao, H. *J. Phys. Chem. B* **2005**, *109*, 18956–18963.
- (32) Wang, G. C.; Zhou, Y. H.; Morikawa, Y.; Nakamura, J.; Cai, Z. S.; Zhao, X. Z. *J. Phys.*

Chem. B **2005**, *109*, 12431-12442.

(33) Remediakis, I. N.; Abild-Pedersen, F.; Nørskov, J. K. *J. Phys. Chem. B* **2004**, *108*, 14535–14540.

(34) Watwe, R. M.; Bengaard, H. S.; Rostrup-Nielsen, J. R.; Dumesic, J. A.; Nørskov, J. K. *J. Catal.* **2000**, *189*, 16–30.

(35) Oliva, C.; Berg, C. V. D.; Niemantsverdriet, J. W.; Curulla-Ferré, D. *J. Catal.* **2007**, *245*, 436–445.

(36) Mittendorfer, F.; Hafner, J. *J. Phys. Chem. B* **2002**, *106*, 13299–13305.

(37) (a) Kresse, G.; Hafner, J. *Phys. Rev. B* **1993**, *47*, 558–561. (b) Kresse, G.; Hafner, J. *Phys. Rev. B* **1994**, *49*, 14251–14269. (c) Kresse, G.; Furthmüller, J. *Comput. Mater. Sci.* **1996**, *6*, 15–50. (d) Kresse, G.; Furthmüller, J. *Phys. Rev. B* **1996**, *54*, 11169–11186.

(38) Perdew, J. P.; Bruke, K.; Ernzerhof, M. *Phys. Rev. Lett.* **1996**, *77*, 3865–3868.

(39) Blöchl, P. E. *Phys. Rev. B* **1994**, *50*, 17953–17979.

(40) Methfessel, M.; Paxton, A. T. *Phys. Rev. B* **1989**, *40*, 3616–3621.

(41) Monkhorst, M.; Pack, J. D. *Phys. Rev. B* **1976**, *13*, 5188–5192.

(42) Christmann, K.; Schober, O.; Ertl, G.; Neumann, M. *J. Chem. Phys.* **1974**, *60*, 4528–4540.

(43) Smart, J. M. *Effective Field Theories of Magnetism*. W. B. Saunders Company, Philadelphia-London, **1966**, p46.

(44) Jónsson, H.; Mills, G.; Jacobsen, K.W. In *Classical and Quantum Dynamics in Condensed Phase Simulations*; Berne, B. J.; Ciccotti, D. F. Eds, World Scientific: Singapore, **1998**; p385.

(45) Erley, W; Sander, D. *J. Vac. Sci. Technol, A* **1989**, *7*, 2238–2244.

(46) Ruka, R. L.; Brockway, L. O.; Boggs, J. E. *J. Am. Chem. Soc.* **1959**, *81*, 2930–2933; and the cited references therein.

(47) Pang, X. Y.; Wang, C.; Zhou, Y. H.; Zhao, J. M.; Wang, G. C. *J. Mol. Struct (THEOCHEM)* **2010**, *948*, 1–10.

(48) Bandara, A.; Kubota, J.; Wada, A.; Domen, K.; Hirose, C. *Appl. Phys. B* **1999**, *68*, 573–578.

(49) Yang, H.; Whitten, J. L. *J. Chem. Phys.* **1993**, *98*, 5039–5049.

(50) Ishiwatari, R.; Tachikawa, M. *J. Mol. Struct.* **2005**, *735–736*, 383–387.

(51) Johnson, A. D.; Daley, S. P.; Utz, A. L.; Ceyer, S. T. *Science*, **1992**, *257*, 223–225.

(52) Daley, S. P.; Utz, A. L.; Trautman, T. R.; Ceyer, S. T. *J. Am. Chem. Soc.* **1994**, *116*, 6001–6002.

(53) Yang, H.; Whitten, J. L. *Surf. Sci. Lett.* **1993**, *294*, L945–L951.

(54) Yang, H.; Whitten, J. L. *Appl. Surf. Sci.* **1994**, *75*, 12–20.

(55) Michaelides, A.; Hu, P.; Alavi, A. *J. Chem. Phys.* **1999**, *111*, 1343–1345.

(56) Kresse, G.; Hafner, J. *Surf. Sci.* **2000**, *459*, 287–302.

- (57) Ledentu, V.; Dong, W.; Sautet, P. *J. Am. Chem. Soc.* **2000**, *122*, 1796–1801.
- (58) Greeley, J.; Mavrikakis, M. *Surf. Sci.* **2003**, *540*, 215–229.
- (59) Henkelman, G.; Arnaldsson, A.; Jónsson, H. *J. Chem. Phys.* **2006**, *124*, 044706–9.
- (60) Benziger, J. B.; Schoofs, G. R. *J. Phys. Chem.* **1984**, *88*, 4439–4444.
- (61) Bakó, I.; Pálinkás, G. *Surf. Sci.* **2006**, *600*, 3809–3814.
- (62) Hartning, C.; Grimminger, J.; Spohr, E. *J. Electroanal. Chem.* **2007**, *607*, 133–139.

3 Formic Acid Dehydrogenation on Ni(211), Pd(211) and Pt(211)

3.1 Introduction

Hydrogen generation from formic acid (FA) has attracted increasing attention, and this is because that FA has been considered as one of the energy resources in future energy society and CO₂ emission.¹⁻⁵ Since FA can either dehydrogenate into H₂ and CO₂ or dehydrate into H₂O and CO, the selective dehydrogenation of FA into H₂ is of critical importance in the usage of FA as H₂ resource; and the key points in this selective reaction are cheap and active catalysts.

Beller *et al.*,⁶ has made a breakthrough in H₂ generation from FA using iron complexes [Fe(BF₄)₂·6H₂O/PP₃] under mild condition in a green solvent without using amine and light. Alternatively, on heterogeneous catalysis, core-shell catalyst was considered to be effective in FA dehydrogenation, e. g.; Tedsree *et al.*,⁷ reported that the Ag-Pd core shell can enhance H₂ production from FA at ambient temperature. Kang *et al.*,⁸ reported that the Pt₃Pb nanocrystals and the core-shell Pt₃Pb-Pt nanocrystals are more efficient for FA oxidation than only Pt metal. Bimetallic Au-Pd nanoparticles immobilized in mesoporous metal organic frameworks also are efficient catalysts in H₂ generation from FA.⁹ In addition, Bi *et al.*,¹⁰ reported the selective decomposition of FA/amine mixtures without CO formation using ultra dispersed subnanometric Au catalysts on acid-tolerant ZrO₂ under ambient conditions in high efficiency.

Along with the intensive experimental studies of FA dehydrogenation, many computational investigations into the mechanisms of FA dissociation have been carried out,¹¹ and nowadays computational chemistry plays an increasingly important role in understanding chemical reactions, especially in the fields of homogenous and heterogeneous catalysis.¹² Recent computational studies show that FA has similar trends in adsorption and dissociation on the M(111) surfaces (M = Ni,¹³ Pd,^{13,14} and Pt¹⁵), and the most favorable reaction path is the formate route (HCOOH → H + HCOO; and HCOO → H + CO₂). Such reaction route has been confirmed by the very recent studies on FA dissociation on Pt(111)¹⁶ and on M(111) with M = Pd, Pt, Rh, Au,¹⁷ as well as on a Pd₇ cluster.¹⁸

Compared with the numerical theoretical studies for FA adsorption and dissociation on the M(111) surfaces, the M(211) surfaces were not considered (M = Ni, Pd, Pt). To further understand the differences in FA dehydrogenation of these metals, we are interested in the catalytic properties of the more open (211) surfaces. The different catalytic activities of M(211) and M(111) have been reported for other reactions. Bengaard *et al.*,¹⁹ found that the Ni(211) surface associated with certain stepped defect sites is more active for steam reforming process (CH₄ + H₂O → CO + 3H₂) than the Ni(111) surface associated with the closed-packed facets. Cao *et al.*,²⁰ reported the direct and H-mediated CO₂ dissociation on the Ni(211) surface and found that CO₂ prefers to adsorb at the stepped site and stepped edge sites, and

the formation of HCO_2 is favored thermodynamically, and CO direct dissociation into $\text{CO}+\text{O}$ is more favorable kinetically than that of HCO_2 into $\text{HCO}+\text{O}$. King *et al.*,²¹ reported that CO has stronger adsorption on the Pt(211) surface than on the Ni(211) surface at every CO coverages. Orita *et al.*,²² found that the most stable CO adsorption configuration is the atop site on the step edge on the Pt(211) surface, while at the bridging site parallel to the step edge on the Ni(211) and Pd(211) surfaces. Orita *et al.*,²³ found that NO has the bridging adsorption configuration parallel to the step edge on the Ni(211) and Pd(211) surfaces, and the Ni(211) surface is more active for NO decomposition than the Pd(211) surface. Hammer²⁴ studied NO dissociation on the Pd(211) and Pd(111) surfaces, and found that NO prefers to dissociate on the Pd(211) surface than on the Pd(111) surface because of the stronger adsorption of NO as well as N and O on the Pd(211) surface than on the Pd(111) surface. NO reduction by CO ($2\text{NO} + 2\text{CO} = \text{N}_2 + 2\text{CO}_2$) has been computed by Hammer²⁵ on the Pd(111), Pd(100), stepped Pd(211), and edged missing-row reconstructed Pd(311) surfaces; and the energy barriers for NO dissociation and N_2 association are much smaller at the Pd steps and edges than at the flat Pd(111) and Pd(100) surfaces.

The adsorption and diffusion of H on the Pd(211) and Pd(111) surfaces were studied by Hong *et al.*,²⁶ and the hollow sites are most favorable for H adsorption on both surfaces, and H can easier diffuse from the preferred surface site to the subsurface on the Pd(211) surface than on the Pd(111) surface. However, Hou *et al.*,²⁷ reported the four-fold hollow site to be most stable for H adsorption on the Pd(211) surface. Olsen *et al.*,²⁸ also reported a bridge H on the step edge of the Pt(211) surface to be a deep global minimum on the potential energy surface. Vehviläinen²⁹ reported the electronic properties of H atom adsorption on the Pt(111), Pt(211) and Pt(311) surfaces, and found that the steps modify the potential energy surface considerably.

We report our computational results about FA dehydrogenation into CO_2 and hydrogen on the M(211) M = Ni, Pd and Pt surfaces. Our goal is the differences of these three metals in FA dissociation and also the differences to the corresponding M(111) surface. All these results have been listed and compared in [Table 3.1](#).

3.2 Computational models and details

All calculations were performed using the plane-wave based periodic density functional method as implemented in the Vienna *Ab Initio* Simulation Package (VASP).³⁰⁻³³ The exchange and correlation energies were calculated using the Perdew, Burke and Ernzerhof (PBE)³⁴ functional within the generalized gradient approximation (GGA). The electron-ion interaction was described by the projector augmented wave (PAW) method,³⁵ and the Kohn-Sham one-electron states were expanded in a plane wave basis set up to 400 eV for Ni, and 500 eV for Pd and Pt. Electron smearing of $\sigma = 0.1$ eV³⁶ was used following the Methfessel-Paxton scheme. Spin polarization was included for the correct description of the magnetic properties.

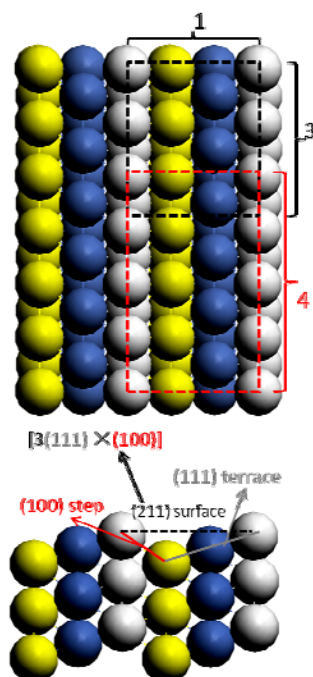


Figure 3.1 Top and side views of M(211) in (1×3) and (1×4) cell size

For optimizing the crystal lattices all atoms were fully relaxed with the forces converged to be less than 0.02 eV/Å and the total energy converged to be less than 10^{-5} eV. Brillouin zone sampling was employed using a Monkhorst-Pack grid.³⁷ The calculated crystal lattice for Ni, Pd and Pt is 352, 396, 398 pm, respectively, and they are in close agreement with the available experimental data (352 pm for Ni,³⁸ as well as 389 pm for Pd and 391 pm for Pt³⁹).

The Ni(211) surface was modeled by a nine-layer periodic slab within a (1×3) super cell (Figure 3.1); the three top layers were allowed to relax, and the bottom six layers were fixed in their bulky positions. The vacuum slab was set up to 10 Å. This model was well tested and used by Cao *et al.*,²⁰ in CO₂ dissociation on the Ni(211) surface. For the Pd(211) and Pt(211) surfaces, we used a six-layer slab within a (1×4) super cell; the top three layers were relaxed and the bottom three layers were fixed in their bulky positions. The vacuum gap was set up to 12 Å. This model was used and tested by Hu *et al.*,⁴⁰ in selective acrolein hydrogenation.

The first Brillouin zone was sampled with 3×3×1 *k*-point grid for the Ni(211) surface, and with 2×2×1 *k*-point grid for the Pd(211) and Pt(211) surfaces. The nudged elastic band (NEB) method was used to locate the transition state (TS) between an initial state (IS) and a final state (FS).⁴¹ The adsorption energy is defined as $E_{\text{ads}} = E_{\text{X/slab}} - [E_{\text{slab}} + E_{\text{X}}]$, where $E_{\text{X/slab}}$ is the total energy of the slab with adsorbate X, E_{slab} is the total energy of the bare slab, and E_{X} is the total energy of free adsorbate X; a negative E_{ads} means an exothermic adsorption and a positive E_{dis} indicates an endothermic adsorption; and the more negative the E_{ads} , the stronger the adsorption. The dissociation barrier is defined as $E_{\text{a}} = E_{\text{TS}} - E_{\text{IS}}$, and E_{TS} and E_{IS} are the total energies of the TS and IS. The dissociation energy is defined as $E_{\text{dis}} = E_{\text{FS}} - E_{\text{IS}}$, and E_{FS}

and E_{IS} are the total energies of the FS and IS; and a negative E_{dis} means an exothermic reaction and a positive E_{dis} indicates an endothermic reaction.

3.3 Results and discussion

3.3.1 HCO₂H adsorption

The configurations of FA adsorption and dissociation on the M(211) surfaces are shown in Figure 3.2, and FA has the adsorption configuration of O/OH-down, in which the O (O=C) atom adsorbs atop on a first-layer metal atom and the H(O-H) atom points towards to two second layer neighboring surface metal atoms. The O–M distance is 198, 218, 213 pm for M = Ni, Pd, Pt, respectively. The H–M distances are 247/246, 252/255, 253/258 pm, for M = Ni, Pd, Pt, respectively. The computed E_{ads} on M(211) is -0.69 , -0.58 , -0.61 eV for M = Ni, Pd, Pt, respectively, indicating an exothermic and thermodynamically favorable process.

The same adsorption configuration is found on M(111),¹³ but the E_{ads} is lower, e.g.; -0.36 ¹³ and -0.43 eV⁴² on the Ni(111) surface, -0.39 ,¹³ -0.40 ,¹⁴ -0.40 eV¹⁷ on the Pd(111) surface, and -0.40 eV on the Pt(111) surface.¹⁵ Depending on the size of the unit cells, the computed E_{ads} on the Pt(111) surface varies in some extent, e.g.; -0.26 eV (2×4),¹³ -0.40 eV (3×3) and -0.34 eV (2×2),¹⁵ -0.39 eV (3×3),¹⁷ -0.42 eV (3×2√3),⁴³ -0.37 eV (4×4).⁴⁴ However, Zhang *et al.*,¹⁶ reported a stronger E_{ads} (-0.62 eV) for FA on Pd(111) with the same adsorption configuration and at the same coverage (1/9 ML), but by using the DMol³ program.

3.3.2 HCO₂H dissociation

On the basis of the most stable adsorption configuration (O/OH-down) of FA on the M(211) surfaces, the expected dissociation reaction is the formate route ($\text{HCOOH} \rightarrow \text{HCO}_2 + \text{H}$); and this is also the same as found on the M(111) surfaces.^{13–18} In the transition states (Figure 3.2), the O–M distance is 192, 208, 205 pm for M = Ni, Pd, Pt, respectively, and they are shorter than those in the initial states. The H–M distances are 174/174, 176/178, 181/187 pm, for M = Ni, Pd, Pt, respectively, and they are much shorter than those in the initial states. The most important change is the breaking O–H distance in the transition states, 159, 178, 172 pm, for M = Ni, Pd, Pt, respectively, and they are much longer than those in the initial states (102 pm). The computed E_a on the M(211) surfaces is 0.42, 0.53, 0.51 eV for M = Ni, Pd, Pt, respectively, and the E_{dis} leading to surface formate and H atom is -0.95 , -0.44 , -0.81 eV, for M = Ni, Pd, Pt, respectively, indicating an exothermic and thermodynamically favorable process.

Compared with the M(211) surfaces, the computed FA E_a is 0.41 eV on the Ni(111) surface and 0.58 eV on the Pd(111) surface,¹³ and they are close to those on the Ni(211) and Pd(211) surfaces. There are also some available E_a data for Pd(111), 0.21,¹⁴ 1.00,¹⁶ and 0.68 eV.¹⁷ On the Pt(111) surface, there are several data available depending on the size of the unit cells, e. g.; 0.94 (3×3),¹⁵ 0.88 (2×2),¹⁵ 0.72 (2×4),¹³ and 0.69 eV (3×3),¹⁷ and they are higher than on the Pt(211) surface. The computed FA E_{dis} into formate and H is -0.60 eV on Ni(111),¹³ -0.17 ,¹³ 0.00¹⁶ and -0.27 eV¹⁷ on Pd(111), and 0.03 eV on Pt(111).¹⁷

These detailed comparisons show that the M(211) surfaces can adsorb FA more strongly

than the M(111) surfaces, and Ni(211) and Ni(111) as well as Pd(211) and Pd(111) have close E_a according to our calculations; while Pt(211) has lower E_a than Pt(111).

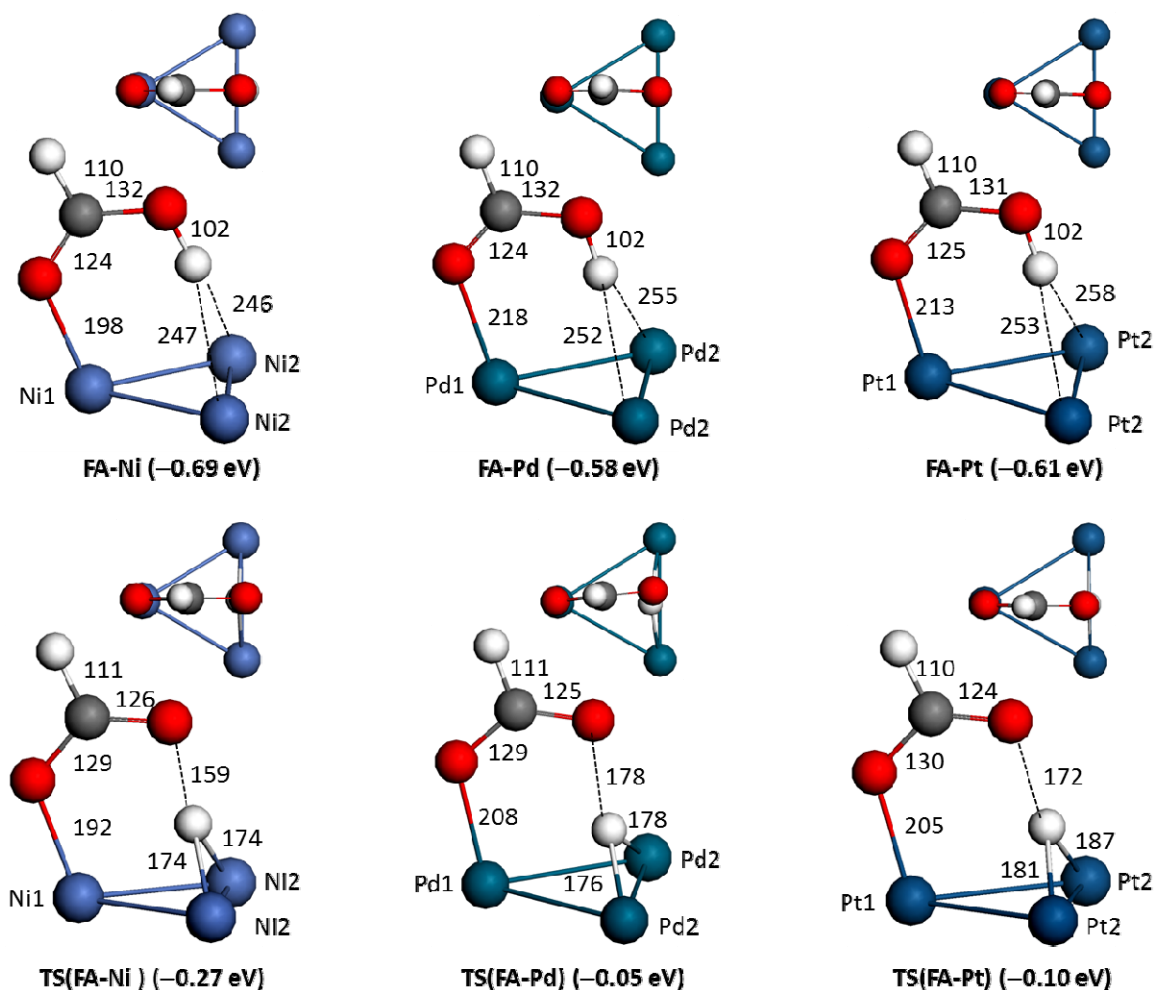


Figure 3.2 Adsorption configurations of FA as well as the transition state of FA dissociation into formate and H on M(211) M = Ni, Pd, Pt (H in white, C in gray, O in red, Ni in blue, Pd in blue-green, and Pt in deep-green; bond distances in pm and energies in eV)

3.3.3 HCO₂ adsorption and dissociation

On the basis of FA dissociation, surface formate has been formed. The adsorbed formate has the bidentate bridging configuration of O/O-down, in which its two oxygen atoms interact directly with the surface M atoms; and this is also the same as found on M(111) surfaces.^{13–18} As shown in Figure 3.3, the O–M distances are 193, 210, 207 pm for M = Ni, Pd, Pt, respectively, and the corresponding C–H and C–O distances are 111 and 127 pm. The computed E_{ads} of formate is -3.49 , -2.82 , -3.04 eV for M = Ni, Pd, Pt, respectively.

On the M(111) surfaces, the E_{ads} of formate is -2.83 ¹³ and -3.03 eV⁴² for Ni(111), -2.37 ,¹³ -0.68 ,¹⁴ -2.71 ,¹⁶ and -2.52 eV¹⁷ for Pd(111) as well as -2.32 (3×3) and -2.50 (2×2)¹⁵ as well as -2.27 ¹⁷ and -2.45 eV³⁹ for Pt(111). These show that M(211) can adsorb formate more

strongly than M(111).

On the basis of the formate adsorption configuration of O/O-down, a direct C–H activation and dissociation is not possible due to its orientation pointing away from the surface. However, the flat adsorption configuration of formate on the surface,⁴⁵⁻⁴⁹ which has been considered as a key intermediate for C–H bond activation, could not be located. It is to note that such flat adsorption configuration also has been not found on Ni(111)¹³ and Pd (111),^{13,16,17} and there are no reports about such adsorption configurations on Pt(111), Rh(111) and Au(111).¹⁷

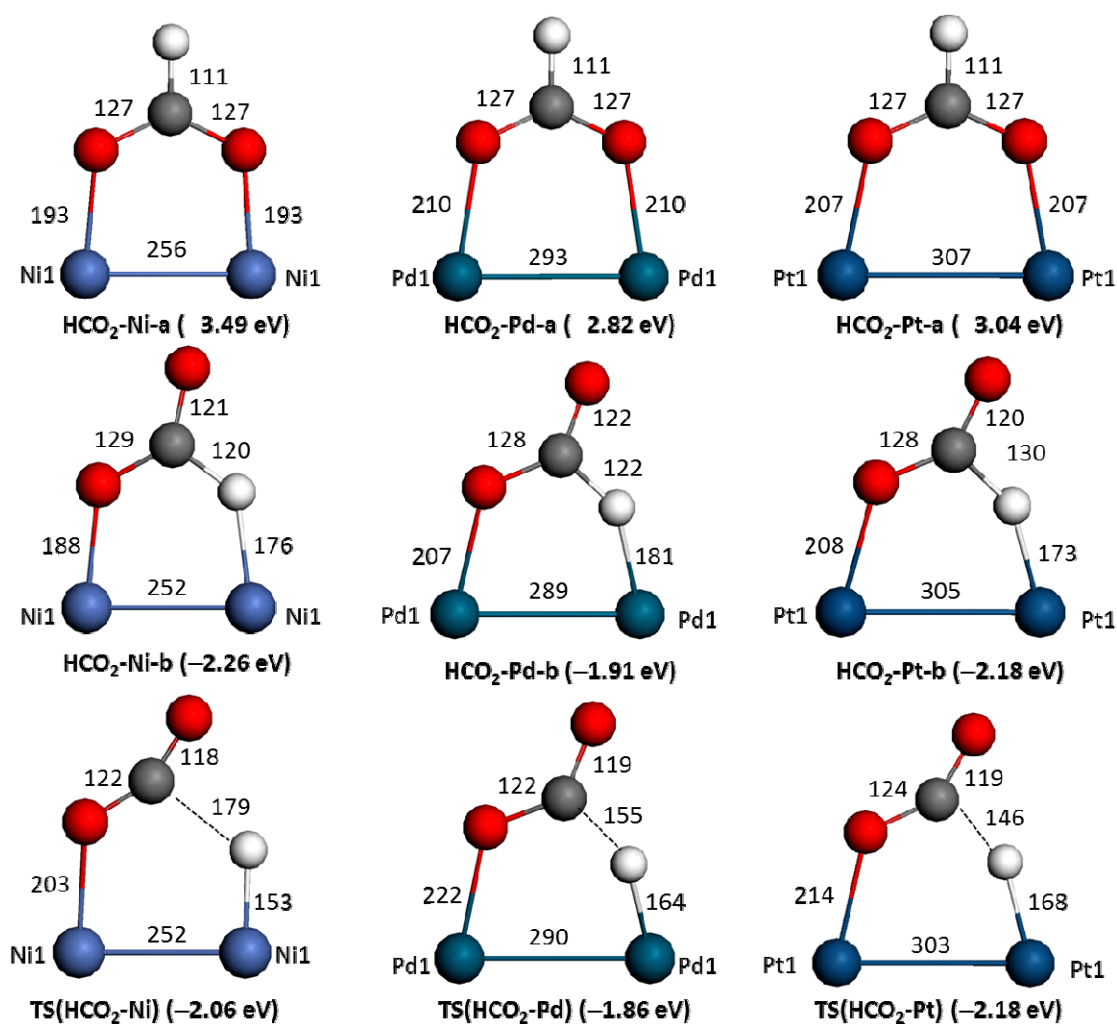


Figure 3.3 Adsorption configurations of formate as well as the transition state of formate dissociation into CO_2 and H on M(211) M = Ni, Pd, Pt (H in white, C in gray, O in red, Ni in blue, Pd in blue-green, and Pt in deep-green; bond distances in pm and energies in eV)

Another key intermediate which can facilitate C–H activation and dissociation has the bidentate bridging configuration of O/H-down,¹³⁻¹⁷ in which one oxygen atom and the hydrogen atom interact with the surface M atoms (Figure 3.3). In the O/H-down adsorption configuration, the O–M distance is 188, 207, 208 pm, respectively, for M = Ni, Pd, Pt; and the

corresponding H–M distance is 176, 181, 173 pm and the C–H distance is 120, 122, 130 pm. However, the computed E_{ads} is -2.26 , -1.91 , -2.18 eV, respectively, for M = Ni, Pd, Pt; and they are much lower than those for the O/O-down adsorption configuration by 1.23, 0.91 and 0.86 eV, respectively.

For formate dissociation, the breaking C–H distance is 179, 155, 146 pm for M = Ni, Pd, Pt, respectively, and the corresponding M–H distance is 153, 164, 168 pm. The computed E_a is 0.20, 0.05, 0.00 eV, respectively, for M = Ni, Pd, Pt. These rather low barriers indicate that the C–H bond has been highly activated on M(211) and the potential energy surface is very flat. Indeed, additional calculations show negligible changes of the relative energy along with the variation of the C–H and M–H distances.

On the basis of the most stable formate adsorption configuration of O/O-down on M(211), the computed effective barrier for formate dissociation is 1.43, 0.96, 0.86 eV for M = Ni, Pd, Pt, respectively. This shows that Ni(211) has the highest effective barrier in formate dissociation, while Pt(211) has the lowest effective barrier.

On M(111), the computed effective barrier on Ni(111) and Pd(111) is 1.03 and 0.76 eV,¹³ respectively, and they are lower than those on Ni(211) and Pd(211), while the effective barrier [1.56 eV (3×3),¹⁵ 1.16 eV (2×2)¹⁵ and 1.23 eV(2×4)¹³ on Pt(111) is higher than that on Pt(211). On the basis of the computed effective barriers for formate dissociation, Ni(111) and Pd(111) are more effective than Ni(211) and Pd(211), while Pt(211) is more effective than Pt(111). However, Hu *et al.*,¹⁷ reported the effective barrier on Pd(111) and Pt(111) is 1.59 and 1.88 eV, respectively, and they are much higher than our data, and Zhang *et al.*,¹⁶ reported an effective barrier on Pd(111) of 0.88 eV, which is interestingly lower than the barrier of FA dissociation.

3.3.4 H adsorption on M(211)

As one of the surface intermediates, we calculated H adsorption on M(211). Hydrogen adsorption on metal surfaces is of crucial importance for understanding hydrogen related chemical processes, e.g.; hydrogenation, dehydrogenation and hydrogenolysis reactions.⁵⁰ On M(211), there are several sites for H adsorption, and all have very close adsorption energies.

On Ni(211), we found five adsorption sites for H atom, and the most stable site is the three-fold site on the (111) terrace with E_{ads} of -2.74 eV, and the least stable site is the four-fold site on the (100) step with E_{ads} of -2.59 eV. Our results are different from those reported by Bengaard *et al.*,¹⁹ they found the bridge site at the step on Ni(211) as the most stable site and the five-fold site at the step and different three-fold sites at the (111) terrace are higher in energy. It is to note that the E_{ads} of H on Ni(111) is -2.76 eV,¹³ which is close to that value on Ni(211).

On Pd(211), we also found five adsorption sites for H atom, and the most stable site is the three-fold site with E_{ads} of -2.79 eV; and the least stable adsorption site is the four-fold site on the (100) step with E_{ads} of -2.65 eV. Our results are in agreement with the data (-2.79 vs.

–2.63 eV) by Hong *et al.*,²⁶ and by Andersin and Honkala,⁵¹ but differ from those by Hou *et al.*,²⁷ and they reported the four-fold hollow site at the step to be most stable (–3.02 eV).

On Pt(211), we found four adsorption sites for H atom, and the four-fold site on the (100) step could not be found. The most stable site is the two-fold bridging site on two neighboring Pt atoms with E_{ads} of –2.97 eV, and the least stable site is the three-fold site on the (111) terrace with E_{ads} of –2.61 eV. Our result agrees well with previous work.^{28,29,52,53}

3.3.5 CO₂ adsorption and desorption on M(211)

Apart from H, we calculated the adsorption and desorption of CO₂, and the adsorption configurations and structural parameters are shown in Figure 3.4. CO₂ activation is an important field in utilizing CO₂ as a cheap C1 feedstock for useful chemicals fuels.⁵⁴ The interaction mechanisms of CO₂ on transition metal surfaces have been studied,⁵⁵ and the d-band center of the metal surfaces and the charge transfer are the main factors in CO₂ activation.

On Ni(211), the adsorbed CO₂ has a tridentate configuration, in which not only the carbon atom but also the two oxygen atoms interact with the surface Ni atoms, and the Ni–C distances are 197 and 216 pm, and the Ni–O distances are 204 and 208 pm, and the O–C–O angle is 140.42°. The computed E_{ads} of CO₂ is –0.32 eV, and this value is rather lower than that (–0.93 eV) by Cao *et al.*,²⁰ using VASP-UUSP. The corresponding physisorbed CO₂ on Ni(211) also has been located and the Ni–O distances are rather long (320 and 327 pm), and the adsorption is rather weak (–0.03 eV). In addition, we have calculated the transition state of CO₂ desorption, in which the Ni–O distances are 300 and 305 pm, and the desorption barrier is 0.29 eV. The desorption transition state is both energetically and structurally close to the physisorbed state.

On Pd(211) and Pt(211), CO₂ has a bidentate adsorption configuration, in which one carbon and one oxygen atom interact with the surface metal atoms, and the distance of Pd–O and Pd–C is 214 and 204 pm, respectively; and the distance of Pt–O and Pt–C is 206 and 204 pm, respectively. The O–C–O angle is 139.95° on Pd(211) and 129.65° on Pt(211). The computed chemisorption energy is –0.13 and –0.27 eV on Pd(211) and Pt(211), respectively. The corresponding CO₂ physisorption on Pd(211) and Pt(211) has also been calculated (Figure 3.4), the physisorption is very weak (0.00 and 0.00 eV). Compared to the chemisorbed states, the transition state for CO₂ desorption has been located; in which the CO₂ still has a bent structure (O–C–O angle of 164.57° on Pd(211) and 160.94° on Pt(211)); and the Pd–O and Pd–C distances are 244 and 260 pm as well as the Pt–O and Pt–C distances are 239 and 267 pm. These distances are longer than those in the chemisorbed states. The desorption barrier is 0.22 eV on Pd(211) and 0.54 eV on Pt(211).

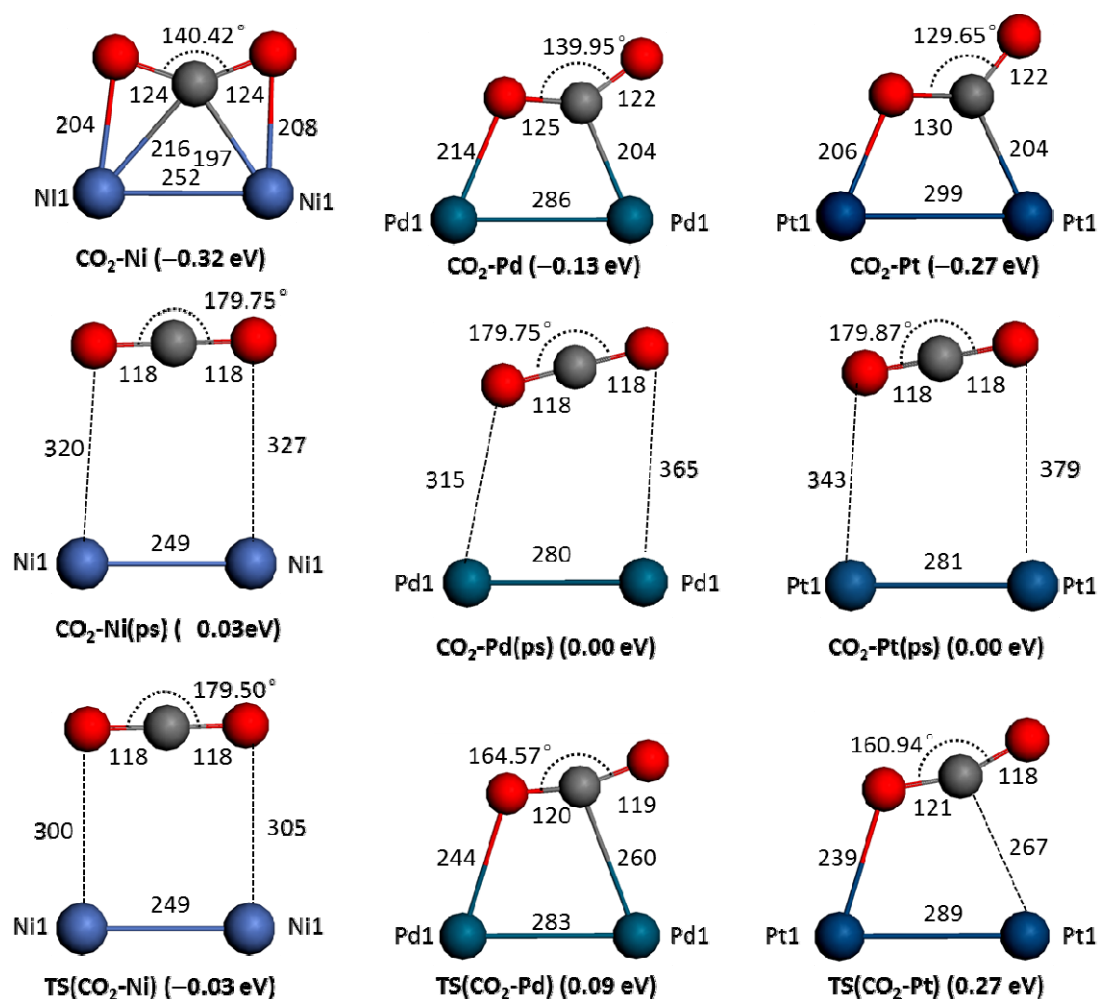


Figure 3.4 Adsorption configurations of CO_2 as well as the transition state of CO_2 desorption on $\text{M}(211)$ $\text{M} = \text{Ni}, \text{Pd}, \text{Pt}$ (C in gray, O in red, Ni in blue, Pd in blue-green, and Pt in deep-green; bond distances in pm and energies in eV)

It is known that CO_2 has a very weak physisorption (-0.06 eV) on $\text{Ni}(111)$,⁴² while prefers chemisorption (-0.14 eV⁵⁶) on $\text{Ni}(100)$ and (-0.42 ⁵⁶ or -0.47 ⁵⁷ eV) on $\text{Ni}(110)$. In addition, CO_2 has chemisorption on the $\text{M}(211)$ surface, while CO_2 has positive chemisorption energies on $\text{Ni}(111)$, $\text{Pd}(111)$ and $\text{Pt}(111)$.⁵⁵ Since the activation degree of CO_2 on metal surface is determined by the d-band center of the metal and the transferred charge from surface to metal,⁵⁵ we have calculated the net Bader-type charge⁵⁸ of the adsorbed CO_2 on the $\text{M}(211)$ surfaces. Compared to the adsorbed CO_2 on $\text{M}(111)$, $\text{M}(211)$ can transfer more negative charge to the adsorbed CO_2 , e.g.; -0.64 , -0.42 , -0.47 e for $\text{M} = \text{Ni}, \text{Pd}, \text{Pt}$, respectively, and the negative charge of the adsorbed CO_2 on $\text{M}(111)$ is -0.58 , -0.40 , -0.42 e for $\text{M} = \text{Ni}, \text{Pd}, \text{Pt}$, respectively (the calculated Mulliken charge on $\text{M}(111)$ ⁵⁵ is -0.44 , -0.36 , -0.37 e for $\text{M} = \text{Ni}, \text{Pd}, \text{Pt}$, respectively). The transferred charge on CO_2 on $\text{M}(211)$ is in line with the chemisorption energies. This difference can be ascribed to the surface metal atoms

interacting with CO_2 , in particular the metal atoms on the (100) step, e.g.; the metal atoms on the (100) step of M(211) are more open and less coordinated than those on the M(111) surface. In addition, the adsorbed CO_2 structure is more compact on M(211) than on M(111).

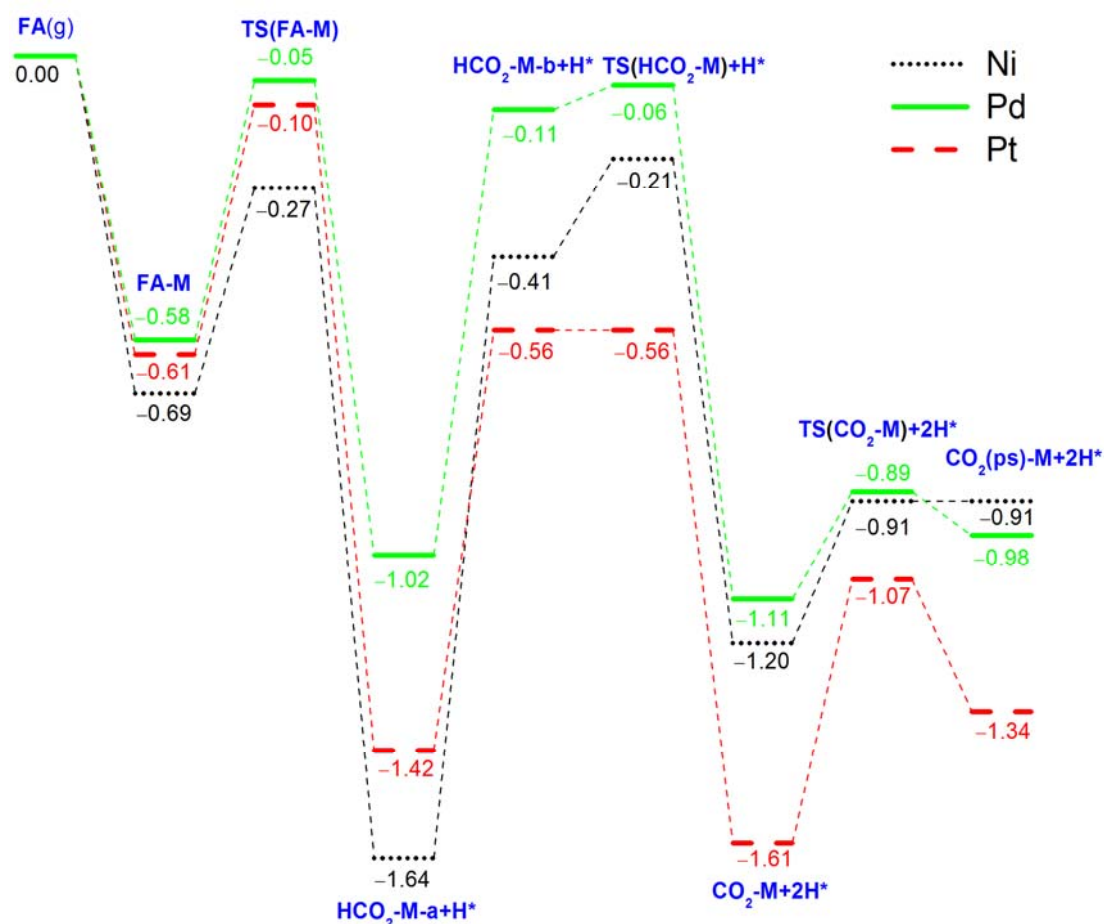


Figure 3.5 Potential energy of formic acid dehydrogenation on M(211) M = Ni, Pd, Pt (energies in eV)

3.3.6 Potential energy surface

Figure 3.5 shows the potential energy surface of FA adsorption and dissociation on the M(211) surfaces, and the reference is the total energy of formic acid in gas phase and the free slab (0.00 eV). The E_{ads} of FA on M(211) is -0.69 , -0.58 , -0.61 eV for M = Ni, Pd, Pt, respectively, and they are more or less close to each other.

The activation barriers of formic acid dissociation into surface formate and hydrogen are 0.42, 0.53, 0.51 eV for M = Ni, Pd, Pt, respectively. The total energies of the transition states are lower than the references in gas phase by -0.27 , -0.05 , -0.10 eV for M = Ni, Pd, Pt, respectively. The dissociation energy is -0.95 , -0.44 , -0.81 eV for M = Ni, Pd, Pt, respectively. This shows that FA dissociation into surface formate and H is both kinetically and thermodynamically most favorable on Ni(211), but least favorable on Pd(211), and this is due

to the much stronger adsorption energy of formate on Ni(211).

Table 3.1 Comparison of the energetic data of FA adsorption and dissociation on M(211) and M(111) (energies in eV)

	Ni(111)	Pd(111)	Pt(111)	Ni(211)	Pd(211)	Pt(211)
$E_{\text{ads}}(\text{HCO}_2\text{H})$	-0.36 ¹³ -0.43 ⁴²	-0.39 ¹³ -0.40 ¹⁴ -0.62 ¹⁶ -0.40 ¹⁷	-0.26 ¹³ -0.40/-0.34 ¹⁵ -0.39 ¹⁷ -0.42 ⁴³ -0.56 ⁵⁹	-0.69	-0.58	-0.61
$E_{\text{ads}}(\text{HCO}_2)$	-2.83 ¹³ -3.03 ⁴²	-2.37 ¹³ -0.68 ¹⁴ -2.71 ¹⁶ -2.52 ¹⁷	-2.32/-2.50 ¹⁵ -2.27 ¹⁷ -2.45 ³⁹	-3.49	-2.82	-3.04
$E_{\text{ads}}(\text{CO}_2)^{\text{a}}$	0.24 ¹³ 0.30 ⁵⁵ 0.19 ⁴²	0.23 ¹³ 0.30 ⁵⁵	0.24 1.01 ⁵⁵	-0.32	-0.13	-0.27
$E_{\text{ads}}(\text{H})$	-2.76 ¹³ -2.83 ⁴²	-2.78 ¹³ -2.92 ¹⁶ -2.89 ¹⁷	-2.78 ¹⁷	-2.74	-2.79	-2.97
$E_{\text{a}}(\text{HCO}_2\text{H} \rightarrow \text{HCO}_2 + \text{H})$	0.41 ¹³	0.58 ¹³ 0.21 ¹⁴ 1.00 ¹⁶ 0.68 ¹⁷	0.72 ¹³ 0.94/0.88 ¹⁵ 0.69 ¹⁷	0.42	0.53	0.51
$E_{\text{dis}}(\text{HCO}_2\text{H} \rightarrow \text{HCO}_2 + \text{H})$	-0.60 ¹³	-0.17 ¹³ 0.00 ¹⁶ -0.27 ¹⁷	0.03 ¹⁷	-0.95	-0.44	-0.81
$E_{\text{a}}(\text{HCO}_2 \rightarrow \text{CO}_2 + \text{H})^{\text{b}}$	1.03 ¹³	0.76 ¹³ 0.88 ¹⁶ 1.59 ¹⁷	1.23 ¹³ 1.56/1.16 ¹⁵ 1.88 ¹⁷	1.43	0.96	0.86
$E_{\text{dis}}(\text{HCO}_2 \rightarrow \text{CO}_2 + \text{H})$	0.36 ¹³	-0.43 ¹³ -0.29 ¹⁶ -0.45 ¹⁷	-0.43 ¹⁷ -0.31/-0.63 ¹⁵	0.44	-0.09	-0.19
super cell	(3×3) ¹³ (3×3) ⁴² (2×2) ⁵⁵	(3×3) ¹³ (3×3) ¹⁴ (3×3) ¹⁶ (3×3) ¹⁷ (2×2) ⁵⁵	(2×4) ¹³ (3×3/2×2) ¹⁵ (3×3) ¹⁷ (3×2√3) ⁴³ (2×2) ⁵⁵	(1×3)	(1×4)	(1×4)

(a) Chemisorption energy; (b) The effective barrier

For the step of formate dissociation, Ni(211) has the highest effective barrier of 1.43 eV and is endothermic by 0.44 eV. On Pd(211) and Pt(211), however, the effective barrier for formate dissociation is 0.96 and 0.86 eV, respectively, and the dissociation is exothermic by 0.09 and 0.19 eV, respectively. This shows that formate dissociation into surface CO₂ and H is both kinetically and thermodynamically less favorable on Ni(211), but more favorable on Pd(211) and Pt(211). Since formate dissociation is the rate-determining step on the basis of the effective barrier, Pd(211) and Pt(211) can dissociate FA more easily than Ni(211).

For CO₂ adsorption and desorption, Ni(211) has the strongest chemisorption (−0.32 eV), followed by Pt(211) (−0.27 eV) and Pd(211) (−0.13 eV). The desorption barrier is 0.29 eV on Ni(211), 0.22 eV on Pd(211) and 0.54 eV on Pt(211).

3.4 Conclusions

Spin-polarized plane-wave based periodic density functional theory calculations have been performed to study formic acid adsorption and decomposition on M(211) into CO₂ and hydrogen (HCOOH → CO₂ + 2H); and the computed results have been compared with those on M(111) for M = Ni, Pd and Pt from our own and other available data.

On M(211) and M(111), formic acid has the same adsorption configuration, in which the O (O=C) atom adsorbs atop on a first-layer metal atom and the H(O-H) atom points towards to two second layer neighboring surface metal atoms, but stronger adsorption has been found on M(211) than on M(111). For formic acid dissociation into surface formate and H, Ni(111) and Ni(211) as well as Pd(111) and Pd(211) have close dissociation barriers of formic acid, while Pt(211) has lower dissociation barrier than Pt(111).

On M(211) and M(111), formate has the same bidentate bridging adsorption configuration, but the calculated adsorption energies are stronger on M(211) than on M(111); and the rate-determining step is the dissociation of formate into surface CO₂ and H (HCOO → CO₂ + H) on both surfaces. The highest effective barrier is found on Ni(211) and Pt(111), and the lowest effective barrier is found on Pt(211) and Pd(111).

It is found that M(211) has thermodynamically favorable CO₂ chemisorption with negative adsorption energies, while M(111) has thermodynamically unfavorable CO₂ adsorption with positive adsorption energies. This difference is due to the nature of the metal atoms on the more open (100) step of M(211) and on the flat M(111) surface, as well as the transferred charge from surface to the adsorbed CO₂.

3.5 References

- (1) Loges, B.; Boddien, A.; Gärtner, F.; Junge, H.; Beller, M. *Top. Catal.* **2010**, *53*, 902–914.
- (2) Wang, J. Y.; Zhang, H. X.; Jiang, K.; Cai, W. B. *J. Am. Chem. Soc.* **2011**, *133*, 14876–14879.
- (3) Armaroli, N.; Balzani, V. *Angew. Chem. Int. Ed.* **2007**, *46*, 52–66.
- (4) Schlögl, L.; Züttel, A. *Nature* **2001**, *414*, 353–358.

- (5) Grasemann, M.; Laurenczy, G. *Energy Environ. Sci.* **2012**, *5*, 8171–8181.
- (6) Boddien, A.; Mellmann, D.; Gärtner, F.; Jackstell, R.; Junge, H.; Dyson, P. J.; Laurenczy, G.; Ludwig, R.; Beller, M. *Science* **2011**, *333*, 1733–1736.
- (7) Tedsree, K.; Li, T.; Jones, S.; Chan, C. W. A.; Yu, K. M. K.; Bagot, P. A. J.; Marquis, E. A.; Smith, G. D. W.; Tsang, S. C. E. *Nat. Nanotechnol.* **2011**, *6*, 302–307.
- (8) Kang, Y.; Qi, L.; Li, M.; Diaz, R. E.; Su, D.; Adzic, R. R.; Stach, E.; Li, J.; Murray, C. B. *ACS Nano* **2012**, *6*, 2818–2825.
- (9) Gu, X.; Lu, Z. H.; Jiang, H. L.; Akita, T.; Xu, Q. *J. Am. Chem. Soc.* **2011**, *133*, 11822–11825.
- (10) Bi, Q. Y.; Du, X. L.; Liu, Y. M.; Cao, Y.; He, H. Y.; Fan, K. N. *J. Am. Chem. Soc.* **2012**, *134*, 8926–8933.
- (11) Luo, Q.; Beller, M.; Jiao, H., Hydrogen Generation from Formic Acid – Computational Aspect *submitted under review*
- (12) Cramer, C. J.; Truhlar, D. G. *Phys. Chem. Chem. Phys.* **2009**, *11*, 10757–10816.
- (13) Luo, Q.; Feng, G.; Beller, M.; Jiao, H. *J. Phys. Chem. C* **2012**, *116*, 4149–4156.
- (14) Zhou, S.; Qian, C.; Chen, X. *Catal. Lett.* **2011**, *141*, 726–734.
- (15) Gao, W.; Keith, J. A.; Anton, J.; Jacob, T. *Dalton Trans.* **2010**, *39*, 8450–8456.
- (16) Zhang, R.; Liu, H.; Wang, B.; Ling, L. *J. Phys. Chem. C* **2012**, *116*, 22266–22280.
- (17) Hu, C.; Ting, S. W.; Chan, K. Y.; Huang, W. *Int. J. Hydrogen Energy* **2012**, *37*, 15956–15965.
- (18) Li, S. J.; Zhou, X.; Tian, W. Q. *J. Phys. Chem. A* **2012**, *116*, 11745–11752.
- (19) Benggaard, H. S.; Nørskov, J. K.; Sehested, J.; Clausen, B. S.; Nielsen, L. P.; Molenbroek, A. M.; Rostrup-Nielsen, J. R. *J. Catal.* **2002**, *209*, 365–384.
- (20) Cao, D. B.; Li, Y. W.; Wang, J.; Jiao, H. *Surf. Sci.* **2009**, *603*, 2991–2998.
- (21) Karmazyn, A. D.; Fiorin, V.; Jenkins, S. J.; King, D. A. *Surf. Sci.* **2003**, *538*, 171–183.
- (22) Orita, H.; Itoh, N.; Inada, Y. *Surf. Sci.* **2004**, *571*, 161–172.
- (23) Orita, H.; Nakamura, I.; Fujitani, T. *J. Chem. Phys.* **2005**, *122*, 014703–9.
- (24) Hammer, B. *Faraday Discuss.* **1998**, *110*, 323–333.
- (25) Hammer, B. *J. Catal.* **2001**, *199*, 171–176.
- (26) Hong, S.; Rahman, T. S. *Phys. Rev. B* **2007**, *75*, 155405–10.
- (27) Hou, L. B.; Deng, H. Q.; Hu, W. Y. *Trans. Nonferrous Met. Soc. China* **2006**, *16*, 820–823.
- (28) Olsen, R. A.; Bădescu, S. C.; Ying, S. C.; Baerends, E. J. *J. Chem. Phys.* **2004**, *120*, 11852–11863.
- (29) Vehviläinen, T.; Salo, P.; Ala-Nissila, T.; Ying, S. C. *Phys. Rev. B* **2009**, *80*, 035403–7.
- (30) Kresse, G.; Hafner, J. *Phys. Rev. B* **1993**, *47*, 558–561.
- (31) Kresse, G.; Hafner, J. *Phys. Rev. B* **1994**, *49*, 14251–14269.
- (32) Kresse, G.; Furthmüller, J. *Comput. Mater. Sci.* **1996**, *6*, 15–50.
- (33) Kresse, G.; Furthmüller, J. *Phys. Rev. B* **1996**, *54*, 11169–11186.

- (34) Perdew, J. P.; Bruke, K.; Ernzerhof, M. *Phys. Rev. Lett.* **1996**, *77*, 3865–3868.
- (35) Blöchl, P. E. *Phys. Rev. B* **1994**, *50*, 17953–17979.
- (36) Methfessel, M.; Paxton, A. T. *Phys. Rev. B* **1989**, *40*, 3616–3621.
- (37) Monkhorst, M.; Pack, J. D. *Phys. Rev. B* **1976**, *13*, 5188–5192.
- (38) Christmann, K.; Schober, O.; Ertl, G.; Neumann, M. *J. Chem. Phys.* **1974**, *60*, 4528–4540.
- (39) Lide, D. R. ed., *CRC Handbook of Chemistry and Physics, 90th Edition (CD-ROM Version 2010)*, CRC Press/Taylor and Francis, Boca Raton, FL, New York, 2002.p12–15 to 18.
- (40) Yang, B.; Wang, D.; Gong, X. Q.; Hu, P. *Phys. Chem. Chem. Phys.* **2011**, *13*, 21146–21152.
- (41) Jónsson, H.; Mills, G.; Jacobsen, K. W. In *Classical and Quantum Dynamics in Condensed Phase Simulations*; Berne, B. J.; Ciccotti, D. F. Eds, World Scientific: Singapore, 1998; p385.
- (42) Peng, G.; Sibener, S. J.; Schatz, G. C.; Ceyer S. T.; Mavrikakis, M. *J. Phys. Chem. C* **2012**, *116*, 3001–3006.
- (43) Bakó, I.; Pálinkás, G. *Surf. Sci.* **2006**, *600*, 3809–3814.
- (44) Hartnig, C.; Grimminger, J.; Spohr, E. *J. Electroanal. Chem.* **2007**, *607*, 133–139.
- (45) Nakatsuji, H.; Yoshimoto, M.; Hada, M.; Domen, K.; Hirose, C. *Surf. Sci.* **1995**, *336*, 232–244.
- (46) Nakatsuji, H.; Yoshimoto, M.; Umemura, Y.; Takagi, S.; Hada, M. *J. Phys. Chem.* **1996**, *100*, 694–700.
- (47) Yoshimoto, M.; Takagi, S.; Umemura, Y.; Hada, M.; Nakatsuji, H. *J. Catal.* **1998**, *173*, 53–63.
- (48) Lintuluoto, M.; Nakatsuji, H.; Hada, M.; Kanai, H. *Surf. Sci.* **1999**, *429*, 133–142.
- (49) Persson, P.; Lunell, S.; Ojamae, L. *Int. J. Quantum. Chem.* **2002**, *89*, 172–180.
- (50) Ferrin, P.; Kandoi, S.; Nilekar, A. U.; Mavrikakis, M. *Surf. Sci.* **2012**, *606*, 679–689.
- (51) Andersin, J.; Honkala, K. *Surf. Sci.* **2010**, *604*, 762–769.
- (52) Watwe, R. M.; Cortright, R. D.; Nørskov, J. K.; Dumesic, J. A. *J. Phys. Chem. B* **2000**, *104*, 2299–2310.
- (53) Offermans, W. K.; Jansen, A. P. J.; Van Santen, R. A.; Novell-Leruth, G.; Ricart, J. M.; Pérez-Ramírez. *J. Phys. Chem. C* **2007**, *111*, 17551–17557.
- (54) Freund, H. J.; Roberts, M. W. *Surf. Sci. Rep.* **1996**, *25*, 225–273.
- (55) Wang, S. G.; Cao, D. B.; Liao, X.Y.; Huo, C. F.; Li, Y. W.; Wang, J.; Jiao, H. *J. Phys. Chem. C* **2007**, *111*, 16934–16940.
- (56) Wang, S. G.; Cao, D. B.; Li, Y. W.; Wang, J.; Jiao, H. *J. Phys. Chem. B* **2005**, *109*, 18956–18963.
- (57) Peng, G.; Sibener, S. J.; Schatz, G. C.; Mavrikakis, M. *Surf. Sci.* **2012**, *606*, 1050–1055.

(58) Tang, W.; Sanville, E.; Henkelman, G. *J. Phys.: Condens. Matter* **2009**, *21*, 084204–7.

(59) Saliccioli, M.; Edie, S. M.; Vlachos, D. G. *J. Phys. Chem. C* **2012**, *116*, 1873–1886.

4 Formic Acid Dehydrogenation on Molybdenum Carbide

4.1 Introduction

Selective and catalytic decomposition of formic acid (FA, HCO_2H) into H_2 and CO_2 is considered as one of the potential chemical processes to satisfy the increasing energy demand, especially in fuel cell, green and clean technologies.¹⁻³ For FA selective decomposition both heterogeneous⁴⁻⁷ and homogeneous⁸⁻¹² catalysts have been used. Recently, Flaherty *et al.*, studied FA decomposition on molybdenum carbide and found that C-modified Mo(110) and C-Mo(110) are up to 15 times more selective than pure Mo(110) for H_2 formation.¹³ Koós and Solymosi reported that the highly stable molybdenum carbide (Mo_2C) catalyst prepared from the reaction of MoO_3 with a multiwall carbon nanotube and carbon Norit can selectively decompose FA into CO-free H_2 at 373-473 K.¹⁴ Cui *et al.*, reported that Pd catalysts supported on Mo_2C which is supported on multiwall carbon nanotube has much higher electrocatalytic activity and stability for FA electrooxidation than only Mo_2C catalyst supported on multiwall carbon nanotubes and only Pd catalysts supported on Mo_2C , and they concluded that Mo_2C is not only a support but also a co-catalyst.¹⁵ In addition, Mo_2C is active for hydrogenation and dehydrogenation,¹⁶ as well as for low temperature water-gas shift (WGS) reaction^{17,18} Transition metal carbides which have the added benefits of lower cost with respect to the Pt group metals, like W_2C and MoC_2 have been found to have Pt-like reactivity.^{19,20}

Theoretically, molybdenum carbides have been used to study various reactions. The hydrogenolysis mechanisms of thiophene²¹ and indole^{22,23} on clean $\beta\text{-Mo}_2\text{C}$ have been studied systematically. The chemisorption and decomposition of small molecules²⁴⁻²⁹ such as nitrogenous compounds, aromatic hydrocarbons and CO_2 were examined on both $\alpha\text{-Mo}_2\text{C}$ and $\beta\text{-Mo}_2\text{C}$ phases. Theoretical studies of the chemical properties of methanol,³⁰ methyl iodide,³¹ CO and the promoting effect of potassium on $\beta\text{-Mo}_2\text{C}$ were reported systematically by Pistonesi *et al.*,³² based on their surface experiments; and they found that the incorporation of potassium atoms enhances the dissociation ability of the C-I and C-O bonds in CH_3I and CH_3OH , while blocks the dissociation of CO. Tominaga and Nagai built a schematic potential energy surface for WGS reaction and concluded that CO_2 formation from CO oxidation by surface O is the rate-limiting step.³³ The mechanism of CO hydrogenation and the promoter effect of cobalt have also been systematically reported recently.³⁴ Liu *et al.*, also calculated WGS mechanism and emphasized the importance of oxygen on the Mo_2C surface.³⁵ In order to study the intrinsic WGS activities of Mo_2C , Schweitzer *et al.*, loaded Pt on Mo_2C and found Mo_2C to play the role of both support and catalyst.³⁶ Shi *et al.*,³⁷ and Han *et al.*,³⁸ calculated the surface energies of low miller index surfaces of hexagonal Mo_2C to compare their stabilities and concluded that the (011) facet was the most stable surface. The elementary steps of syngas reaction have been systematically studied by using ab initio

thermodynamics method by Andrew *et al.* and Mo_2C was proved to have similar catalytic properties with noble metals.³⁹ Recently, Zheng *et al.*, reported H_2 production from ammonia decomposition catalyzed by molybdenum carbide both experimentally and theoretically.⁴⁰

We carried out spin-polarized periodic density functional theory computations to study the adsorption and dissociation of FA on the $\text{Mo}_2\text{C}(101)$ surface. Our goal is the understanding into the adsorption configurations of FA and its dissociation intermediates on the $\text{Mo}_2\text{C}(101)$ surface as well as the dissociation paths. These results are compared with those on the Pt group metals, e.g.; Pd(111),⁴¹⁻⁴⁴ Pt(111),^{43,45,46} and Ir(100),⁴⁷ from recent computational studies.

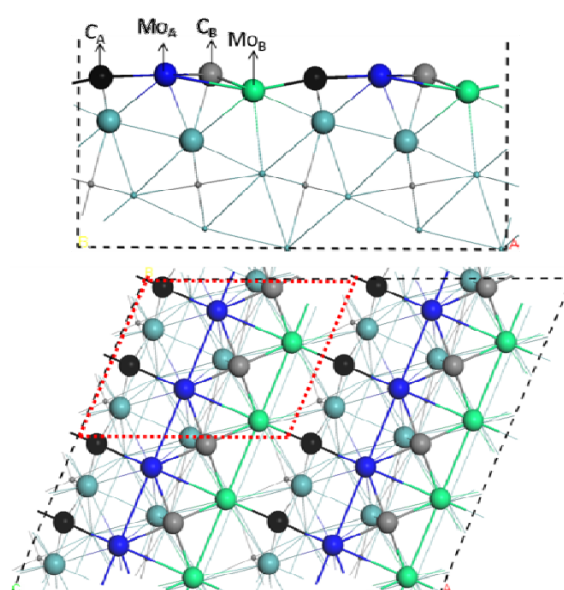


Figure 4.1 Side and top views of the $\text{Mo}_2\text{C}(101)$ surface

4.2 Computational details

4.2.1 Model

Mo_2C mainly has two crystalline structures, the orthorhombic α - Mo_2C phase⁴⁸ and the hexagonal β - Mo_2C phase.^{49,50} In our work, we used the β -hexagonal Mo_2C phase with an eclipsed configuration as unit cell.^{51,52} The calculated lattice parameter of the cell is $2a = 6.075 \text{ \AA}$, $2b = 6.069 \text{ \AA}$ and $c = 4.722 \text{ \AA}$, in good agreement with the experiment: $a = b = 3.011 \text{ \AA}$ and $c = 4.771 \text{ \AA}$.⁵³ Among all the surfaces of β - Mo_2C , the (101) surface was reported to be most stable,^{37,51-55} and there are two types of C atoms and two types of Mo atoms on the exposed surface (Figure 4.1). For describing this surface atoms easily, the 4-coordinated (two surface Mo atoms and two bulky phase Mo atoms) C atom is marked as C_A , the 5-coordinated (four surface Mo atoms and one bulky phase Mo atom) C atom is denoted as C_B . The 10-coordinated (three surface Mo atoms, three surface C atoms and four bulky phase Mo atoms) and 11-coordinated (three surface Mo atoms, three surface C atoms and five bulky phase Mo atoms) Mo atoms are notated as Mo_A and Mo_B , respectively. The total supercell

contains a $\text{Mo}_{32}\text{C}_{64}$ unit within a volume of $15.40 \times 12.11 \times 17.96 \text{ \AA}$, and the exposed surface has 16 Mo atoms and 16 C atoms. In addition, a smaller surface model containing 4 exposed Mo atoms and 4 exposed C atoms within the red region of the surface was also employed to study coverage effect, which is defined as the exposed surface Mo atoms, e.g.; 1/16 ML for the large model and 1/4 ML for the small model.

4.2.2 Method

All calculations were done using the plane-wave spin-polarized periodic density functional method (DFT) in the Vienna *ab initio* simulation package (VASP).⁵⁶⁻⁵⁹ The electron ion interaction was described with the projector augmented wave (PAW) method.⁶⁰ The electron exchange and correlation energy was treated within the generalized gradient approximation in the Perdew-Burke-Ernzerhof formalism (GGA-PBE).⁶¹ For Mo, the core 4p states were also taken into valence region and totally 12 valence electrons were included. The Kohn-Sham one-electron states were expanded in a plane wave with an energy cutoff 400 eV, and the Methfessel-Paxton scheme was used under the electron smearing of $\sigma = 0.1 \text{ eV}$.⁶² The vacuum zone was set up to 12 \AA in the z direction to separate the slabs. The geometry optimization was done when force becomes smaller than 0.02 eV/\AA and the energy difference was lower than 10^{-5} eV . For bulk optimization, the lattice parameters were obtained by minimizing the total energy of the unit cell using a conjugated-gradient algorithm to relax the ions and a $5 \times 5 \times 5$ Monkhorst-Pack k-point grid was used for sampling the Brillouin zone.⁶³ The first Brillouin zone was sampled with $3 \times 3 \times 1$ k-point grid for investigating the surfaces (1/16 and 1/4 ML). The nudged elastic band (NEB) method was used to locate the minimum energy path.⁶⁴ The computed vibrational frequencies were used to characterize a minimum state without imaginary frequencies or an authentic transition state with only one imaginary frequency.

The adsorption energy is defined as in Equation, $E_{\text{ads}} = E_{\text{A/slab}} - [E_{\text{slab}} + E_{\text{A}}]$; where $E_{\text{A/slab}}$ is the total energy of the slab with adsorbates A, E_{slab} is the total energy of the bare slab, and E_{A} is the total energy of free adsorbate A in gas phase; and the more negative the E_{ads} , the stronger the adsorption. The activation energy is defined in Equation, $E_{\text{a}} = E_{\text{TS}} - E_{\text{IS}}$; and the reaction energy is defined as in Equation, $E_{\text{r}} = E_{\text{FS}} - E_{\text{IS}}$; where E_{IS} , E_{FS} and E_{TS} represent the total energy of initial, final and transition states.

4.3 Results and Discussion

4.3.1 Adsorption of the surface intermediates

For each adsorbate, only adsorption site and geometries with the largest adsorption energy are included while many more have been evaluated. Table 4.1 lists the adsorption energies of the most stable adsorption configurations on the $\text{Mo}_2\text{C}(101)$ surface at 1/16 ML and 1/4 ML. The rather small differences in adsorption energies of these intermediates show that 1/16 ML is quite larger enough for our analysis and the coverage effects can be ruled out. Figure 4.2 shows the most stable adsorption configurations of these intermediates (HCO_2H , CO_2 , CO ,

H₂O, HCO₂, CO₂H, CHO, OH, O and H) at 1/16 ML; and those at 1/4 ML are given in [Appendix Figure A11](#). Our discussion and comparison are mainly based on the data at 1/16 ML, if it is not noted otherwise.

Two FA adsorption configurations on the Mo₂C(101) surface are located, the flat one HCO₂H-flat (**1**) and the perpendicular one HCO₂H-O/OH-down (**2**). As shown in [Figure 4.2](#), HCO₂H-flat (**1**) has its O=C-O group chelating with a surface Mo_A atom, and the O atom of the OH group bonding to a neighbouring surface Mo_A atom, and the adsorption energy is -1.12 eV, indicating a strong adsorption. In HCO₂H-O/OH-down (**2**), FA stands over the surface by the O atom of the O=C group interacting with one surface Mo_A atom and the H atom of the OH group pointing towards one surface C_A atom; and the adsorption energy is -1.06 eV, which is only 0.06 eV less stable than that of HCO₂H-flat (**1**). This indicates that both adsorption configurations are isoenergetic and might coexist at this coverage.

Table 4.1 The computed adsorption energies (E_{ads} , eV) for the most stable adsorption configurations of the intermediates involved in FA dissociation at 1/16 and 1/4 ML

Species	1/16 ML	1/4 ML
HCO ₂ H-flat (1)	-1.12	-1.16
HCO ₂ H-O/OH-down (2)	-1.06	-1.06
CO ₂ -OM/CC (3)	-0.92	-0.87
CO ₂ -OM/OM (4)	-0.81	-0.81
CO-flat (5)	-1.61	-1.32
CO-C-down (6)	-1.58	-1.56
H ₂ O (7)	-0.66	-0.63
HCO ₂ -O/O-down (8)	-4.04	-4.10
HCO ₂ -flat (9)	-3.44	-3.54
HCO ₂ -O/H-down (10)	-2.88	-2.76
CO ₂ H-OM/CC (11)	-2.92	-2.91
CO ₂ H-OM/CM (12)	-2.85	-2.94
CHO (13)	-3.22	-3.21
OH (14)	-4.15	-4.16
O (15)	-6.59	-6.58
H (16)	-2.79	-2.76

CO₂ has two energetically very close adsorption configurations, CO₂-OM/CC (**3**) and

CO₂-OM/OM (4). In CO₂-OM/CC (3), the O atoms bond to surface Mo_A and Mo_B atoms, and the C atom bonds to a surface C_A atom, and the OCO angle is 128.04°; and the adsorption energy is -0.92 eV. In CO₂-OM/OM (4), the O atoms bond to surface Mo_A atoms and the C atom bridges two Mo_A atoms, and the OCO angle is 134.96°; and the adsorption energy is -0.81 eV. In addition, the physisorption is also located and the adsorption energy is only -0.19 eV, much weaker than the chemisorption.

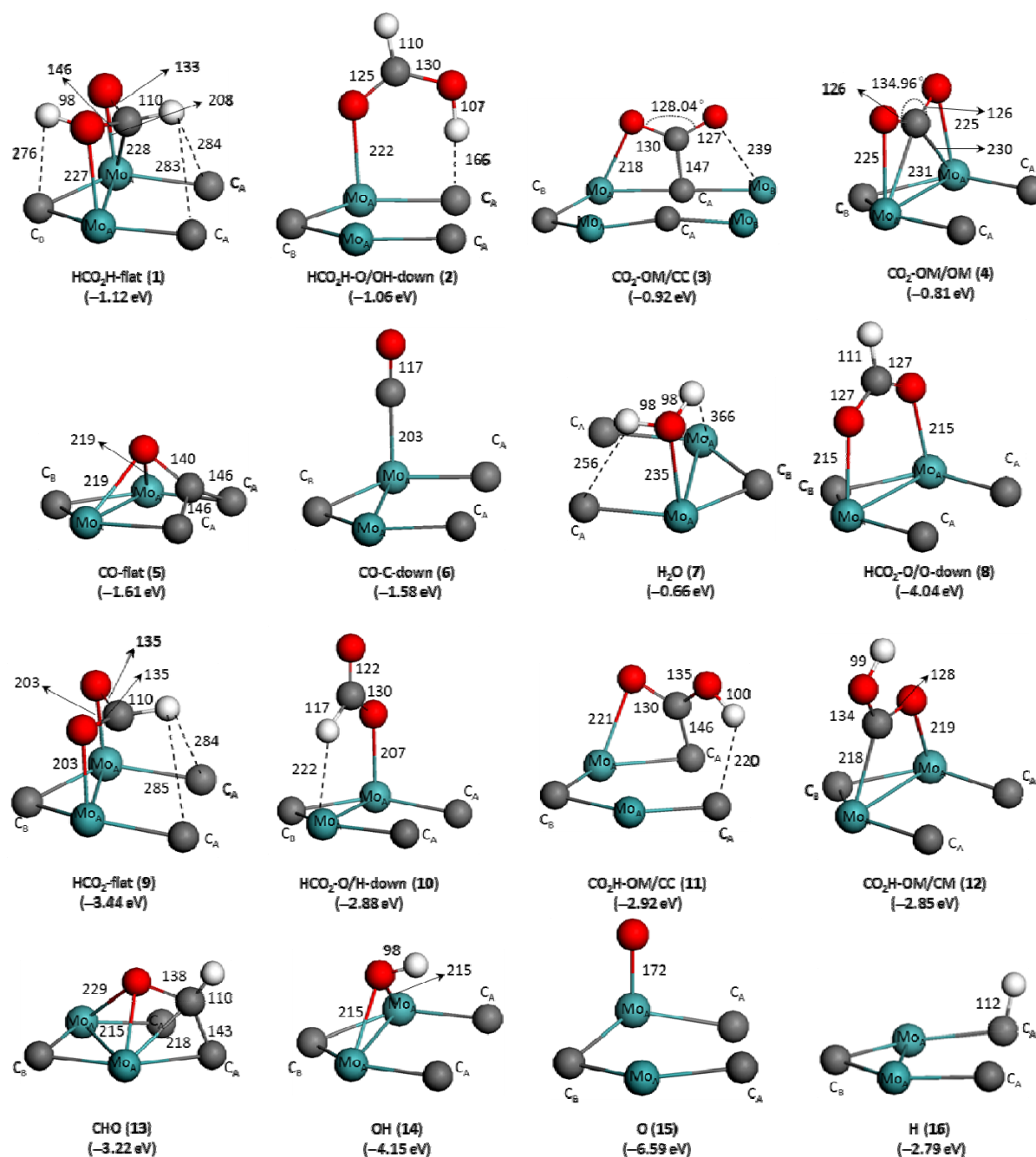


Figure 4.2 The most stable adsorption configurations of intermediates involved in FA decomposition (bond distances in pm and energies in eV)

CO has two energetically almost equivalent configurations, CO-flat (**5**) and CO-C-down (**6**). In CO-flat (**5**), the O atom bonds to two surface Mo_A atoms, and the C atom bonds to two surface C_A atoms; and the adsorption energy is -1.61 eV. In CO-C-down (**6**), the C atom adsorbs vertically atop on one surface Mo_A atom, and the adsorption energy is -1.58 eV.

H_2O (**7**) prefers the O atom bonding to surface Mo_A atom, and its H atoms pointing towards a neighbouring C_A and a neighbouring Mo_A atom, and the adsorption energy is -0.66 eV

The most stable adsorption configurations of formate are $\text{HCO}_2\text{-O/O-down}$ (**8**), $\text{HCO}_2\text{-flat}$ (**9**) and $\text{HCO}_2\text{-O/H-down}$ (**10**). In $\text{HCO}_2\text{-O/O-down}$ (**8**), HCO_2 stands perpendicular to the surface and the O atoms bridge two surface Mo_A atoms with O- Mo_A distances of 215 pm; and the adsorption energy is -4.04 eV. In $\text{HCO}_2\text{-flat}$ (**9**), HCO_2 covers the surface and its two O atoms bond directly to two Mo_A atoms with the Mo-O distances of 203 pm; and the adsorption energy is -3.44 eV. In $\text{HCO}_2\text{-O/H-down}$ (**10**), one of its O atoms bonds to a surface Mo_A atom with the O- Mo_A distance of 207 pm and the H atom points towards the neighbouring Mo_A with the H- Mo_A distance of 222 pm; and the adsorption energy is -2.88 eV. These show that $\text{HCO}_2\text{-O/O-down}$ (**8**) is the most stable adsorption configuration.

Table 4.2 The computed energy barriers (E_a , eV) and reaction energies (E_r , eV) for the elementary steps of FA dissociation

reaction	E_a/E_r	
	1/16 ML	1/4 ML
$\text{HCO}_2\text{H-flat/H+HCO}_2$ (a)	0.93/-1.12	0.95/-1.11
$\text{HCO}_2\text{H-flat/H+CO}_2\text{H}$ (b)	1.47/-0.23	1.49/-0.16
$\text{HCO}_2\text{H-flat/CHO+CO}$ (c)	0.48/-1.16	0.49/-1.12
$\text{HCO}_2\text{H-O/OH-down/H+HCO}_2$ (d)	0.02/-1.18	0.01/-1.21
$\text{HCO}_2\text{-O/O-down/O+CHO}$ (e)	2.27/-0.02	2.27/-0.04
$\text{HCO}_2\text{-flat/H+CO}_2$ (f)	1.01/-0.26	1.17/-0.07
$\text{HCO}_2\text{-O/H-down/H+CO}_2$ (g)	0.54/-0.82	0.54/-0.85
CHO/H+CO (h)	1.46/-0.02	1.53/0.05
$\text{H+OH/H}_2\text{O}$ (i)	1.36/0.94	1.31/0.95
$\text{CO+OH/CO}_2\text{H-OM/CM}$ (j)	1.40/1.02	1.27/0.89
$\text{CO}_2\text{H-OM/CC/H+CO}_2$ (k)	0.23/-0.55	0.27/-0.47
$\text{CO}_2\text{/desorption}$ (l)	0.92	0.87

Carboxyl (CO_2H) has two energetically very close adsorption configurations, $\text{CO}_2\text{H-OM/CC}$ (**11**) and $\text{CO}_2\text{H-OM/CM}$ (**12**). In $\text{CO}_2\text{H-OM/CC}$ (**11**), the O atom of the O=C group interacts with one surface Mo_A atom and the C atom binds to one neighbouring surface C_A atom as well as the H atom points to one surface C_A atom (the configuration with the H atom opposite to the surface C_A atom is 0.04 eV less stable, [Appendix Figure A12](#)); and the adsorption energy is -2.92 eV. In $\text{CO}_2\text{H-OM/CM}$ (**12**), the O=C group bridges two surface Mo_A atoms and the H atom is opposite to the surface (the configuration with the H atom pointing to the surface is 0.04 eV less stable, [Appendix Figure A12](#)) and the adsorption energy is -2.85 eV. These indicate their possible co-existence.

Formyl (CHO , **13**) prefers the O atom bridging two neighbouring surface Mo_A atoms and the C atom bridging one Mo_A and one surface C_A ; and the adsorption energy is -3.22 eV. Hydroxyl (OH , **14**) has its O atom bridging two neighbouring surface Mo_A atoms, and the adsorption energy is -4.15 eV. Atomic oxygen (O , **15**) has atop adsorption on one surface Mo_A atom, and the adsorption energy is -6.59 eV; and atomic hydrogen (H , **16**) has atop adsorption on one surface C_A atom and the adsorption energy is -2.79 eV.

4.3.2 Dissociation path

On the basis of the above discussed adsorption configurations and energies, we analyzed FA dissociation on the surface starting from the two most stable $\text{HCO}_2\text{H-flat}$ (**1**) and $\text{HCO}_2\text{H-O/OH-down}$ (**2**). The adsorption configuration of the transition states are shown in [Figure 4.3](#); and the energetic parameters are given in [Table 4.2](#).

(a) FA Dissociation: Since FA has two adsorption configurations in close energy; we studied both dissociation routes accordingly. Starting from $\text{HCO}_2\text{H-flat}$ (**1**), FA can dissociate either to HCO_2+H (formate) or alternatively to $\text{CO}_2\text{H}+\text{H}$ (carboxyl) or to $\text{CHO}+\text{OH}$ (formyl+hydroxyl). For HCO_2 formation, the transition state **TS**($\text{HCO}_2\text{H-flat}/\text{HCO}_2+\text{H}$) (**a**) is located, and the breaking O-H distance is 137 pm and the forming $\text{C}_B\text{-H}$ distance is also 137 pm. The energy barrier is 0.93 eV and the reaction is exothermic by 1.12 eV. For CO_2H formation, the transition state **TS**($\text{HCO}_2\text{H-flat}/\text{H}+\text{CO}_2\text{H}$) (**b**) is located; and the breaking C-H distance is 149 pm and the forming $\text{C}_A\text{-H}$ distance is 137 pm. The energy barrier is 1.47 eV, which is 0.35 eV higher than the adsorption of FA (-1.12 eV); and the reaction is exothermic by 0.23 eV. For FA dissociation into $\text{CHO}+\text{OH}$, the transition state **TS**($\text{HCO}_2\text{H-flat}/\text{CHO}+\text{OH}$) (**c**) is located; and the breaking C-O distance is 210 pm (146 pm in $\text{HCO}_2\text{H-flat}$ (**1**)). The energy barrier is 0.48 eV and the reaction is exothermic by 1.16. It is clearly to see that starting from $\text{HCO}_2\text{H-flat}$ (**1**) FA prefers to dissociate into $\text{CHO}+\text{OH}$ rather than into HCO_2+H or $\text{CO}_2\text{H}+\text{H}$ both thermodynamically and kinetically. Starting from $\text{HCO}_2\text{H-O/OH-down}$ (**2**), FA can only dissociate into HCO_2+H because of its perpendicular adsorption configuration. In the transition state **TS**($\text{HCO}_2\text{H-O/OH-down}/\text{H}+\text{HCO}_2$) (**d**), the breaking O-H distance is elongated to 122 pm and the forming H- C_A bond is 140 pm (107 and 166 pm in $\text{HCO}_2\text{H-O/OH-down}$ (**2**), respectively); and the energy barrier is only 0.02 eV and the reaction energy is exothermic by

1.18 eV. This shows that FA dissociates spontaneously into HCO_2+H . Compared to the adsorption energy and the dissociation barriers of HCO_2H -flat (1), HCO_2H -O/OH-down (2) dissociation into HCO_2+H is much more favourable kinetically.

To show this preference more clearly, we calculated the FA adsorption at very high coverage (1/2 ML); and only HCO_2H -O/OH-down (2) adsorption configuration is possible, and the computed FA adsorption energy is -0.80 eV, which is lower than that of the first FA adsorption at 1/4 ML, indicating a significant lateral repulsive interaction of 0.26 eV. At such high coverage, HCO_2H -O/OH-down (2) dissociation into HCO_2+H is the only possible route.

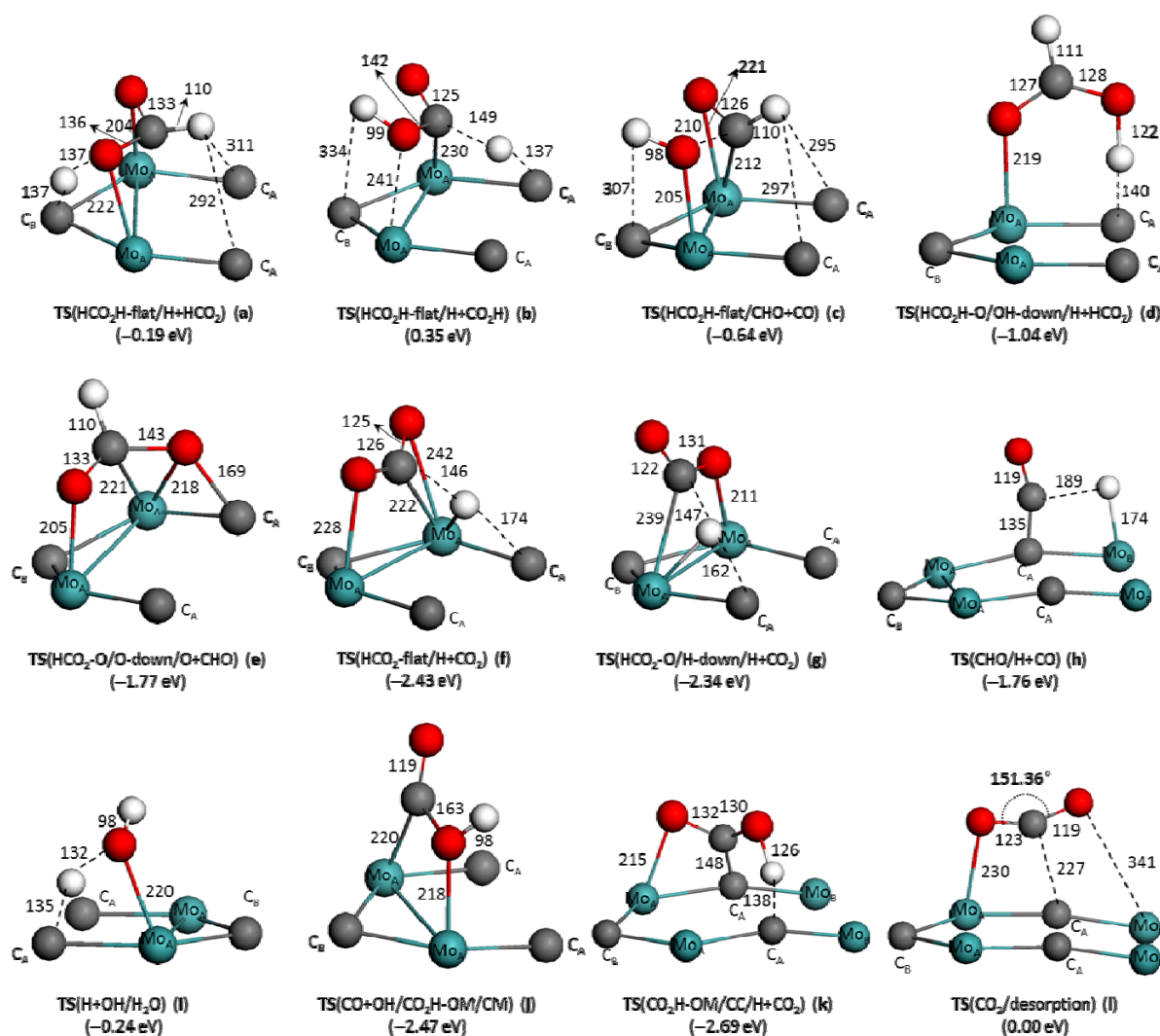


Figure 4.3 The transition state configurations involved in FA decomposition (bond distances in pm and energies in eV)

(b) HCO_2 dissociation: As the most favourable surface intermediate, formate dissociation into either $\text{O}+\text{CHO}$ or $\text{H}+\text{CO}_2$ was studied. For the $\text{O}+\text{CHO}$ route from $\text{HCO}_2\text{-O}/\text{O}\text{-down}$ (8), the transition state $\text{TS}(\text{HCO}_2\text{-O}/\text{O}\text{-down}/\text{O}+\text{CHO})$ (e) is located; the breaking C-O bond distance is elongated from 127 pm to 143 pm and the energy barrier is 2.27 eV and the

reaction is thermal neutral (-0.02 eV). For the CO_2+H route from $\text{HCO}_2\text{-O/O-down}$ (**8**), it is not possible for a direct C-H bond dissociation due to its perpendicular orientation, and the less stable adsorption configurations, $\text{HCO}_2\text{-flat}$ (**9**) and $\text{HCO}_2\text{-O/H-down}$ (**10**) from the dynamic bending were considered.⁶⁵⁻⁶⁹ Starting from $\text{HCO}_2\text{-flat}$ (**9**) into CO_2+H , the transition state $\text{TS}(\text{HCO}_2\text{-flat/H+CO}_2)$ (**f**) is located; where the breaking C-H distance is 146 pm and the forming $\text{C}_A\text{-H}$ distance is 174 pm. The energy barrier is 1.01 eV. Starting from $\text{HCO}_2\text{-O/H-down}$ (**10**) into CO_2+H , the transition state $\text{TS}(\text{HCO}_2\text{-O/H-down/H+CO}_2)$ (**g**) is located; where the breaking C-H distance is 147 pm and the forming $\text{C}_A\text{-H}$ distance is 162 pm. The energy barrier is 0.54 eV.

Starting from $\text{HCO}_2\text{-O/O-down}$ (**8**), the effective barrier via the transition state $\text{TS}(\text{HCO}_2\text{-flat/H+CO}_2)$ (**f**) is 1.61 eV; while the effective barrier via the transition state $\text{TS}(\text{HCO}_2\text{-O/H-down/H+CO}_2)$ (**g**) is 1.70 eV; and the reaction is endothermic by 0.34 eV. Compared with the high barrier (2.27 eV) of O+CHO formation, the formation of H+CO_2 via the dynamic bending $\text{HCO}_2\text{-flat}$ (**9**) configuration is more favourable kinetically.

(c) CHO dissociation as well as H_2O and CO_2 formation: As the most favourable route for CHO+OH formation from $\text{HCO}_2\text{H-flat}$ (**1**), we computed CHO (**13**) dissociation into CO+H , and the subsequent CO_2H formation from CO+OH as well as H_2O formation from H+OH . For CHO dissociation into CO+H , the transition state $\text{TS}(\text{CHO/H+CO})$ (**h**) is located, and the C-H distance is 189 pm; and the energy barrier is 1.46 eV and the reaction is almost thermal neutral (-0.02 eV).

Starting from the previously formed surface OH, the further reactions of CO+H into H_2O and CO_2H were calculated. For H_2O (**7**) formation from H+OH , the transition state $\text{TS}(\text{H+OH/H}_2\text{O})$ (**i**) is located, and the forming O-H distance is 132 pm and the breaking surface C-H distance is 135 pm; and the energy barrier is 1.36 eV and the reaction is endothermic by 0.94 eV, while the back reaction has lower energy barrier of 0.42 eV. Therefore, H_2O dissociation is more favourable than its formation.

For CO_2H formation from CO+OH , the transition state $\text{TS}(\text{CO+OH/CO}_2\text{H-OM/CM})$ (**j**) is located, and the forming C-O distance is 163 pm, and the energy barrier is 1.40 eV; and the reaction is endothermic by 1.02 eV; while the back reaction has lower energy barrier of 0.38 eV; these show that CO_2H dissociation instead of formation is more favourable. Nevertheless, we also calculated CO_2H dissociation into CO_2+H . It is to note that there are two adsorption configurations for CO_2H in very close energy, $\text{CO}_2\text{H-OM/CC}$ (**11**) and $\text{CO}_2\text{H-OM/CM}$ (**12**). Starting from the more stable $\text{CO}_2\text{H-OM/CC}$ (**11**), we located the transition state $\text{TS}(\text{CO}_2\text{H-OM/CC/H+CO}_2)$ (**k**), in which the breaking H-O distance is 126 pm and the forming H- C_A distance is 138 pm; and the energy barrier is 0.23 eV; and the reaction is exothermic by 0.55 eV. In addition, $\text{CO}_2\text{H-OM/CM}$ (**12**) ([Appendix Figure A12](#)) dissociates into CO_2+H is less favourable kinetically.

On the basis of the computed energy barriers and the reaction energies for CO₂H formation and dissociation, CO₂H dissociation into CO₂+H is kinetically more favourable, while CO₂H dissociation back to CO+OH is kinetically less favourable, but thermodynamically more favourable.

(d) CO₂ desorption: Since CO₂ has a strong adsorption on the surface, the corresponding desorption was computed. Starting from the most stable adsorption configuration (CO₂-OM/CC (**3**)), the transition state **TS**(CO₂/desorption) (**I**) was located; in which the distance of O-Mo_A and C-C_A is 230 and 227 pm, respectively; and the OCO angle is 151.36°, which is larger than that (128.04°) in CO₂-OM/CC (**3**); and the desorption energy is endothermic by 0.92 eV, and this is also the CO₂ adsorption energy.

The computed adsorption energies of the intermediates involved in FA dissociation in [Table 4.1](#) show negligible differences between 16/ML and 1/4 ML apart from the flat adsorbed CO (**5**), which has a difference of 0.29 eV. Detailed analysis into this difference shows the strong reconstruction of the surface structure for CO (**5**) at 1/4 ML and no such significant surface reconstructions can be found for other intermediates. Similar coverage effects have also been found for the energy barriers and reaction energies for the elemental steps for FA dissociation ([Table 4.2](#)). All these show that our surface models are large enough for computing FA dissociation.

The transition states involved in FA dissociation at 1/4 ML are shown in [Appendix Figure A13](#).

4.3.3 Potential Energy Surface

On the basis of the computed energetic parameters for the elementary steps, we have mapped the potential energy surface for FA adsorption and decomposition on the Mo₂C(101) at 1/16 ML ([Figure 4.4](#)). FA has two adsorption configurations close in energy, parallel to the surface (HCO₂H-flat (**1**, $E_{\text{ads}} = -1.12$ eV)) and perpendicular to the surface (HCO₂H-O/OH-down (**2**, $E_{\text{ads}} = -1.06$ eV)). However, they have very different dissociation routes. Starting from the more stable configuration (**1**), a potential route follows its dissociation (**c**) forming surface CHO and OH (CHO+OH). Other dissociation routes towards surface formate (HCO₂) (**a**) and carboxyl (CO₂H) (**b**) have much higher barriers and thus kinetically much less favored. Considering (**2**), which is a less stable configuration than (**1**), the formation of surface formate (**8**) proceeds almost barrier-less following the dissociation route (**d**). We shall revisit this result when discussing the selectivity.

Continuing the reaction pathway starting at (**8**), direct C-H bond cleavage is not possible. Also the dissociation of (**8**) into surface CHO+O is not competitive, as its barrier is 2.27 eV. Instead, dynamic bending involving the adsorption configurations HCO₂-falt (**9**) and HCO₂-O/H-down (**10**) become likely. These processes need to overcome an effective barrier of 1.70 eV, and the surface CO₂ formation is endothermic by 0.34 eV (or 1.26 eV to gaseous

CO₂). However, the overall reaction pathway remains below the potential energy of the initial state (FA in gas phase ($E \equiv 0.00$ eV)).

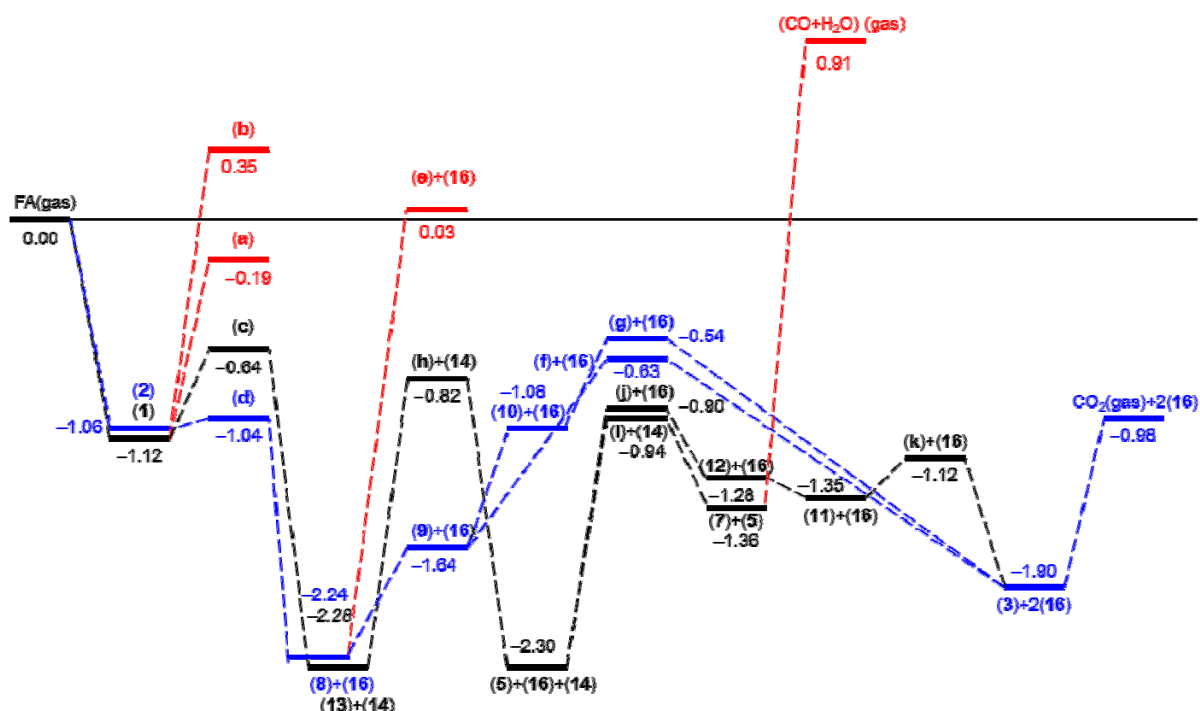


Figure 4.4 The potential energy surface for FA dissociation at 1/16 ML starting from gaseous FA (energies in eV)

A potential competitive reaction pathway may start at the surface CHO (**13**). The dissociation of (**13**) into surface CO+H is associated with a barrier of 1.46 eV, and the reaction is nearly thermal neutral. The subsequent elementary steps of CO and OH to form surface carboxyl (**12**) as well as H+OH to form surface H₂O (**7**) need high barriers (1.40 eV and 1.34 eV, respectively) and are endothermic by 1.02 and 0.94 eV, respectively. These show that (**12**) and (**7**) are metal-stable intermediates and they prefer the dissociation into surface CO (**5**) and OH. However, desorption of CO and H₂O is highly endothermic and would thus lead to poisoning of the active sites. Since the elementary steps are equilibrated, this part of the reaction may also proceed in the reverse direction.

With a view to the high selectivity the catalyst provides for the overall decomposition of FA towards CO₂ and H₂, we should keep in mind that the entire potential energy surface remains below the potential energy of FA; all elementary steps are equilibrated. Additionally, we may formulate the conservation of the number of active sites by the sum of all intermediates sticking to the surface, which is constant. Due to the thermodynamic equilibrium, the equation is cancelling down to $1 = \theta_{\text{HCO}_2+\text{H}} + \theta_{\text{CHO}+\text{OH}}$, where θ is the coverage. Although the reaction pathway via (**13**) also lead to CO₂ formation, the probability is very low. Reason for this observation is the barrier of the elementary step (**c**), which is higher and requires a $\sim 10^6$ times

longer lifetime of the transition state than that of (d). Finally, the overall reaction rate for FA decomposition via the HCO₂ pathway was found to be 2300 times faster than that following the HCO pathway (Appendix Text A1).

Figure 4.3 illustrates the potential energy surface and highlights the most favourable route of the decomposition of FA via formate towards CO₂+2H. This agrees with the experimental findings of CO-free H₂.¹⁴

The corresponding potential energy surface for FA dissociation at 1/4 ML is shown in Appendix Figure A14

Table 4.3 Comparison of the adsorption energies (E_{ads} , eV), dissociation barriers (E_{a} , eV) and dissociation energies (E_{r} , eV) of FA on β -M₂C(101), Pd(111) and Pt(111) as well as on Ir(100) surfaces

Mo ₂ C(101)	Pd(111)	Pt(111)	Ir(100)
E_{ads} (HCO ₂ H)			
-1.12; -1.06	-0.39 ⁴¹ ; -0.62 ⁴² ; -0.40 ⁴³ ; -0.40 ⁴⁴	-0.39 ⁴³ ; -0.40/-0.34 ⁴⁵ ; -0.26 ⁴⁶	-0.63 ⁴⁷
E_{ads} (HCO ₂)			
	-2.37 ⁴¹ ; -2.71 ⁴² ; -2.52 ⁴³ ; -2.49 ⁴⁴	-2.27 ⁴³ ; -2.32/-2.50 ⁴⁵	-3.66 ⁴⁷
E_{ads} (CO ₂) ^a			
-0.92	0.23 ⁴¹		
E_{ads} (H)			
-2.79	-2.78 ⁴¹ ; -2.92 ⁴² ; -2.89 ⁴³	-2.78 ⁴³	-3.01 ⁴⁷
E_{a} (HCO ₂ H → HCO ₂ + H)			
0.02	0.58 ⁴¹ ; 1.00 ⁴² ; 0.68 ⁴³ ; 0.49 ⁴⁴	0.72 ⁴⁶ ; 0.94/0.88 ⁴⁵ ; 0.69 ⁴³	
E_{r} (HCO ₂ H → HCO ₂ + H)			
-1.18	-0.17 ⁴¹ ; 0.00 ⁴² ; -0.27 ⁴³ ; -0.09 ⁴⁴	0.03 ⁴³	0.18 ⁴⁷
E_{a} (HCO ₂ → CO ₂ + H) ^b			
1.61	0.76 ⁴¹ ; 0.88 ⁴² ; 1.59 ⁴³ ; 0.77 ⁴⁴	1.23 ⁴⁶ ; 1.56/1.16 ⁴⁵ ; 1.88 ⁴³	0.87 ⁴⁷
E_{r} (HCO ₂ → CO ₂ + H)			
0.34	-0.43 ⁴¹ ; -0.29 ⁴² ; -0.45 ⁴³ ; -0.22 ⁴⁴	-0.43 ⁴³ ; -0.31/-0.63 ⁴⁵	-0.06 ⁴⁷
super cell			
(4×4)	(3×3) ⁴¹ ; (3×3) ⁴² ; (3×3) ⁴³ ; (3×3) ⁴⁴	(2×4) ⁴⁶ ; (3×3/2×2) ⁴⁵ ; (3×3) ⁴³	(3×3) ⁴⁷

(a) chemisorption state energy; (b) effective energy barrier

4.3.4 Comparison with Pd(111), Pt(111) and Ir(100)

Since molybdenum carbide has been proposed to have the catalytic activity of the Pt group metals, we compared the energetic parameters of FA adsorption and dissociation on Mo₂C(101), Pt(111), Pd(111) and Ir(100). Since the formate route is the more preferable

mechanism, it is much easy for the general comparison, and these data are summarized in [Table 4.3](#).

As shown in [Table 4.3](#), FA has much stronger adsorption energy on Mo₂C(101) than on Pd(111), Pt(111) and Ir(100); all these surfaces have FA chemisorption. For CO₂ adsorption, there are quite large differences among these surfaces. For example, CO₂ on Mo₂C(101) has much stronger chemisorption energy, while Pd(111) does not adsorb CO₂ (positive adsorption energies). For hydrogen atom adsorption, all these surfaces have very close adsorption energies in the range of -2.8 to -3.0 eV; and there are no differences among these surfaces apart from the fact that H adsorption prefers the surface carbon atom instead of surface Mo atom. For formate adsorption, Mo₂C(101) has stronger chemisorption energy than Pd(111), Pt(111) and Ir(100).

For FA dissociation into surface formate and hydrogen, Pd(111) and Pt(111) have very high activation barriers, while Mo₂C(101) is practically barrier-less. Along with the energy barriers, FA dissociation into surface formate and hydrogen is strongly exothermic on Mo₂C(101), and almost thermal neutral on Pd(111) and Pt(111). It is endothermic on Ir(100). For formate dissociation into surface CO₂ and hydrogen, Mo₂C(101) has very high effective barrier, while Pd(111), Pt(111) and Ir(100) have low effective barrier apart from the reported 1.59 and 1.88 eV for Pd(111) and Pt(111) by Hu *et al.*,^{41c} respectively. The corresponding dissociation energy is endothermic on Mo₂C(101), while strongly exothermic on Pd(111) and Pt(111).

4.4 Conclusions

For the catalytic and selective decomposition of formic acid into CO₂ and hydrogen on β-Mo₂C(101), the adsorption configurations and energies of the surface intermediates (HCO₂H, CO₂, CO, H₂O, HCO₂, CO₂H, CHO, OH, O and H) have been computed systematically. On the basis of the most stable adsorption states the full potential energy surface has been mapped and the minimum energy path has been identified.

Mo₂C(101) represents the most stable termination, and the unit cell contains 16 exposed Mo atoms and 16 exposed C atoms; and detailed calculations and comparisons show that this surface model is large enough for studying formic acid dissociation without significant lateral interactions.

On Mo₂C(101) at 1/16 ML, formic acid has two very different adsorption configurations, HCO₂H-flat (**1**) and HCO₂H-O/OH-down (**2**), but in very close adsorption energies. For HCO₂H-flat (**1**), the most preferred dissociation route is the formation of surface formyl and hydroxyl (CHO+OH); while the formation of either formate and hydrogen (HCO₂+H) or carboxyl and hydrogen (CO₂H+H) is kinetically much less favorable. For HCO₂H-O/OH-down (**2**), the only dissociation route is the formation of surface formate and hydrogen (HCO₂+H), and it is barrier less and highly exothermic. Therefore, formate from HCO₂H-O/OH-down (**2**) represents the most important surface intermediate and the most stable adsorption

configuration HCO₂-O/O-down (**8**) has its two oxygen atoms bridging two surface Mo_A atoms. The dissociation of surface formyl into CH and O has much high energy barrier.

Starting from HCO₂-O/O-down (**8**), formate dissociation into CO₂ and hydrogen is kinetically much more favored than into surface formyl and oxygen (CHO+O). The formation of surface carboxyl from surface CO and OH has high barrier and is highly exothermic, and the dissociation of surface carboxyl into CO+OH is more favorable than into CO₂+H. In addition, H₂O formation from surface OH+H is also kinetically and thermodynamically less favorable. All these rule out the possible formation of CO and H₂O. Therefore, Mo₂C exhibits a unique property to catalyze formic acid dissociation into CO-free hydrogen.

The potential energy surface shows clearly the formate dissociation into CO₂ and hydrogen is the rate-determining step and HCO₂-O/O-down (**8**) represents the resting state. In addition, due to their strong chemisorption, desorption of CO, CO₂ and H₂O is very difficult. The analysis of the overall reaction rates shows the faster FA decomposition via the formate (HCO₂) route over the formyl route (CHO). Finally the Mo₂C(101) catalyzed formic acid dissociation produces CO-free hydrogen.

Because of the proposed Pt-like properties for transition metal carbides, the adsorption properties of HCO₂H, HCO₂, CO₂ and H as well as their dissociation energetic on Mo₂C(101) have been compared with those on Pd(111), Pt(111) and Ir(100). Apart from the adsorption of hydrogen atom, which has very close adsorption energies on all these surfaces, Mo₂C(101) can adsorb these intermediates much stronger than Pd(111) and Pt(111), in particularly the much stronger CO₂ chemisorption.

For the first step of formic acid dissociation into surface formate and hydrogen on Mo₂C(101), it is barrier-less and highly exothermic, while it has higher barriers and is less exothermic on Pd(111) and Pt(111). Due to the much stronger adsorption of surface formate, the dissociation of formate into surface CO₂ and hydrogen has higher effective barrier, while this dissociation step on Pd and Pt has lower barrier.

4.5 References

- (1) Loges, B.; Boddien, A.; Gärtner, F.; Junge, H.; Beller, M. *Top. Catal.* **2010**, *53*, 902–914.
- (2) Grasmann, M.; Laurenczy, G. *Energy Environ. Sci.* **2012**, *5*, 8171–8181.
- (3) Joó, F. *ChemSusChem* **2008**, *1*, 805–808.
- (4) Tedsree, K.; Chan, C. W. A.; Jones, S.; Cuan, Q.; Li, W. K.; Gong, X. Q.; Tsang, S. C. E. *Science* **2011**, *332*, 224–228.
- (5) Tedsree, K.; Li, T.; Jones, S.; Chan, C. W. A.; Yu, K. M. K.; Bagot, P. A. J.; Marquis, E. A.; Smith, G. D. W.; Tsang, S. C. E. *Nat. Nanotechnol.* **2011**, *6*, 302–306.
- (6) Bi, Q. Y.; Du, X. L.; Liu, Y. M.; Cao, Y.; He, H. Y.; Fan, K. N. *J. Am. Chem. Soc.* **2012**, *134*, 8926–8933.
- (7) Gu, X.; Lu, Z. H.; Jiang, H. L.; Akita, T.; Xu, Q. *J. Am. Chem. Soc.* **2011**, *133*,

11822–11825.

- (8) Loges, B.; Boddien, A.; Gärtner, F.; Junge, H.; Beller, M. *Angew. Chem. Int. Ed.* **2008**, *47*, 3962–3965.
- (9) Fellay, C.; Dyson, P. J.; Laurenczy, G. *Angew. Chem. Int. Ed.* **2008**, *47*, 3966–3968.
- (10) Fukuzumi, S. *Eur. J. Inorg. Chem.* **2008**, 1351–1362.
- (11) Johnson, T. R.; Morris, D. J.; Wills, M. *Chem. Soc. Rev.* **2010**, *39*, 81–88.
- (12) Boddien, A.; Mellmann, D.; Gärtner, F.; Jackstell, R.; Junge, H.; Dyson, P. J.; Laurenczy, G.; Ludwig, R.; Beller, M. *Science* **2011**, *333*, 1733–1736.
- (13) Flaherty, D. W.; Berglund, S. P.; Mullins, C. B.; *J. Catal.* **2010**, *269*, 33–43.
- (14) Koós, Á.; Solymosi, F. *Catal. Lett.* **2010**, *138*, 23–27.
- (15) Cui, Z.; Gong, C.; Guo, C. X.; Li, C. M. *J. Mater. Chem. A* **2013**, *1*, 1179–1184.
- (16) Hwu, H. H.; Chen, J. G. *Chem. Rev.* **2005**, *105*, 185–212.
- (17) Schaidle, J. A.; Lausche, A. C.; Thompson, L. T. *J. Catal.* **2010**, *272*, 235–245.
- (18) Nagai, M.; Matsuda, K. *J. Catal.* **2006**, *238*, 489–496.
- (19) Levy, R. L.; Boudart, M. *Science* **1973**, *181*, 547–549.
- (20) Chen, J. G.; *Chem. Rev.* **1996**, *96*, 1447–1498.
- (21) Tominaga, H.; Nagai, M. *Appl. Catal. A* **2008**, *343*, 95–103.
- (22) Piskorz, W.; Adamski, G.; Kotarba, A.; Sojka, Z.; Sayag, C.; Djega-Mariadassou, G. *Catal. Today* **2007**, *119*, 39–43.
- (23) Kotarba, A.; Adamski, G.; Piskorz, W.; Sojka, Z.; Sayag, C.; Djega-Mariadassou, G. *J. Phys. Chem. B* **2004**, *108*, 2885–2892.
- (24) Nagai, M.; Tominaga, H.; Omi, S. *Langmuir* **2000**, *16*, 10215–10220.
- (25) Ren, J.; Huo, C. F.; Wang, J. G.; Li, Y. W.; Jiao, H. J. *Surf. Sci.* **2005**, *596*, 212–221.
- (26) Ren, J.; Huo, C. F.; Wang, J. G.; Cao, Z.; Li, Y. W.; Jiao, H. J. *Surf. Sci.* **2006**, *600*, 2329–2337.
- (27) Ren, J.; Wang, J. G.; Huo, C. F.; Wen, X. D.; Cao, Z.; Yuan, S. P.; Li, Y. W.; Jiao, H. J. *Surf. Sci.* **2007**, *601*, 1599–1607.
- (28) Rocha, A. S.; Rocha, A. B.; Silva, V. T. *Appl. Catal. A* **2010**, *379*, 54–60.
- (29) Shi, X. R.; Wang, J. G.; Hermann, K. *J. Phys. Chem. C* **2010**, *114*, 13630–13641.
- (30) Pistonesi, C.; Juan, A.; Farkas, A. P.; Solymosi, F. *Surf. Sci.* **2008**, *602*, 2206–2211.
- (31) Pronsato, M. E.; Pistonesi, C.; Juan, A.; Farkas, A. P.; Bugyi, L.; Solymosi, F. *J. Phys. Chem. C* **2011**, *115*, 2798–2804.
- (32) Pistonesi, C.; Pronsato, M. E.; Bugyi, L.; Juan, A. *J. Phys. Chem. C* **2012**, *116*, 24573–24581.
- (33) Tominaga, H.; Nagai, M. *J. Phys. Chem. B* **2005**, *109*, 20415–20423.
- (34) Tominaga, H.; Aoki, Y.; Nagai, M. *Appl. Catal. A* **2012**, *423*, 192–204.
- (35) Liu, P.; Rodriguez, J. A. *J. Phys. Chem. B* **2006**, *110*, 19418–19425.
- (36) Schweitzer, N. M.; Schaidle, J. A.; Ezekoye, O. K.; Pan, X. Q.; Linic, S.; Thompson, L. T.

- J. Am. Chem. Soc.* **2011**, *133*, 2378–2381.
- (37) Shi, X. R.; Wang, S. G.; Wang, H.; Deng, C. M.; Qin, Z. F.; Wang, J. G. *Surf. Sci.* **2009**, *603*, 852–859.
- (38) Han, J. W.; Li, L.; Sholl, D. S. *J. Phys. Chem. C* **2011**, *115*, 6870–6876.
- (39) Medford, A. J.; Vojvodic, A.; Studt, F.; Abild-Pedersen, F.; Nørskov, J. K. *J. Catal.* **2012**, *290*, 108–117.
- (40) Zheng, W.; Cotter, T. P.; Kaghazchi, P.; Jacob, T.; Frank, B.; Schlichte, K.; Zhang, W.; Su, D. S.; Schuth, F.; Schlogl, R. *J. Am. Chem. Soc.* **2013**, *135*, 3458–3464.
- (41) Luo, Q.; Feng, G.; Beller, M.; H. Jiao, *J. Phys. Chem. C*, **2012**, *116*, 4149–4156.
- (42) Zhang, R.; Liu, H.; Wang, B.; Ling, L. *J. Phys. Chem. C* **2012**, *116*, 22266–22280.
- (43) Hu, C.; Ting, S. W.; Chan, K. Y.; Huang, W. *Int. J. Hydrogen Energy* **2012**, *37*, 15956–15965.
- (44) Yuan, D.W.; Liu, Z. R. *J. Power Sources*, **2013**, *224*, 241–249.
- (45) Gao, W.; Keith, J. A.; Anton, J.; Jacob, T. *Dalton Trans.* **2010**, *39*, 8450–8456.
- (46) Kang, Y.; Qi, L.; Li, M.; Diaz, R. E.; Su, D.; Adzic, R. R.; E. Stach, J. Li, C. B. Murray, *ACS Nano* **2012**, *6*, 2818–2825.
- (47) Li, X.; Lim, K. H. *ChemCatChem* **2012**, *4*, 1311–1320.
- (48) Pistonesi, C.; Juan, A.; Farkas, A. P.; Solymosi, F. *Surf. Sci.* **2010**, *604*, 914–919.
- (49) Dubois, J.; Epicier, T.; Esnouf, C.; Fantozzi, G.; Convert, P. *Acta Metall.* **1988**, *8*, 1891–1901.
- (50) Epicier, T.; Dubois, J.; Esnouf, C.; Fantozzi, G.; Convert, P. *Acta Metall.* **1988**, *8*, 1903–1921.
- (51) Wang, T.; Liu, X. W.; Wang, S. G.; Huo, C. F.; Li, Y. W.; Wang, J.; Jiao, H. *J. Phys. Chem. C* **2011**, *115*, 22360–22368.
- (52) Haines, J.; Leger, J. M.; Château, C.; Lowther, J. E.; *J. Phys. Condens. Mat.* **2001**, *13*, 2447–2454.
- (53) Rudy, E.; Windisch, S.; Stosick, A. J.; Hoffman, J. R.; *Trans. Metall. Soc. AIME.* **1967**, *239*, 1247–1267.
- (54) Wang, X. H.; Hao, H. L.; Zhang, M. H.; Li, W.; Tao, K. Y. *J. Solid State Chem.* **2006**, *179*, 538–543.
- (55) Nagai, M.; Zahidul, A. M.; Matsuda, K. *Appl. Catal. A* **2006**, *313*, 137–145.
- (56) Kresse, G.; Hafner, J. *Phys. Rev. B* **1993**, *47*, 558–561.
- (57) Kresse, G.; Hafner, J. *Phys. Rev. B* **1994**, *49*, 14251–14269.
- (58) Kresse, G.; Furthmüller, J. *Comput. Mater. Sci.* **1996**, *6*, 15–50.
- (59) Kresse, G.; Furthmüller, J. *Phys. Rev. B* **1996**, *54*, 11169–11186.
- (60) Blöchl, P. E.; *Phys. Rev. B* **1994**, *50*, 17953–17979.
- (61) Perdew, J. P.; Bruke, K.; Ernzerhof, M. *Phys. Rev. Lett.* **1996**, *77*, 3865–3868.
- (62) Methfessel, M.; Paxton, A. T. *Phys. Rev. B* **1989**, *40*, 3616–3621.

-
- (63) Monkhorst, M.; Pack, J. D. *Phys. Rev. B* **1976**, *13*, 5188–5192.
- (64) Jónsson, H.; Mills, G.; Jacobsen, K.W. In *Classical and Quantum Dynamics in Condensed Phase Simulations*; B. J. Berne, D. F. Ciccotti, Eds, World Scientific: Singapore, **1998**; p385.
- (65) Nakatsuji, H.; Yoshimoto, M.; Hada, M.; Domen, K.; Hirose, C. *Surf. Sci.* **1995**, *336*, 232–244.
- (66) Nakatsuji, H.; Yoshimoto, M.; Umemura, Y.; Takagi, S.; Hada, M. *J. Phys. Chem.* **1996**, *100*, 694–700.
- (67) Yoshimoto, M.; Takagi, S.; Umemura, Y.; Hada, M.; Nakatsuji, H. *J. Catal.* **1998**, *173*, 53–63.
- (68) Lintuluoto, M.; Nakatsuji, H.; Hada, M.; Kanai, H. *Surf. Sci.* **1999**, *429*, 133–142.
- (69) Persson, P.; Lunell, S.; Ojamae, L. *Int. J. Quantum. Chem.* **2002**, *89*, 172–180.

5 Full Acrolein Hydrogenation on Ni(111)

5.1 Introduction

Selective hydrogenation of α,β -unsaturated aldehydes to the corresponding unsaturated alcohols has attracted much interests, and this is because that such alcohols are very important intermediates in fine chemicals and pharmaceuticals.¹ Since the C=C bond in α,β -unsaturated aldehydes is generally easier to be hydrogenated than the C=O bond both thermodynamically and kinetically,² the biggest challenge remains the finding of suitable catalysts for producing the desired unsaturated alcohols. Many catalysts, especially the platinum group metals, have been used and the selectivity is mainly controlled by the nature of catalysts, e.g.; Pt alloyed with an electropositive metal can significantly improve the selectivity in the hydrogenation of α,β -unsaturated aldehydes toward unsaturated alcohols³ and addition of various promoters plays an important role on improving the production of unsaturated alcohols.⁴ For understanding the catalytic selectivity, it is necessary to know the detailed reaction mechanisms, especially the competitive processes in the hydrogenation of the C=C and C=O bonds.

As the simplest α,β -unsaturated aldehyde, acrolein has been used to study the selective hydrogenation. Figure 5.1 shows the hydrogenation network of acrolein into propanol. The selective addition of one hydrogen atom can form four radical intermediates and the addition of a second hydrogen atom to these intermediates can form three closed-shell intermediates, e.g.; allyl alcohol (prop-2-en-1-ol), propanal and prop-1-en-1-ol. The addition of a third hydrogen atom can form four radical intermediates from six possibilities and the last hydrogen addition forms propanol as the final product.

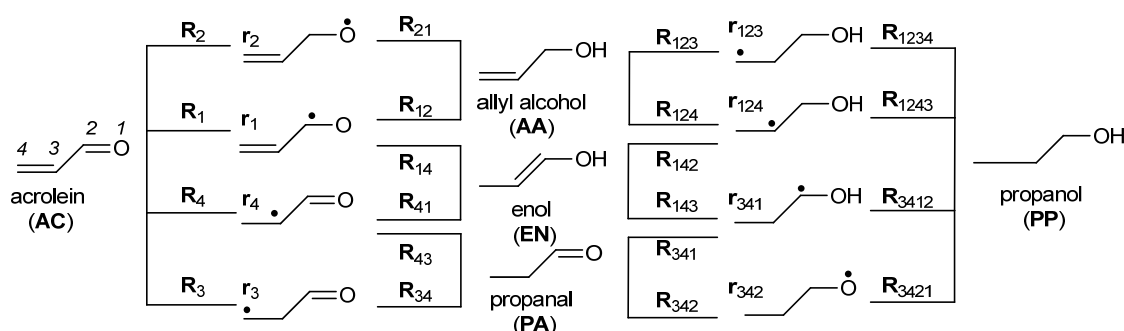


Figure 5.1 Hydrogenation network of acrolein to propanol

Due to their industrial importance, there are many experimental studies on the selective hydrogenation of α,β -unsaturated aldehydes. Touroude investigated the catalytic behaviors of the group VIII transition metals in the deuterium-acrolein reaction.⁵ Coq *et al.*,⁶ reported acrolein hydrogenation on group VIII metal supported catalysts and found the selectivity depending on the nature of the supports and the size of the catalysts. Claus *et al.*,⁷ reported

acrolein hydrogenation on Ag-based catalysts. Brandt *et al.*,⁸ found that acrolein coverage on the Ag(111) surface plays an important role in the selectivity toward the formation of allyl alcohol. Gold catalyst shows unexpected activity for producing allyl alcohol.⁹ Chen *et al.*,¹⁰ studied acrolein hydrogenation on bimetallic catalysts from experiment and theory, and found the selectivity depending on the electronic nature of the catalysts.

Density functional theory (DFT) studies on the selective acrolein hydrogenation have been carried out. Chen *et al.*,¹¹ computed acrolein hydrogenation on pure gold clusters, In-doped gold surfaces and ZnO supported gold clusters as well as gas phase hydrogenation. Liu *et al.*,¹² reported acrolein selective hydrogenation on ZrO₂-supported single gold catalysts. Rösch *et al.*,¹³ reported selective acrolein hydrogenation on different silver surfaces. Hu *et al.*,¹⁴ computed acrolein hydrogenation on the stepped Pt(211) and Au(211) surfaces. Illas *et al.*,¹⁵ investigated acrolein hydrogenation on the clean Cu(111) and S-covered Cu(111) surfaces. The hydrogenation of acrolein, crotonaldehyde and prenal on Pt(111) also has been computed.¹⁶

As an excellent hydrogenation catalyst widely used in industry and academic research, and there are many theoretical studies on Ni hydrogenation. For example, Remediakis *et al.*,¹⁷ reported CO hydrogenation to methanol ($\text{CO} + 2\text{H}_2 \rightarrow \text{CH}_3\text{OH}$), and Olive *et al.*,¹⁸ reported HCN hydrogenation to methylamine ($\text{HCN} + 2\text{H}_2 \rightarrow \text{CH}_3\text{NH}_2$). As a fundamental process in the refining industry benzene hydrogenation ($\text{C}_6\text{H}_6 + 3\text{H}_2 \rightarrow \text{C}_6\text{H}_{12}$) was explored by Mittendorfer and Hafner.¹⁹ CO₂ hydrogenation into formic acid ($\text{CO}_2 + \text{H}_2 \rightarrow \text{HCO}_2\text{H}$) was reported by Peng *et al.*²⁰ However, the mechanism of acrolein hydrogenation on nickel is still unclear. This work reports a detailed theoretical study on acrolein hydrogenation on Ni(111) for the understanding into the selective acrolein hydrogenation into either allyl alcohol or propanal or propanol.

5.2 Computational details

Spin polarized periodic DFT method implemented in Vienna *ab initio* simulation package (VASP)²¹ was used. The electron exchange and correlation energy was treated within the generalized gradient approximation (GGA) in the Perdew-Burke-Ernzerhof formalism (PBE).²² The core electron interactions were described with the projector augmented wave (PAW) method.²³ The cut-off energy was set up to 400 eV. The forces convergence was set to be less than 0.02 eV/Å, and the total energy convergence was set to be less than 10⁻⁴ eV. Electron smearing of $\sigma = 0.1$ eV²⁴ was used following the Methfessel-Paxton scheme. Brillouin zone sampling was employed using a Monkhorst-Pack grid.²⁵

For the Ni(111) surface, the first Brillouin zone was sampled with a 3×3×1 k-point grid. A p(3×4) super cell with 12 atoms at each layer was used. Ni(111) was modelled with a three-layer slab with a 12 Å vacuum zone in the z direction to separate the slabs; the first two layers with adsorbates are relaxed and the bottom layer is fixed to its bulk. This three-layer model was well tested and used in our previous work.²⁶

The nudged elastic band (NEB) method was used to locate the transition states of the hydrogenation reactions.²⁷ The computed vibrational frequencies were used to characterize a minimum state without imaginary frequencies or an authentic transition state with only one imaginary frequency. The adsorption energy is defined as $E_{\text{ads}} = E_{\text{A/slab}} - [E_{\text{slab}} + E_{\text{A}}]$, where $E_{\text{A/slab}}$ is the total energy of the slab with adsorbate A, E_{slab} is the total energy of the bare slab, and E_{A} is the total energy of free adsorbate A in gas phase. Thus, the more negative the E_{ads} , the stronger the adsorption. The reaction energy (E_{r}) and activation barrier (E_{a}) are calculated using $E_{\text{r}} = E_{\text{FS}} - E_{\text{IS}}$ and $E_{\text{a}} = E_{\text{TS}} - E_{\text{IS}}$, respectively, where E_{IS} , E_{FS} and E_{TS} are the total energies of the initial state (IS), final state (FS) and transition state (TS), respectively.

5.3 Results and Discussion

For convince and simplicity, acrolein (**AC**) is numbered from O₁ to C₄ and this is also the sequence for the stepwise hydrogen addition (Figure 5.1). For example, first hydrogen addition at O₁, C₂, C₃ and C₄ atoms forms the four radical intermediates; i.e.; 1-hydroxyl allyl radical (**r**₁), prop-2-en-1-oxyl radical (**r**₂), 3-oxopropyl radical (**r**₃) and 1-formylethyl radical (**r**₄); respectively, and the corresponding routes are named as **R**₁, **R**₂, **R**₃ and **R**₄. For second hydrogen addition to the four radical intermediates, six possible reaction routes exist and three closed-shell products are produced, i.e.; allyl alcohol (**AA**), propanal (**PA**) and enol (**EN**). For **AA** formation, the alternative routes are **R**₁₂ (H atom is added to C₂ of **r**₁) and **R**₂₁ (H atom is added to O₁ of **r**₂). For **PA** formation, the alternative routes are **R**₃₄ (H atom is added to C₄ of **r**₃) and **R**₄₃ (H atom is added to C₃ of **r**₄). For **EN** formation, the alternative routes are **R**₁₄ (H atom is added to C₄ of **r**₁) and **R**₄₁ (H atom is added to O₁ of **r**₄). For third hydrogen addition to **AA**, **PA** and **EN**, each species has two reaction routes and all six reaction routes can form four radical intermediates; i.e.; 3-hydroxyl propyl radical (**r**₁₂₃) from **R**₁₂₃, 1-hydroxyl isopropyl radical (**r**₁₂₄) from either **R**₁₂₄ or **R**₁₄₂, 1-hydroxyl propyl radical (**r**₃₄₁) from either **R**₃₄₁ or **R**₁₄₃, and propoxyl radical (**r**₃₄₂) from **R**₃₄₂. For final hydrogen addition, **PP** can be formed from **R**₁₂₃₄, **R**₁₂₄₃, **R**₃₄₁₂ or **R**₃₄₂₁. The detailed structural parameters and energetic data for the full hydrogenation reaction are given in Appendix Table A2.

5.3.1 Hydrogenation intermediates

Figure 5.2 shows most stable adsorption configurations along with the selected bond parameters for the hydrogenation intermediates from acrolein to propanol.

Acrolein (AC). Molecular **AC** exhibits *trans* and *cis* conformations. The computed structural parameters agree well with the available experimental data by Blom *et al.*,²⁸ and the *trans* configuration is the major isomer (98%), as also found experimentally (96% at room temperature). Therefore we used only the *trans* isomer for our calculations on Ni(111). As shown in Figure 5.2, the most stable **AC** adsorption configuration has the C=O and C=C bonds over two neighboring face centered cubic (fcc) sites; and the C=O and C=C bonds are elongated to 135 and 145 pm, compared to the gas phase values (123 and 134 pm). The adsorption energy is -1.15 eV, indicating a strong interaction of **AC** with the surface Ni atoms.

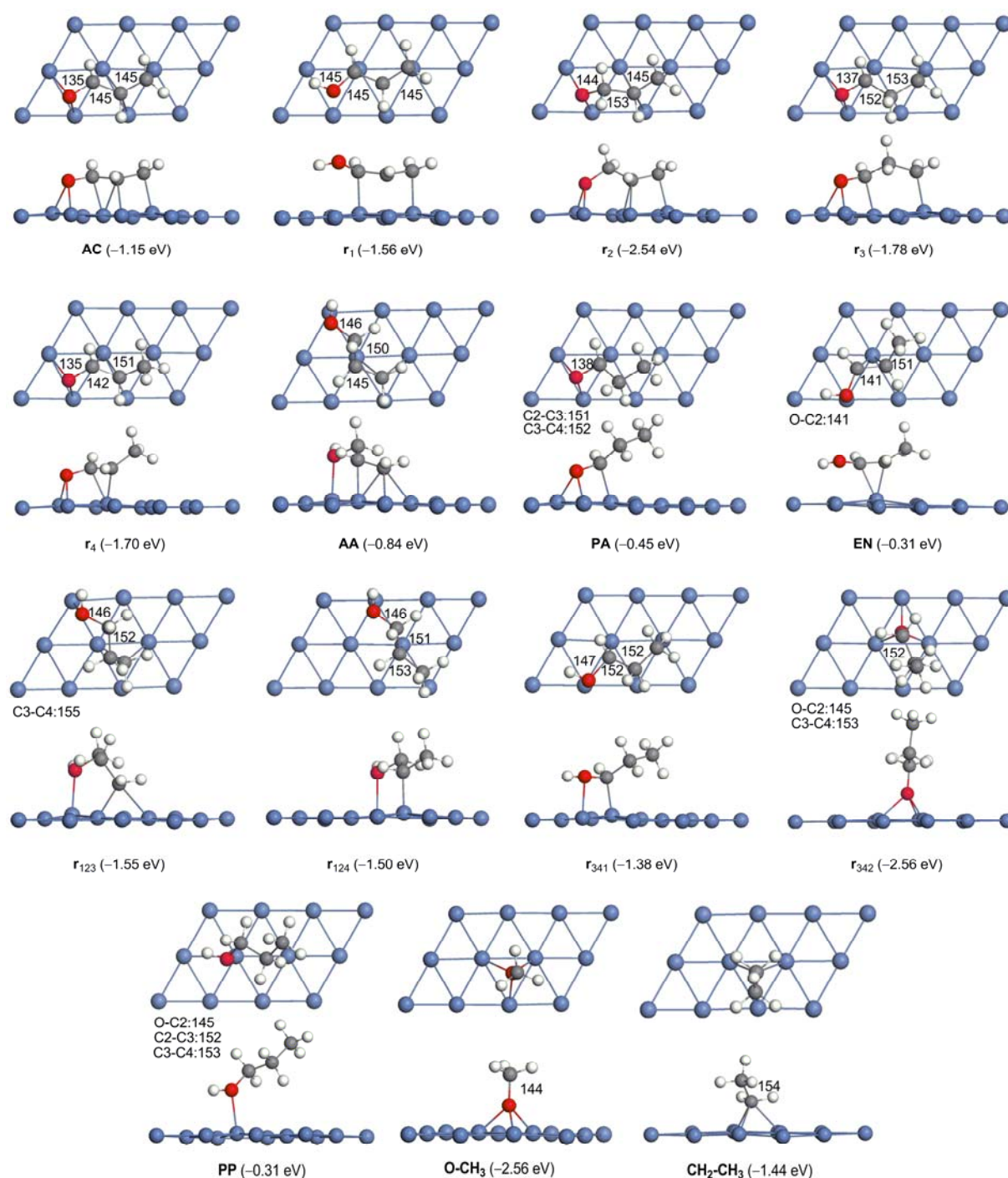


Figure 5.2 Adsorption configurations involved in acrolein hydrogenation into propanol on Ni(111) (bond distances in pm).

First H addition: The most stable adsorption configurations for the intermediates of first H addition, r_1 , r_2 , r_3 and r_4 , are shown in Figure 5.2. In r_1 , the H atom is added to O₁ and the free intermediate can be considered as a 1-hydroxyl allyl radical; C₂ and C₄ bridge two neighboring surface nickel atoms and the adsorption energy is -1.56 eV. In r_2 , the H atom is added to C₂ and the free intermediate can be considered as prop-2-en-1-oxyl radical; O₁ bridges two

surface Ni atoms and the C=C bond locates over the fcc site and the adsorption energy is -2.54 eV. Such strong adsorption energy (-2.56 eV) is also found for methoxyl radical (Figure 5.2) on Ni(111), where the oxygen atom locates over the fcc site. However, at high coverage (1/4 ML on a (2×2) supercell), the most stable adsorption configuration of methoxyl radical has the oxygen atom atop on the Ni(111) surface and the adsorption energy is -1.86 eV.¹⁷ It is worthy to note that on the three-fold hollow site of the Pd(111) and Cu(111) surfaces,²⁹ the adsorption energy of methoxyl radical is -1.68 and -2.45 eV, respectively, while that on the atop site is -0.93 and -1.73 eV, respectively. In r_3 , the H atom is added to C_3 and the free intermediate can be considered as 3-oxopropyl radical; the C=O group adsorbs over the fcc site and C_4 adsorbs atop on a surface Ni atom and the adsorption energy is -1.78 eV. In r_4 , the H atom is added to C_4 , and the free intermediate can be considered as 1-formylethyl radical; where the C=O group locates over the fcc site as well as C_2 and C_3 chelate a surface nickel atom, and the adsorption energy is -1.70 eV.

As shown above, the most stable surface intermediate for one H addition is r_1 , and the other three surface intermediates are much less stable. However we computed further H addition to all intermediates for analyzing the selective hydrogenation.

Second H addition: The most stable adsorption configurations for the intermediates of second H addition, allyl alcohol (**AA**), propanal (**PA**) and prop-1-en-1-ol (**EN**), are shown in Figure 5.2. For **AA**, the most stable adsorption configuration has the C=C bond capping the fcc site and O_1 atop at one surface Ni atom; and the adsorption energy is -0.84 eV. For **PA**, the most stable adsorption configuration has the C=O bond capping the fcc site and the ethyl group pointing away from the surface; and the adsorption energy is -0.45 eV. For **EN**, the most stable adsorption configuration has the central C=C bond coordination with only one surface Ni atom; and the adsorption energy is -0.31 eV. The most stable surface intermediate is the adsorbed allyl alcohol (**AA**), and the adsorption of propanal (**PA**) and prop-1-en-1-ol (**EN**) is weaker.

Third H addition: Starting from these closed-shell intermediates, third H addition can form four possible radicals, 3-hydroxyl propyl radical (r_{123}), 1-hydroxyl isopropyl radical (r_{124}), 1-hydroxyl propyl radical (r_{341}) and propoxyl radical (r_{342}) and these configurations are shown in Figure 5.2. In 3-hydroxyl propyl radical (r_{123}) the OH group interacts with one surface Ni atom and C_4 radical carbon bridges two surface Ni atoms, and the adsorption energy is -1.55 eV. In 1-hydroxyl isopropyl radical (r_{124}) the OH group and C_3 radical carbon bridge two neighboring surface Ni atoms; and the adsorption energy is -1.50 eV. In 1-hydroxyl propyl radical (r_{341}), O_1 and C_2 radical carbon bridge two neighboring surface Ni atoms and the adsorption energy is -1.38 eV. The adsorption energies of these carbon radicals are close to that (-1.44 eV) of ethyl radical on Ni(111) (Figure 5.2). In propoxyl radical (r_{342}), O_1 is at the

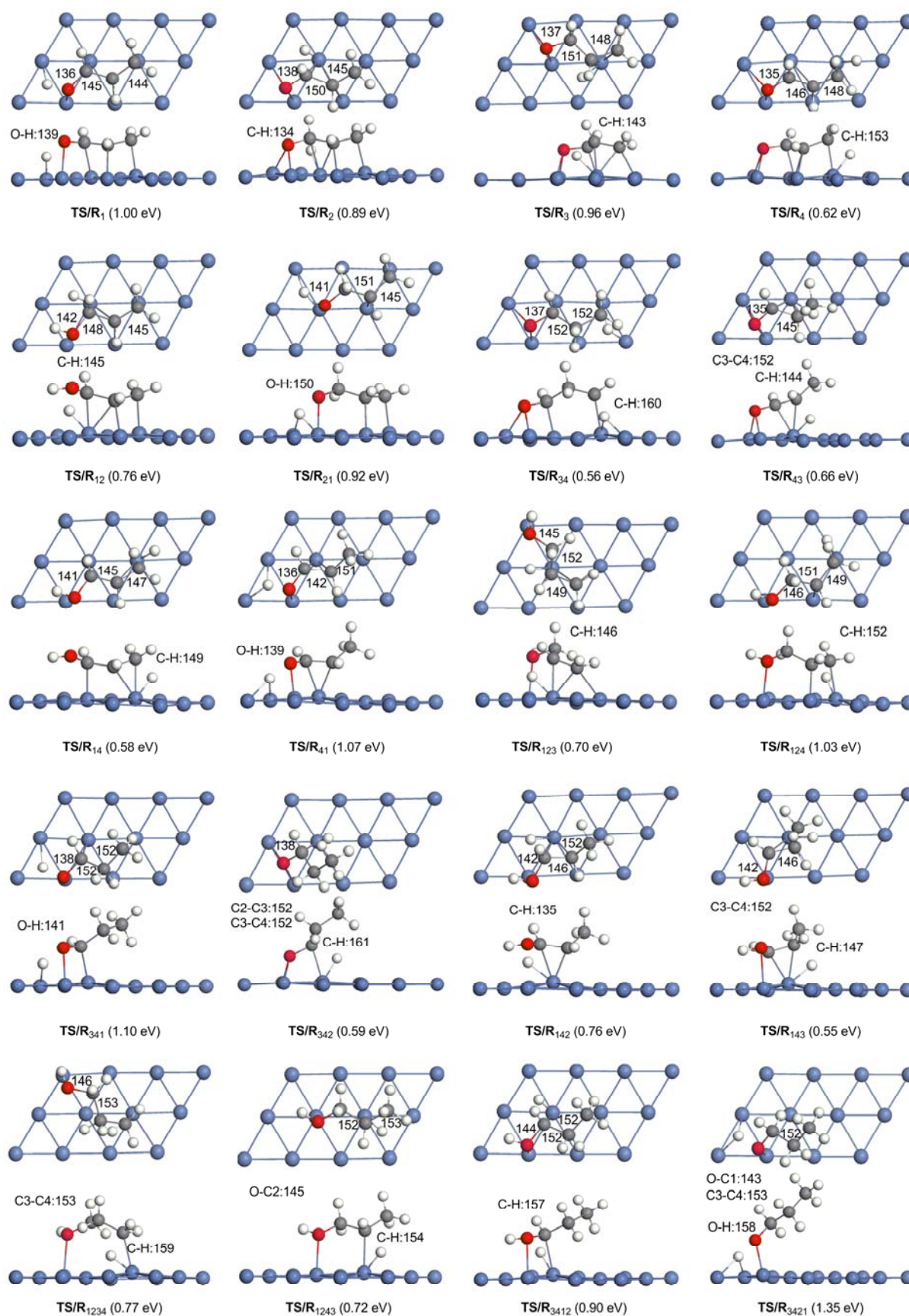


Figure 5.3 Transition state configurations involved in acrolein hydrogenation into propanol on Ni(111) (bond distances in pm)

three-fold fcc hollow site, and the adsorption energy is -2.56 eV, which is close to that of the methoxyl adsorption (-2.54 eV). These results show that oxygen radical has stronger adsorption energy than those of carbon radicals on Ni(111).

Fourth H addition: The final hydrogenation product is propanol (**PP**), and the most stable adsorption configuration (Figure 5.2) has O_1 atop at one surface Ni atom with adsorption energy of -0.31 eV. It is noted that the adsorption configuration at the three-fold hollow site is not stable, and optimization leads to atop site.

5.3.2 Hydrogenation transition states

On the basis of the computed intermediates we have computed the corresponding transition states for analyzing their kinetic and thermodynamic parameters in the hydrogenation reaction. The optimized transition states along with the critical bond parameters are shown in Figure 5.3; and the activation barrier and reaction energy of each step is shown in Figure 5.4.

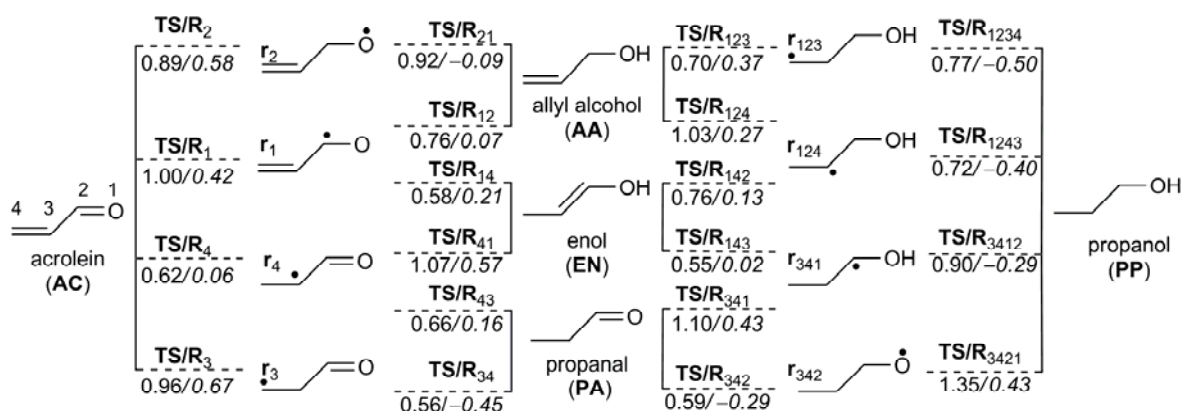


Figure 5.4 Acrolein hydrogenation route with intermediates (activation barrier in plain and the reaction energy in italics, in eV)

Prior to consider the transition states of H addition, we computed hydrogen adsorption. On Ni(111), there is only dissociative hydrogen adsorption,³⁰ and the adsorption energy of one H_2 gas molecule is -1.01 eV, which is close to that of one acrolein molecule (-1.15 eV); indicating the possibility for the co-adsorption of atomic hydrogen and molecular acrolein. Since the migration of atomic hydrogen on the Ni(111) surface has negligible barrier (< 0.15 eV),³¹ we started our transition state search by putting the hydrogen atom directly to the attached oxygen or carbon atom. This approach has also been used in acrolein hydrogenation on Pt(111) by Loffreda *et al.*^{16c}

First H addition: Starting from the most stable adsorption configurations of acrolein (**AC**) and the four intermediates (r_1 , r_2 , r_3 and r_4) from the first H addition, we located four corresponding transition states (**TS/R₁**, **TS/R₂**, **TS/R₃** and **TS/R₄**). For r_1 formation, the H atom is added to O_1 . In transition state **TS/R₁**, the forming H-O distance is 139 pm; the activation barrier is 1.00 eV and the reaction is endothermic by 0.42 eV. For r_2 formation, the H atom is

added to C₂. In transition state **TS/R**₂, the forming H-C distance is 134 pm; the activation barrier is 0.89 eV; and the reaction is endothermic by 0.58 eV. For r₃ formation, the H atom is added to C₃. In transition state **TS/R**₃, the forming H-C distance is 143 pm; the activation barrier is 0.96 eV and the reaction is endothermic by 0.67 eV. For r₄ formation, the H atom is added to C₄. In transition state **TS/R**₄, the forming H-C distance is 153 pm; the activation barrier is 0.62 eV; and the reaction is almost thermal neutral (0.06 eV).

Compared with the formation of other intermediates which have higher activation barriers and are stronger endothermic, the formation of r₄ (1-formylethyl radical) is favorable both kinetically and thermodynamically.

Second H addition: For allyl alcohol (**AA**) formation, there are two formation ways, i.e.; by adding second H atom to r₁ at C₂ via transition state **TS/R**₁₂ and to r₂ at O₁ via transition state **TS/R**₂₁. In **TS/R**₁₂, the forming C-H distance is 145 pm and in **TS/R**₂₁, the forming H-O distance is 150 pm. For **AA** formation via **TS/R**₁₂, the activation barrier is 0.76 eV and the reaction is nearly thermal neutral (0.07 eV), while for the reaction via **TS/R**₂₁, the activation barrier is 0.92 eV and the reaction is exothermic by 0.09 eV. Starting from **AC**, the effective barrier is 1.18 eV from **R**₁₂, and 1.50 eV from **R**₂₁, and **AA** formation is endothermic by 0.49 eV.

The formation of propanal (**PA**) has two ways, i.e.; by adding the second H atom to r₃ at C₄ via transition state **TS/R**₃₄ and to r₄ at C₃ via transition state **TS/R**₄₃. The forming C-H distance is 160 pm in **TS/R**₃₄ and 144 pm in **TS/R**₄₃. For **PA** formation via **TS/R**₃₄, the activation barrier is 0.56 eV and the reaction is exothermic (-0.45 eV), while for the reaction via **TS/R**₄₃, the activation barrier is 0.66 eV and the reaction is endothermic (0.16 eV). Starting from **AC**, the effective barrier is 1.23 eV from **R**₃₄, and 0.72 eV from **R**₄₃, and **PA** formation is endothermic by 0.22 eV.

The formation of prop-1-en-1-ol (**EN**) also has two ways, i.e.; by adding the second H atom r₁ at C₄ via transition state **TS/R**₁₄ and to r₄ at O₁ via transition state **TS/R**₄₁. In **TS/R**₁₄, the forming C-H distance is 149 pm, and in **TS/R**₄₁, the forming O-H distance is 139 pm. For **EN** formation via **TS/R**₁₄, the activation barrier is 0.58 eV and the reaction is endothermic by 0.21 eV, while for the reaction via **TS/R**₄₁, the activation barrier is 1.07 eV and the reaction is endothermic by 0.57 eV. Starting from **AC**, the effective barrier is 1.00 eV from **R**₁₄, and 1.13 eV from **R**₄₁, and **EN** formation is endothermic by 0.63 eV.

On the basis of the above results and starting from **AC**, the more preferred route for **AA** formation has effective barrier of 1.18 eV and is endothermic by 0.49 eV; and the more preferred route for **EN** formation has effective barrier of 1.00 eV and is endothermic by 0.63 eV, while **PA** formation has effective barrier of 0.72 eV and is endothermic by 0.22 eV. These results show clearly that **PA** formation is most favorable both kinetically and thermodynamically, while the formation of **AA** has the highest effective barrier. Since **AA** has stronger adsorption energy than **PA** (-0.84 eV for **AA** and -0.45 eV for **PA**), **AA** desorption is

more difficult than **PA** on Ni(111).

Third H addition: Despite of the fact that **PA** formation is more favored than that of **AA** and **EN**, we computed further hydrogenation to all three intermediates towards to the formation of propanol (**pp**) for general comparison.

Starting from **AA**, third H atom can be added either to C₃ via transition state **TS/R**₁₂₃ to form 3-hydroxyl propyl radical intermediate (**r**₁₂₃) or to C₄ via transition state **TS/R**₁₂₄ to form 1-hydroxyl isopropyl radical intermediate (**r**₁₂₄). The forming H-C distance in **TS/R**₁₂₃ and **TS/R**₁₂₄ is 146 and 152 pm, respectively. For the formation of **r**₁₂₃, the activation barrier is 0.70 eV and the reaction is endothermic by 0.37 eV, while for that of **r**₁₂₄, the activation barrier is 1.03 eV and the reaction is endothermic by 0.27 eV. Therefore, **r**₁₂₃ formation is kinetically more preferred.

Starting from **PA**, third H atom can be added either to O₁ via transition state **TS/R**₃₄₁ to form 1-hydroxyl propyl radical intermediate (**r**₃₄₁) or to C₂ via transition state **TS/R**₃₄₂ to form propoxyl radical (**r**₃₄₂) intermediate. The forming H-O distance in **TS/R**₃₄₁ is 141 pm, and the forming C-H distance in **TS/R**₃₄₂ is 161 pm. For the formation of **r**₃₄₁ the activation barrier is 1.10 eV and the reaction is endothermic by 0.43 eV, while for that of **r**₃₄₂, the activation barrier is 0.59 eV and the reaction is exothermic by 0.29 eV. Therefore, **r**₃₄₂ formation is more preferred both kinetically and thermodynamically.

Starting from **EN**, third H atom can be added either to C₂ via transition state **TS/R**₁₄₂ to form 1-hydroxyl isopropyl radical intermediate (**r**₁₂₄) or to C₃ via transition state **TS/R**₁₄₃ to form to 1-hydroxyl propyl radical intermediate (**r**₃₄₁). The forming H-C distance in **TS/R**₁₄₂ and **TS/R**₁₄₃ is 135 and 147 pm, respectively. For the formation of **r**₁₂₄, the activation barrier is 0.76 eV and the reaction is endothermic by 0.13 eV, while for that of **r**₃₄₁ the activation barrier is 0.55 eV and the reaction is almost thermal neutral (0.02 eV). Therefore, **r**₃₄₁ formation is more preferred kinetically and thermodynamically.

Fourth H addition: For propanol (**PP**) formation we used all four radical intermediates. The activation barrier for **PP** formation is 0.77, 0.72, 0.90 and 1.35 eV for H addition to **r**₁₂₃ at C₄, to **r**₁₂₄ at C₃, to **r**₃₄₁ to C₂ and **r**₃₄₂ to O₁, respectively; and the corresponding reaction energy is -0.50, -0.40, -0.29 and 0.43, respectively. In the corresponding transition states, the H-C forming distance is 159 pm in **TS/R**₁₂₃₄, 154 pm in **TS/R**₁₂₄₃ and 157 pm in **TS/R**₃₄₁₂; the H-O distance is 158 pm in **TS/R**₃₄₂₁.

For **PP** formation from **AA**, the more preferred route has effective barrier of 1.03 eV and the reaction is exothermic by 0.13 eV. For **PP** formation from **PA**, the more preferred route has effective barrier of 1.33 eV and the reaction is endothermic by 0.14 eV. For **PP** formation from **EN**, the more preferred route effective barrier is 0.85 eV and the reaction is exothermic by 0.27 eV.

5.3.3 Potential energy surface of selective hydrogenation

On the basis of the discussed stepwise hydrogenation barriers and reaction energies, we

mapped the potential energy surface for analyzing the selectivity of acrolein hydrogenation on Ni(111). Since **EN** can tautomerize to **PA** and also has higher effective barrier, Figure 5.5 shows only the more preferred hydrogenation routes for the formation of **AA** and **PA**. For the adsorption of molecular hydrogen and acrolein, the adsorption energy of acrolein is -1.15 eV, which is close to the dissociative adsorption of molecular hydrogen (-1.01 eV); and their co-adsorption is possible. It is reasonable to discuss the hydrogenation steps from surface hydrogen atoms following the proposed Langmuir-Hinshelwood mechanism on the surface.

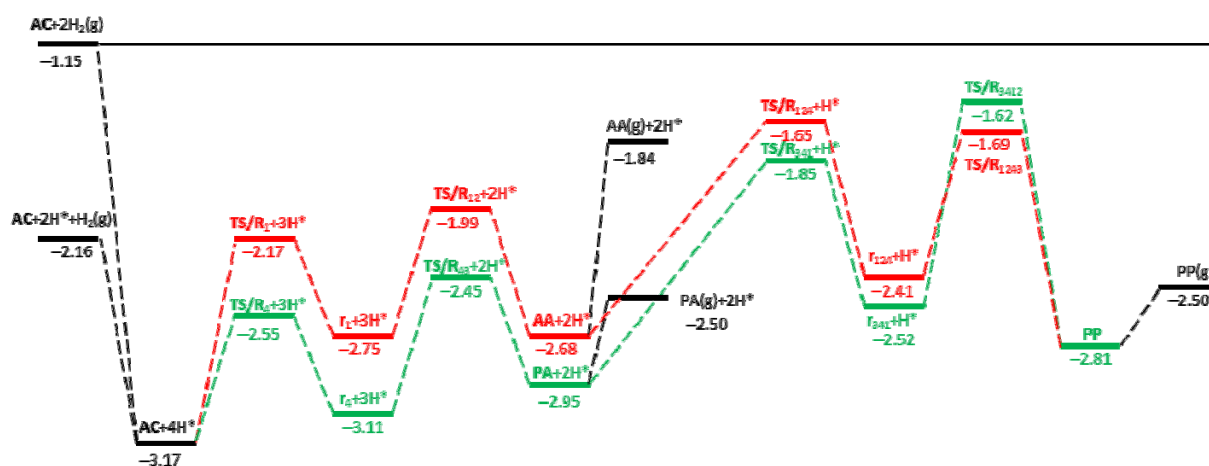


Figure 5.5 Potential energy surface of acrolein (**AC**) hydrogenation into allyl alcohol(**AA**), propionaldehyde (**PA**) and propanol (**PP**) on Ni(111) (energies in eV)

For the competitive formation of **AA** and **PA**, it is found that **PA** formation has lower effective barrier than **AA** formation (0.72 vs. 1.18 eV); and **PA** formation is less endothermic than **AA** formation (0.22 vs. 0.49 eV). Therefore, **PA** formation on the Ni(111) surface is more preferred kinetically and thermodynamically.

For further hydrogenation of **AA** and **PA** into **PP**, it is necessary to compare their adsorption (or desorption) energies with their hydrogenation barriers. We found that **AA** has stronger adsorption energy than **PA** (-0.84 vs. -0.45 eV), and **PA** can desorb easier than **AA** from the Ni(111) surface. For **AA** hydrogenation, the effective barrier is 1.03 eV; and the reaction is exothermic by 0.13 eV. For **PA** hydrogenation, the effective barrier is 1.33 eV; and the reaction is endothermic by 0.14 eV. Since these effective barriers are much higher than their adsorption energies; both **AA** and **PA** prefer to desorb from the surface instead of hydrogenation on the Ni(111) surface. Thus it is easily to conclude that **AC** hydrogenation on the Ni(111) surface mainly forms **PA**, and the formation of **AA** is less favored, and **PA** further hydrogenation to **PP** is kinetically hindered. Since the adsorption of **AA** and **PA** are much lower than that of molecular hydrogen on Ni(111), one might consider a hydrogenation mechanism with atomic hydrogen on the Ni(111) surface and **AA** (or **PA**) coming from the gas phase (the Eley-Rideal mechanism), which is different from the Langmuir-Hinshelwood

mechanism.

That the hydrogenation of the C=C double bond in **AC** into **PA** is more favored kinetically and thermodynamically than the hydrogenation of the C=O double in **AC** into **AA** is in agreement with the general trend;² and the same trend is also found for the C=C double bond hydrogenation in **AA** and the C=O double bond hydrogenation in **PA**.

Table 5.1 Adsorption energies (eV) of **AC**, **AA** and **PA** on different surfaces

Surface	AC	AA	PA	Ref
Ni(111)	-1.15	-0.84	-0.45	
Au(110)	-0.42	-0.43	-0.12	11e
In/Au(110)	-0.73	-0.40	-0.28	11e
Au ₂₀	-0.46	-0.56	-0.40	11d
Au(211)	-0.22	-0.45	-0.07	14
Pt(211)	-1.63	-1.45	-0.79	14
Pt(111)	-1.06	-1.08	-0.23	16c
Ag(110)	-0.17	-0.19	-0.21	13a
O _{sub} /Ag(111)	-0.10	-0.21	-0.13	13a

5.3.4 Comparison with other surfaces

Now it is interesting to compare acrolein hydrogenation on different surfaces (Table 5.1). It is found that **AC** has stronger adsorption on Ni(111) than on the Au and Ag surfaces as well as on the Pt(111) surface, but weaker than on the Pt(211) surface. Recent DFT calculations show that the adsorption energies and configurations depend on the coverage, e.g.; **AC** on the Ag(111) surface has a parallel adsorption configuration at low coverage with adsorption energy of -0.06 eV, while head-to-head and head-to-tail configurations at high coverage with adsorption energy of -0.18 eV.³² For **AA**, the adsorption energy on Ni(111) is stronger than on the Au and Ag surfaces, but weaker than on the Pt(211) and Pt(111) surfaces. For **PA**, the adsorption energy on Ni(111) is stronger than on the Au and Ag surfaces as well as on the Pt(111) surface, but weaker than on the Pt(211) surface. Table 5.1 also shows that on Ni(111), the adsorption energy is in the order of **AC**, **AA** and **PA**; and the same order is also found on the Pt(211) surface, while disorders are found on other surfaces. Such differences in adsorption energies on different surfaces indicate their adsorption (or desorption) strength, which controls their hydrogenation mechanisms and determines the hydrogenation selectivity as discussed below.

The selective hydrogenation of **AC** to **AA** and **PA** on the Au(110) surface and on the Au₂₀ cluster has been reported by Chen *et al.*. The effective barrier for the formation of **AA** and **PA** is 0.45 and 0.92 eV on the Au(110) surface,^{11e} respectively, as well as 0.41 and 1.00 eV on

one In atom decorated Au(110) surface, respectively, indicating the preference of **AA** formation on these surfaces. On the Au₂₀ cluster the effective barriers for **AA** and **PA** formation are close (0.77 vs. 0.83 eV),^{11d} indicating their competition. On AuOH/ZrO₂(212), Liu *et al.*,¹² reported the preference of **AA** formation over **PA** formation on the basis of the computed effective barriers (0.46 vs. 0.82 eV). Further hydrogenation of **AA** to **PP** needs effective barrier of 0.74 eV, which is larger than the desorption energy of 0.25 eV.

On the Pt(111) surface Loffreda *et al.*,^{16c} found that the effective barrier of **AA** formation is lower than that of **PA** formation (0.78 vs. 1.13 eV), indicating the kinetic preference of **AA** formation, while the desorption energy of **AA** is much higher than that of **PA** (1.08 vs. 0.23 eV). Hu *et al.*,¹⁴ reported acrolein partial hydrogenation to **AA**, **PA** and **EN** on the Pt(211) and Au(211) surfaces. On Pt(211), the most favored product is **EN**, which is favored both kinetically and thermodynamically, while on Au(211), the formation of **AA** is more favored due to its much lower energy barrier.

On the Ag(110) surface,^{13a} the effective barrier of **AA** and **PA** formation is 0.68 and 0.59 eV, respectively, indicating a slight preference of **PA** formation over **AA** formation. While on the subsurface oxygen decorated Ag(111) surface, the effective barrier of **AA** formation is lower than that of **PA** formation (1.07 and 1.33 eV, respectively), indicating the change of the selectivity upon subsurface oxygen decoration.

The stepwise reaction barriers of acrolein hydrogenation on different catalysts are shown in [Appendix Table A3](#).

5.4 Conclusions

The full hydrogenation of acrolein via allyl alcohol, propanal or enol to propanol on the Ni(111) surface has been computed using spin-polarized periodic density functional theory method; and all possible intermediates and products as well as their corresponding transition states have been considered.

On Ni(111), acrolein has adsorption energy, which is close to that of molecular hydrogen, and this indicates their possible co-adsorption and the reaction should obey the proposed Langmuir-Hinshelwood mechanism on the surface. Following the minimum energy path, acrolein hydrogenation on Ni(111) prefers the formation of propanal both kinetically and thermodynamically, while the formation of allyl alcohol has higher barrier and is more endothermic. The effective barrier is smaller in magnitude than the adsorption energy of acrolein.

In addition, allyl alcohol has stronger adsorption than propanal, and therefore propanal desorption is much easier than allyl alcohol desorption. Further calculations show that the hydrogenation of allyl alcohol to propanol has lower effective barrier than that of propanal. Since the adsorption energies of allyl alcohol and propanal are smaller in magnitudes than their effective hydrogenation barriers, their hydrogenation reaction should be more difficult. The main product of acrolein hydrogenation on Ni(111) should be propanal instead of the

desired allyl alcohol. Since the adsorption energies of propanal and allyl alcohol are much smaller than that of molecular hydrogen, the hydrogen of propanal or allyl alcohol might obey the Eley-Rideal mechanism with atomic hydrogen on the Ni(111) surface and propanal or allyl alcohol coming from the gas phase.

On the Ni(111) surface, the general trend that C=C double bonds can be more easily hydrogenated both kinetically and thermodynamically than C=O double bonds is also found in acrolein hydrogenation to propanal and allyl alcohol, as well as in the hydrogenation of propanal and allyl alcohol into propanol.

Further comparisons with acrolein partial hydrogenation on other Au, Ag and Pt surfaces show the different preference of the allyl alcohol and propionaldehyde.

5.5 References

- (1) (a) Gallezot, P.; Richard, D. *Catal. Rev.-Sci. Eng.* **1998**, *40*, 81–126. (b) Ponec, V. *Appl. Catal. A* **1997**, *149*, 27–48. (c) Claus, P. *Top. Catal.* **1998**, *5*, 51–62.
- (2) (a) Marinelli, T. B. L. W.; Nabuurs, S.; Ponec, V. *J. Catal.* **1995**, *151*, 431–438. (b) Mohr, C.; Hofmeister, H.; Radnik, J.; Claus, P. *J. Am. Chem. Soc.* **2003**, *125*, 1905–1911.
- (3) Hirschl, R.; Delbecq, F.; Sautet, P.; Hafner, J. *J. Catal.* **2003**, *217*, 354–366.
- (4) Kliewer, C. J.; Bieri, M.; Somorjai, G. A. *J. Am. Chem. Soc.* **2009**, *131*, 9958–9966.
- (5) Touroude, R. *J. Catal.* **1980**, *65*, 110–120.
- (6) Coq, B.; Figueras, F.; Geneste, P.; Moreau, C.; Moreau, P.; Warawdekar, M. *J. Mol. Catal.* **1993**, *78*, 211–226.
- (7) (a) Volckmar, C. E.; Bron, M.; Bentrup, U.; Martin, A.; Claus, P. *J. Catal.* **2009**, *261*, 1–8. (b) Bron, M.; Teschner, D.; Knop-Gericke, A.; Jentoft, F. C.; Kroehnert, J.; Hohmeyer, J.; Volckmar, C.; Steinhauer, B.; Schloegl, R.; Claus, P. *Chem. Phys. Chem. Phys.* **2007**, *9*, 3559–3569. (c) Lucas, M.; Claus, P. *Chem. Eng. Technol.* **2005**, *28*, 867–870. (d) Gruenert, W.; Brueckner, A.; Hofmeister, H.; Claus, P. *J. Phys. Chem. B* **2004**, *108*, 5709–5717.
- (8) Brandt, K.; Chiu, M. E.; Watson, D. J.; Tikhov, M. S.; Lambert, R. M.; *J. Am. Chem. Soc.* **2009**, *131*, 17286–17290.
- (9) (a) Claus, P. *Appl. Catal. A* **2005**, *291*, 222–229. (b) Claus, P.; Hofmeister, H.; Mohr, C. *Gold Bull* **2004**, *37*, 181–186.
- (10) (a) Murillo, L. E.; Menning, C. A.; Chen, J. G. *J. Catal.* **2009**, *268*, 335–342. (b) Murillo, L. E.; Chen, J. G. *Surf. Sci.* **2008**, *602*, 919–931. (c) Murillo, L. E.; Goda, A. M.; Chen, J. G. *J. Am. Chem. Soc.* **2007**, *129*, 7101–7105.
- (11) (a) Li, Z.; Ding, W. P.; Kang, G. J.; Chen, Z. X. *Catal. Commun.* **2012**, *17*, 164–167. (b) Kang, G. J.; Ma, J.; Chen, Z. X. *Catal. Lett.* **2012**, *142*, 287–293. (c) Kang, G. J.; Chen, Z. X.; Li, Z. *Catal. Lett.* **2011**, *141*, 996–1003. (d) Li, Z.; Chen, Z. X.; He, X.; Kang, G. J. *J. Chem. Phys.* **2010**, *132*, 184702–5. (e) He, X.; Chen, Z. X.; Kang, G. J. *J. Phys. Chem. C* **2009**, *113*, 12325–12330. (f) Li, Z.; Chen, Z. X.; Kang, G. J.; He, X. *J. Mol. Struct.: THEOCHEM* **2008**, *870*,

61–64.

(12) Wang, C. M.; Fan, K. N.; Liu, Z. P. *J. Catal.* **2009**, *266*, 343–350.

(13) (a) Lim, K. H.; Mohammad, A. B.; Yudanov, I. V.; Neyman, K. M.; Bron M.; Claus, P.; Rösch N. *J. Phys. Chem. C* **2009**, *113*, 13231–13240. (b) Lim, K. H.; Chen, Z. X.; Neyman, K. M.; Rösch, N. *Chem. Phys. Lett.* **2006**, *420*, 60–64.

(14) Yang, B.; Wang, D.; Gong, X. Q.; Hu, P. *Phys. Chem. Chem. Phys.* **2011**, *13*, 21146–21152, and references therein.

(15) Boronat, M.; May, M.; Illas, F. *Surf. Sci.* **2008**, *602*, 3284–3290.

(16) (a) Laref, S.; Delbecq, F.; Loffreda, D. *J. Catal.* **2009**, *265*, 35–42. (b) Lofferda, D.; Delbecq, F.; Vigné, F.; Sautet, P. *J. Am. Chem. Soc.* **2006**, *128*, 1316–1323. (c) Lofferda, D.; Delbecq, F.; Vigné, F.; Sautet, P. *Angew. Chem. Int. Ed.* **2005**, *44*, 5279–5282. (d) Lofferda, D.; Delbecq, F.; Sautet, P. *Chem. Phys. Lett.* **2005**, *405*, 434–439. (e) Delbecq, F.; Sautet, P. *J. Catal.* **2003**, *220*, 115–126. (f) Delbecq, F.; Sautet, P. *J. Catal.* **2002**, *211*, 398–406.

(17) Remediakis, I. N.; Abild-Pedersen, F.; Nørskov, J. K. *J. Phys. Chem. B* **2004**, *108*, 14535–14540.

(18) Oliva, C.; Berg, C. V. D.; Niemantsverdriet, J. W.; Curulla-Ferré, D. *J. Catal.* **2007**, *245*, 436–445.

(19) Mittendorfer, F.; Hafner, J. *J. Phys. Chem. B* **2002**, *106*, 13299–13305.

(20) (a) Peng, G.; Sibener, S. J.; Schatz, G. C.; Ceyer, S. T.; Mavrikakis, M. *J. Phys. Chem. C* **2012**, *116*, 3001–3006. (b) Peng, G.; Sibener, S. J.; Schatz, G. C.; Ceyer, S. T.; Mavrikakis, M. *Surf. Sci.* **2012**, *606*, 1050–1055.

(21) (a) Kresse, G.; Hafner, J. *Phys. Rev. B* **1993**, *47*, 558–561. (b) Kresse, G.; Hafner, J. *Phys. Rev. B* **1994**, *49*, 14251–14269. (c) Kresse, G.; Furthmüller, J. *Comput. Mater. Sci.* **1996**, *6*, 15–50. (d) Kresse, G.; Furthmüller, J. *Phys. Rev. B* **1996**, *54*, 11169–11186.

(22) Perdew, J. P.; Bruke, K.; Ernzerhof, M. *Phys. Rev. Lett.* **1996**, *77*, 3865–3868.

(23) Blöchl, P. E. *Phys. Rev. B* **1994**, *50*, 17953–17979.

(24) Methfessel, M.; Paxton, A. T. *Phys. Rev. B* **1989**, *40*, 3616–3621.

(25) Monkhorst, M.; Pack, J. D. *Phys. Rev. B* **1976**, *13*, 5188–5192.

(26) Luo, Q.; Fang, G.; Beller, M.; Jiao, H. *J. Phys. Chem. C* **2012**, *116*, 4149–4156.

(27) Jónsson, H.; Mills, G.; Jacobsen, K.W. In *Classical and Quantum Dynamics in Condensed Phase Simulations*; Berne, B. J.; Ciccotti, D. F. Eds, World Scientific: Singapore, **1998**; p385.

(28) Blom, C. E.; Grassi, G.; Bauder, A. *J. Am. Chem. Soc.* **1984**, *106*, 7427–7431.

(29) Chen, Z. -X.; Neyman, K. M.; Lim, K. W.; Rösch, N. *Langmuir* **2004**, *20*, 8068–8077.

(30) Yang, H.; Whitten, J. L. *J. Chem. Phys.* **1993**, *98*, 5039–5049.

(31) Kresse, G.; Hafner, J. *Surf. Sci.* **2000**, *459*, 287–302.

(32) Ferullo, R.; Branda, M. M.; Illas, F. *J. Phys. Chem. Lett.* **2010**, *1*, 2546–2549.

Appendix

Table A1 Adsorption energies (E_{ads} , eV) for all stationary points involved in HCO₂H dissociation into CO₂ and H on Ni(111) and Pd(111)

species	E_{ads}	species	E_{ads}
1a	-0.36	5a	-2.41
1b	-0.36	5b	-2.40
1c	0.04	1A	-0.39
1d	0.05	1B	-0.39
2a	-2.83	2A	-2.37
2b	-2.23	2B	-1.67
2c	-1.90	2C	-1.66
2d	-2.15	3A	-5.25
3a	-5.34	3B	-5.28
3b	-5.36		
4a	0.24		
4b	0.27		

Table A2 energetic and structural parameters of acrolein hydrogenation to propanol (energy in eV and bond distance in pm)

speices	Bond length (pm)								E_{ads}/E_a (eV)
	O1-C2	C2-C3	C3-C4	O1-Ni	C2-Ni	C3-Ni	C4-Ni	O/C-H	
AC	123	147	134						
PP	144	152	153						
O-CH₃	144				312				-2.56
CH₂-CH₃			154	198		211	272		-1.44
AC	135	145	145	205	200	217	200		-1.15
r₁	145	145	145	279	199	235	198		-1.56
r₂	144	153	145	197	255	216	200		-2.54
r₃	137	152	153	202	197	279	198		-1.78
r₄	135	142	151	202	205	213	303		-1.70
AA	146	150	145	215	294	198	213		-0.84
PA	138	151	152	200	199	302	352		-0.45
EN	141	141	151	229	208	209	311		-0.31
r₃₄₁	147	152	152	213	198	305	329		-1.38
r₃₄₂	145	152	153	198	310	354	496		-2.56
r₁₂₃	146	152	155	217	322	282	202		-1.55
r₁₂₄	146	151	153	210	293	200	298		-1.50
PP	145	152	153	218	324	373	472		-0.31
TS/R₁	136	145	144	212	202	226	199	139	1.00
TS/R₂	138	150	145	199	209	219	200	134	0.89
TS/R₃	137	151	148	203	196	208	211	143	0.96
TS/R₄	135	146	148	203	198	219	206	153	0.62
TS/R₂₁	141	151	145	199	272	205	201	150	0.92
TS/R₁₂	142	148	145	257	209	222	197	145	0.76
TS/R₄₃	135	145	152	201	206	220	326	144	0.66
TS/R₃₄	137	152	152	202	197	288	211	160	0.56
TS/R₄₁	136	142	151	209	210	211	306	139	1.07
TS/R₁₄	141	145	147	255	196	219	206	149	0.58
TS/R₁₂₃	145	152	149	223	300	207	212	146	0.70
TS/R₁₂₄	146	151	149	213	300	202	211	152	1.03
TS/R₃₄₁	138	152	152	201	204	305	335	141	1.10
TS/R₃₄₂	138	152	152	199	214	324	407	161	0.59
TS/R₁₄₂	142	146	152	236	217	204	309	135	0.76
TS/R₁₄₃	142	146	152	224	205	212	321	147	0.55
TS/R₃₄₂₁	143	152	153	194	296	371	471	158	1.35
TS/R₃₄₁₂	144	152	152	218	220	302	355	157	0.90
TS/R₁₂₄₃	145	152	153	210	290	222	322	154	0.72
TS/R₁₂₃₄	146	153	159	221	318	317	214	159	0.77

Table A3 stepwise reaction barriers of acrolein hydrogenation on different catalysts (energy in eV)

	Ni(111)	Au(110)	In/Au(110)	Au ₂₀	AuOH/ZrO ₂	Au(211)	Pt(211)	Pt(111)	Pt(111)	Ag(110)	O _{sub} /Ag(111)
R₁	1.00	0.45	0.84	0.83	0.31	0.74	0.51	0.42	0.19	0.81	0.94
R₂	0.89	0.70	0.41	0.87	2.07	1.38	0.81	0.62	0.51	0.68	2.06
R₃	0.96	0.54	0.52	0.86	0.82	1.32	0.73	0.95	0.85	0.77	2.08
R₄	0.62	0.97	0.92	0.77	0.97	0.94	0.67	0.93	0.83	0.37	1.33
R₂₁	0.92	0.46	0.61	0.30	0.2	1.08	0.60	0.32	0.20	0.41	1.55
R₁₂	0.76	0.37	0.34	0.33	0.22	1.20	0.75	0.78	0.69	0.34	1.07
R₄₃	0.66	0.70	0.97	0.51	0.52	0.95	0.82	1.00	0.84	0.59	0.94
R₃₄	0.56	0.92	1.00	0.39	0.69	0.85	0.70	1.05	0.85	0.82	1.88
R₄₁	1.07								0.02		
R₁₄	0.58					1.00	0.83		0.83		
R₃₄₁	1.10										
R₃₄₂	0.59										
R₁₂₃	0.70				0.82						
R₁₂₄	1.03				0.74						
R₁₄₂	0.76										
R₁₄₃	0.55										
R₃₄₂₁	1.35										
R₃₄₁₂	0.90										
R₁₂₄₃	0.72				0.14						
R₁₂₃₄	0.77				0.34						
Ref		1	1	2	3	4	4	5	6	7	7

(1) He, X.; Chen, Z. X.; Kang, G. J. *J. Phys. Chem. C* **2009**, *113*, 12325–12330.

(2) Li, Z.; Chen, Z. X.; He, X.; Kang, G. J. *J. Chem. Phys.* **2010**, *132*, 184702–5.

(3) Wang, C. M.; Fan, K. N.; Liu, Z. P. *J. Catal.* **2009**, *266*, 343–350.

(4) Yang, B.; Wang, D.; Gong, X. Q.; Hu, P. *Phys. Chem. Chem. Phys.* **2011**, *13*, 21146–21152.

(5) Lofferda, D.; Delbecq, F.; Vigné, F.; Sautet, P. *Angew. Chem. Int. Ed.* **2005**, *44*, 5279–5282.

(6) Lofferda, D.; Delbecq, F.; Vigné, F.; Sautet, P. *J. Am. Chem. Soc.* **2006**, *128*, 1316–1323.

(7) Lim, K. H.; Mohammad, A. B.; Yudanov, I. V.; Neyman, K. M.; Bron, M.; Claus, P.; Rösch, N. *J. Phys. Chem. C* **2009**, *113*, 13231–13240.

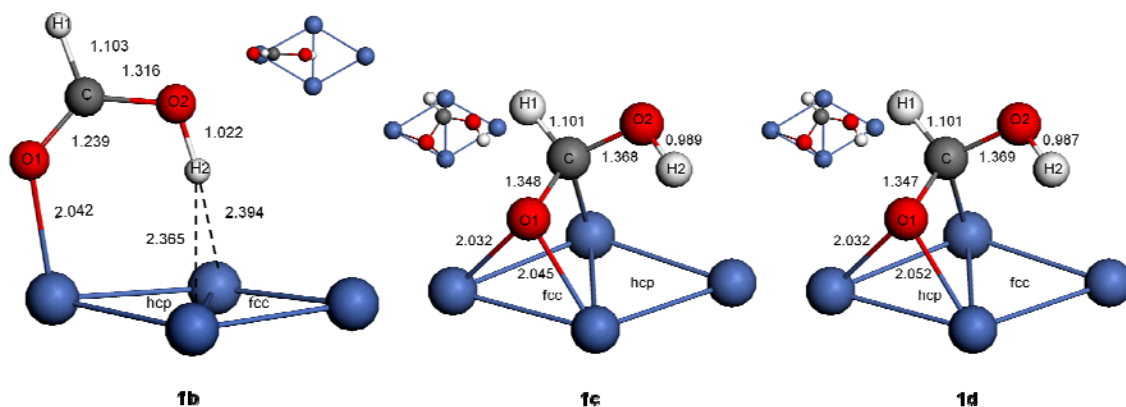


Figure A1 The stable HCO₂H adsorption configuration on Ni(111) (bond distances in Å)

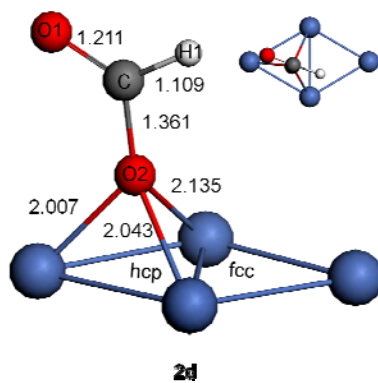


Figure A2 Equilibrium state of HCO₂ adsorption on Ni(111) (bond distances in Å)

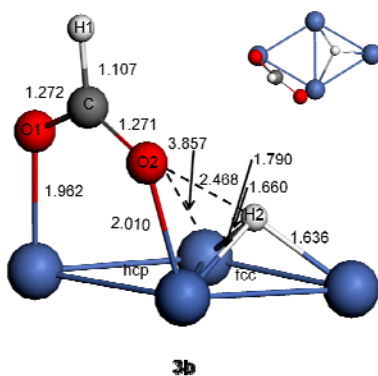


Figure A3 HCO₂ and H co-adsorption on Ni(111) (bond distances in Å)

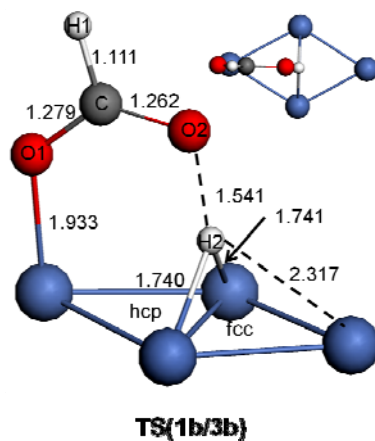


Figure A4 Transition state of $\text{HCO}_2\text{H} \rightarrow \text{HCO}_2 + \text{H}$ on Ni(111) (bond distances in Å)

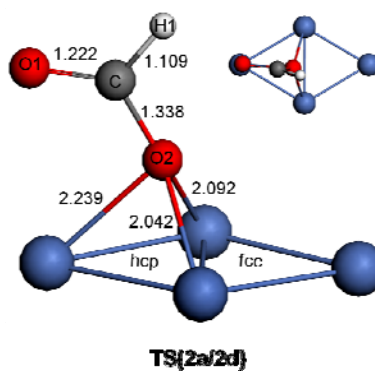


Figure A5 Transition state of the coordination change of HCO_2 adsorption on Ni(111) (bond distances in Å)

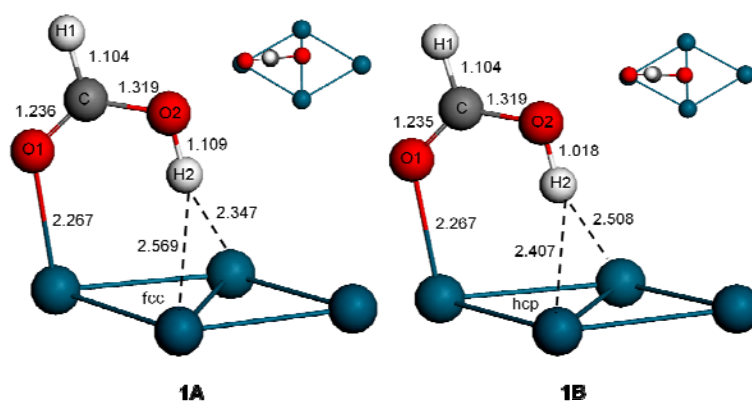


Figure A6 The stable HCO_2H adsorption configurations on Pd(111) (bond distances in Å)

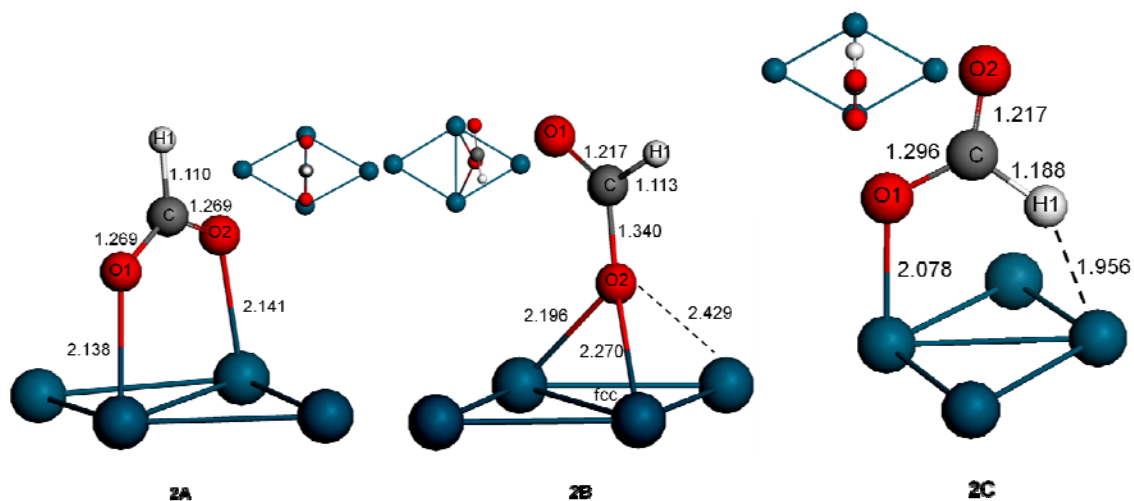


Figure A7 The stable HCO₂ adsorption configurations on Pd(111) (bond distances in Å)

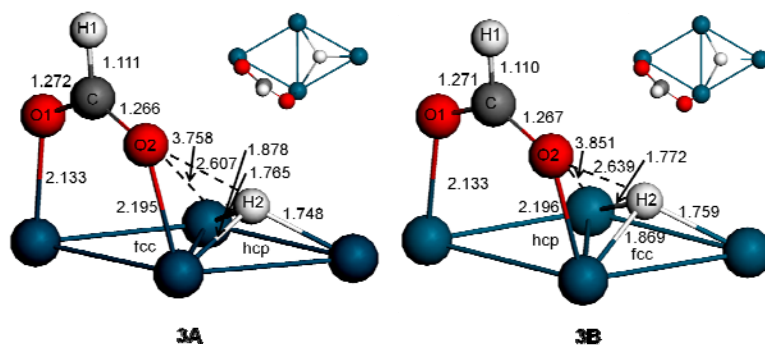


Figure A8 HCO₂ and H co-adsorption on Pd(111) (bond distances in Å)

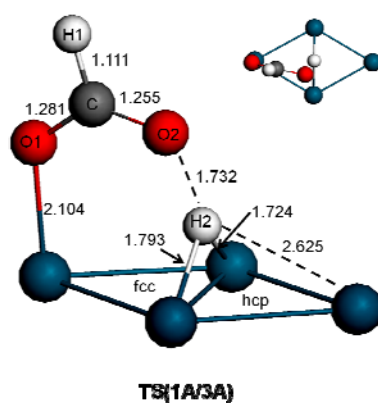


Figure A9 Transition state of HCO₂H → HCO₂ + H on Pd(111) (bond distances in Å)

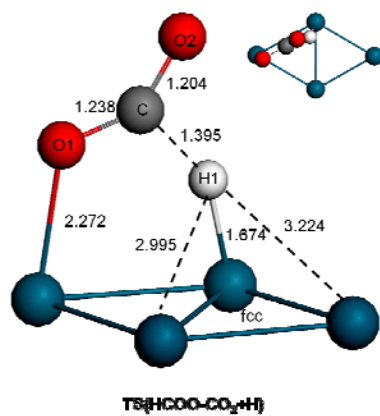


Figure A10 Transition state of $\text{HCO}_2 \rightarrow \text{CO}_2 + \text{H}$ on Pd(111) (bond distances in Å)

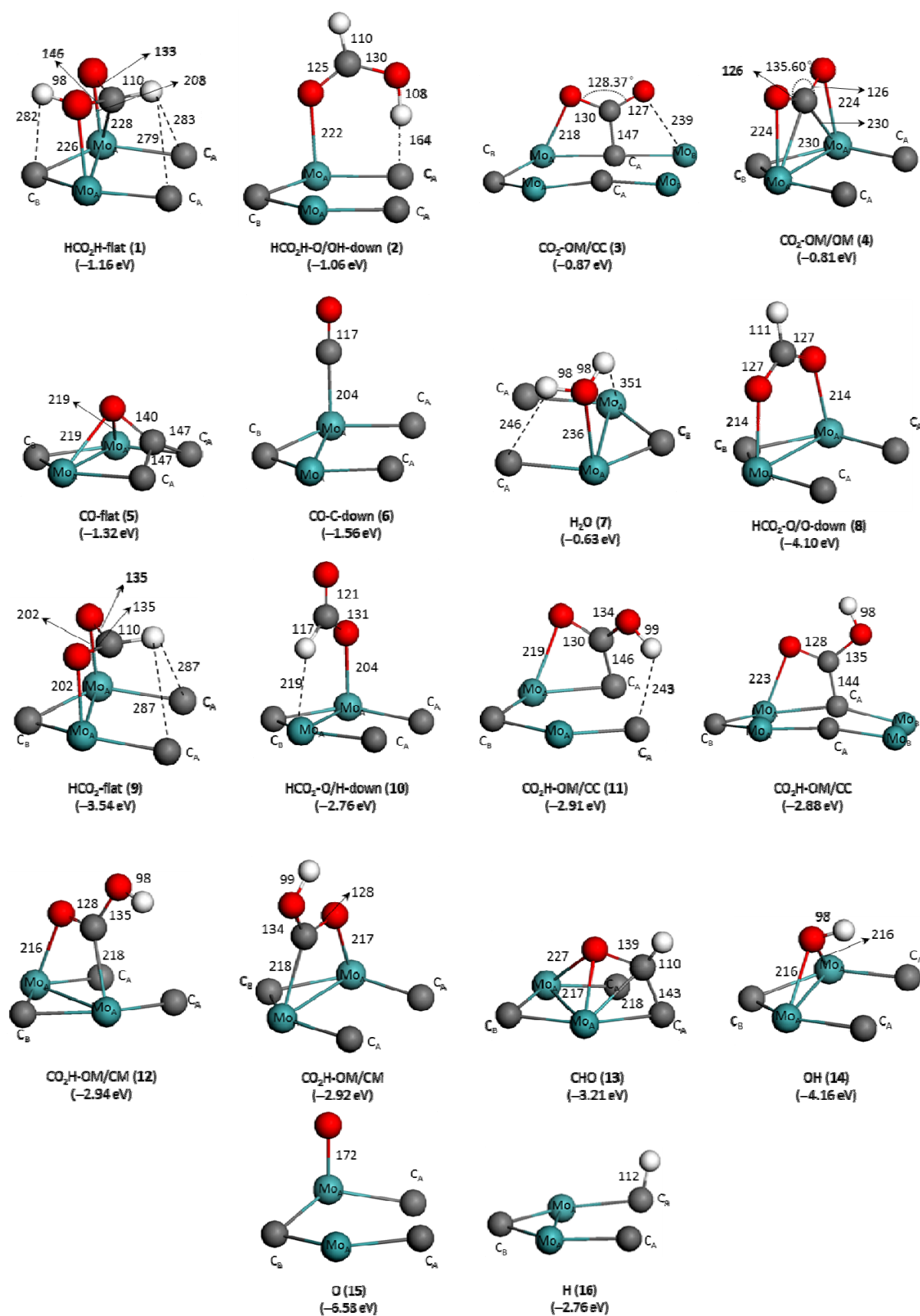


Figure A11 The most stable adsorption configurations of intermediates involved in FA decomposition at 1/4 ML (bond distances in pm and energies in eV)

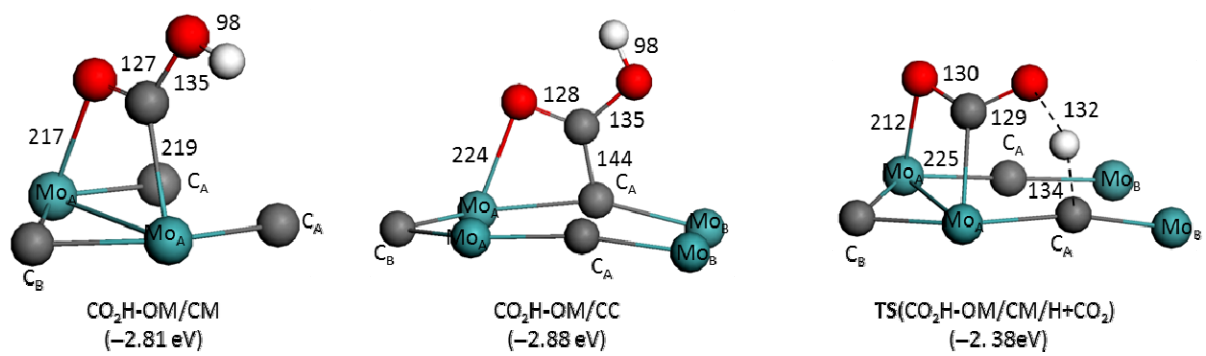


Figure A12 Adsorption configurations and transition state at 1/16 ML (bond distances in pm and energies in eV)

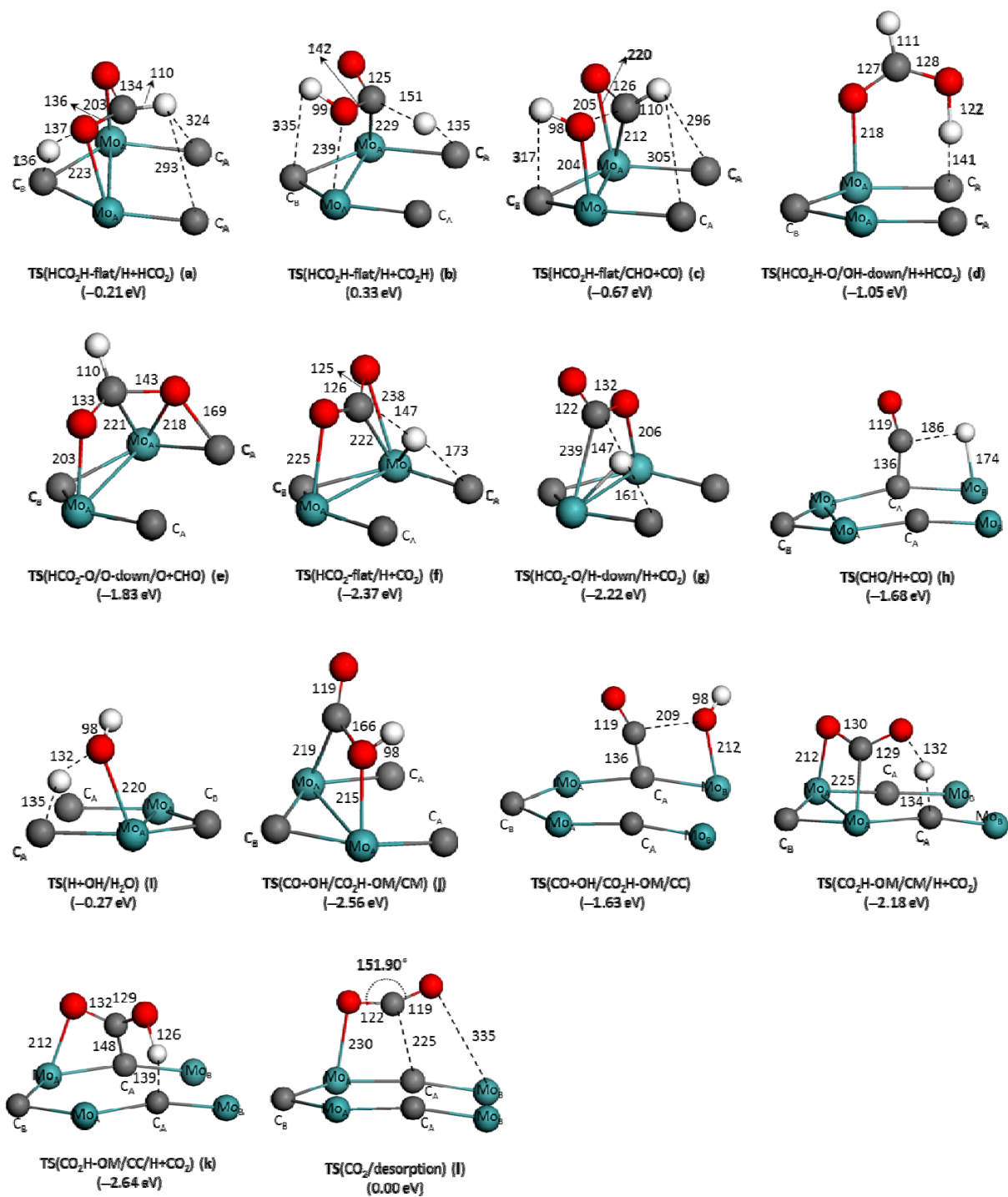


Figure A13 The transition configurations involved in FA decomposition at 1/4 ML (bond distances in pm and energies in eV)

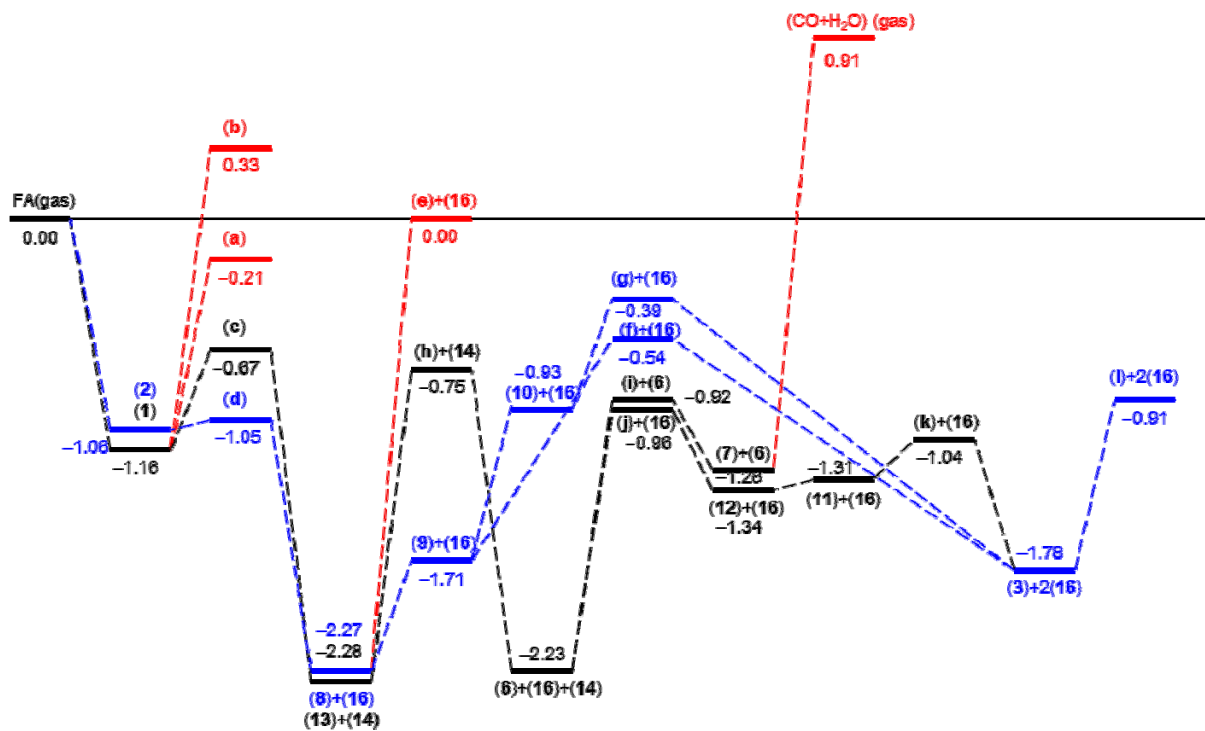


Figure A14 Potential energy surface at 1/4 ML (energies in eV)

Text A1

The formation of surface formate and H via perpendicular configuration (HCO₂H-O/OH-Down (2)) and the formation of surface CHO and OH via the flat one compete on the surface at low coverage; therefore, a micro-kinetic modeling is virtually needed to quantify the selectivity of the various products.

Micro-kinetic modeling has got increasing concerns in the study of heterogeneous catalysis for understanding the mechanistic details (Lynggaard, H.; Andreasen, A.; Stegelmann, C.; Stoltze, P. *Prog. Surf. Sci.* **2004**, 77, 71-137). Based on the proposed scheme, we have tried to investigate the quantity of the selective formic acid dehydrogenation and dehydration on molybdenum carbide. Unfortunately, we could not get the partial pressure of CO and H₂O; or CO₂ and H₂ from the available experimental data. Without those parameters, the final TOF of the formation of H₂ or CO could not be obtained. Indeed, experimental work also shows CO-free H₂ formation from formic acid on molybdenum carbide. Nevertheless we have tried to extract the question by considering the minimum energy path of formation CO₂ and H₂ versus the minimum energy path of formation CO and H₂O.

The reaction path contains many elementary steps, which determine the overall reaction rate. Our potential energy surface reveals that the first three elementary steps play very important roles in the selectivity of FA dissociation since the rate determining step was the third step (HCO₂→ CO₂ + H vs. CHO→ CO + H). We supposed that these three elementary steps consist of a consecutive reaction, and therefore we mainly considered the reaction rates of these steps.

The first step is the adsorption of the FA. Two adsorption models with similar adsorption energy were found and their difference in adsorption energy determines their coverage differences. For the adsorption of FA, the adsorption equilibrium constant (K_{ads}), which determines the stable coverage of FA on the surface, can be got from equation $\Delta G_{\text{ads}} = -RT \ln K_{\text{ads}}$. Where, $\Delta G_{\text{ads}} = G_{\text{slab+FA}} - G_{\text{slab}} - G_{\text{FA}}$, is a function of temperature and pressure. Here, we chose 373K as the sample temperature for discussion.

373K	$\Delta G_{\text{ads}}/\text{eV}$	$K_{\text{ads}}/\text{s}^{-1}$
HCO ₂ H-flat (1)	-1.19	1.06×10^{16}
HCO ₂ H-O/OH-Down (2)	-1.13	1.64×10^{15}

The second elementary step of those two different reaction paths starts from FA with flat and perpendicular adsorption modes. The reaction rate of this step can be described by the equation $r_2 = K_2\theta$, where K_2 is the reaction rate constant of the second step and θ is the coverage of adsorbed FA (which is determined by K_{ads}). The value of K_2 is derived from Arrhenius equation $K = k_B T/h \times \exp(-E_a/RT)$, approximately; where, k_B is Boltzmann's constant,

and h is Planck's constant, E_a is the computed activation energy. Here, we supposed that pre-exponential factors are approximately equal. For the two different reaction paths, the reaction rate constants can be estimated.

373K	E_a /eV	K_2/s^{-1}
HCO ₂ H-flat/CHO+CO (c)	0.48	2.53×10^6
HCO ₂ H-O/OH-down/H+HCO ₂ (d)	0.02	4.17×10^{12}

For the rate-determined step, similar estimation was done as the case of step two, and the reaction rate constant (K_3) at 373K was given in the following table.

373K	E_a /eV	K_3/s^{-1}
HCO ₂ -O/O→ down/H+CO ₂	1.46	1.43×10^{-7}
CHO/H+CO (h)	1.61	1.35×10^{-9}

Since those three primary steps composed an overall consecutive reaction, the overall reaction rate (K_{total}) can be determined approximately by multiplying K_{ads} , K_2 and K_3 .

373K	K_{total}/s^{-1}
HCO ₂ H-flat → CO ₂ + 2H	9.19×10^{18}
HCO ₂ H-O/OH-Down → CO + H + OH	3.84×10^{15}

Thus, the formation of CO₂ and 2H via HCO₂H-O/OH-Down (2) is around 2300 time more faster than the formation of CO, H and OH via HCO₂H-flat (1) on the surface, even to say, surface CO + H + OH can either form CO + H₂O or H₂ and CO₂ and 2H under close activation energy. Based on the above analyses, formic acid selective decomposition into CO-free H₂ agrees with the experimental result. And our DFT results are reasonable.

Eidesstattliche Erklärung

I hereby declare under oath that I have completed the work submitted here independently and have composed it without outside assistance. Furthermore, I have not used anything other than the resources and sources stated and where I have taken sections from these works in terms of content or text, I have identified this appropriately.

Rostock, den 29. Juli 2013

Qiquan Luo

Curriculum Vitae

Personal Data

Name: Qiquan Luo
Date of birth: 14th March 1984 in Anhui Province, China
Address: Max-Planck Str. 3a. Zi.1.03.2 D-18059 Rostock, Germany
Phone: +49 (0)381-1281-351
Mail: qiquan.luo@catalysis.de; luoqiquan@sina.com.cn

Education

10/2009 – today Leibniz-Institut für Katalyse e.V., Rostock University, Germany
PhD student in the research group of PD. Dr. Habil. Haijun Jiao
Title: “*Theoretical Study of Formic Acid Dehydrogenation and Full Hydrogenation of Acrolein*”

Supervisor: PD Dr. Habil. Haijun Jiao

9/2006 – 7/2009 School of Physics and Material Science, Anhui University, China
Master thesis: “*Structure and Properties of Nickel and Doped Aluminum Clusters*”
Supervisor: Prof. Dr. Qi-Liang Lu

9/2002 – 7/2006 Department of Physics and Maths, West Anhui University, China
Supervisor: Prof. Dr. Xing-Ju Wu

Scholarship

10/2009 – 9/2013 State Scholarship Fund (China Scholarship Council)

Publications

Luo, Q.; Feng, G.; Beller, M.; Jiao, H. "Formic Acid Dehydrogenation on Ni(111) and comparison with Pd(111) and Pt(111)" *The Journal of Physical Chemistry C* **2012**, *116*, 4149–4156.

Luo, Q.; Wang, T.; Beller, M.; Jiao, H. "Hydrogen Generation From Formic Acid Decomposition on Ni(211), Pd(211) and Pt(211)" *submitted to The Journal of Molecular Catalysis A: Chemical*

Luo, Q.; Wang, T.; Beller, M.; Jiao, H. "Molybdenum Carbide Catalysed Hydrogen Production from Formic Acid" *The Journal of Power Sources* **2013**, in press

Luo, Q.; Beller, M.; Jiao, H. "FORMIC ACID DEHYDROGENATION ON SURFACES – A REVIEW OF COMPUTATIONAL ASPECTS" *The Journal of theoretical and computational chemistry* **2013**, DOI: 10.1142/S0219633613300012.

Luo, Q.; Wang, T.; Beller, M.; Jiao, H. "Full Acrolein Hydrogenation on Ni(111)" *The Journal of Physical Chemistry C* **2013**, *117*, 12715–12724..